AD-784 959

A DETERMINISTIC APPROACH TO THE PREDICTION OF TELESEISMIC GROUND MOTION FROM NUCLEAR EXPLOSIONS

J. T. Cherry, et al

Systems, Science and Software

Prepared for:

Defense Nuclear Agency
Advanced Research Projects Agency

18 January 1974

REPORT DOCUMENTATION PAGE		READ INSTRUCTIONS BEFORE COMPLETING FORM
1. REPORT NUMBER DNA 3321F	2. GOVT ACCESSION NO.	3. RECIPIENT'S CATALOG NUMBER AD 784 959
4. TITLE (and Subtitle) A DETERMINISTIC APPROACH TO THE PREDICTION OF TELESEISMIC GROUND MOTION FROM NUCLEAR EXPLOSIONS		5. TYPE OF REPORT & PERIOD COVERED Final Report
		6. PERFORMING ORG. REPORT NUMBER SSS-R-74-2034
7. AUTHOR(s) J. T. Cherry, T. C. Bache, C. B. Archambeau, and D. G. Harkrider		8. CONTRACT OR GRANT NUMBER(s) Contract No. DNA 001-73-C-0167
9. PERFORMING ORGANIZATION NAME AND ADDRESS Systems, Science and Software P.O. Box 1620 La Jolla, California 92037		10. PROGRAM ELEMENT, PROJECT, TASK AREA & WORK UNIT NUMBERS ARPA Order No. 1866, Amend #3, RMSS Code 199-QARSB047, Work Unit 01
11. CONTROLLING OFFICE NAME AND ADDRESS Director, Defense Advanced Research Projects Agency, 1400 Wilson Boulevard, Arlington, Virginia 22209		12. REPORT DATE Jan. 18, 1974
		13. NUMBER OF PAGES 165
14. MONITORING AGENCY NAME & ADDRESS(if different from Controlling Office)		15. SECURITY CLASS. (of this report) Unclassified
		15a. DECLASSIFICATION DOWNGRADING SCHEDULE

16. DISTRIBUTION STATEMENT (of this Report)

Approved for public release; distribution unlimited.

17. DISTRIBUTION STATEMENT (of the abstract entered in Block 20, if different from Report)

18. SUPPLEMENTARY NOTES

This work was supported by the Defense Nuclear Agency, Washington, D. C.

19. KEY WORDS (Continue on reverse side if necessary and identify by block number)

Seismology, Nuclear Explosions. Teleseismic Ground Motion, Detection

20. ABSTRACT (Continue on reverse side if necessary and identify by block number)

   Theoretical predictions of teleseismic ground motion from explosions are presented using a deterministic computer model which merges nonlinear shock code calculations in the near-field with seismic code calculations of far-field stress wave propagation through a realistic earth structure. The predicted ground motion given by synthetic seismograms is shown to be in good agreement with observations of body and surface wave motion.

DD FORM 1473 1 JAN 73   EDITION OF 1 NOV 65 IS OBSOLETE

I

For a given earth structure, surface wave magnitude (M_s) is found to be directly proportional to $\log_{10} \psi(\infty)$, the logarithm of the steady state value of the reduced displacement potential. On the other hand, body wave magnitude is found to be strongly influenced by depth of burial and the near source compressional velocity, as well as $\psi(\infty)$. The shape of the source spectrum has no effect on M_s and only a minor effect on m_b. Thus, if depth of burial and earth structure are invariant, m_b is directly proportional to $\log_{10} \psi(\infty)$.

Tectonic stress relaxation is found to add considerable complexity to the first arrival P wave train but to have little effect on m_b. Having developed improved models of other factors influencing teleseismic ground motion from explosions, the importance of accurate earth structure models for both body and surface wave propagation is highlighted.

II

FOREWORD

This final technical report entitled, "A Deterministic Approach to the Prediction of Teleseismic Ground Motion From Nuclear Explosions," is submitted by Systems, Science and Software (S³) to the Advanced Research Projects Agency (ARPA) and to the Defense Nuclear Agency (DNA). The report presents the results from a twelve-month effort to determine the sensitivity of M_s and m_b to variations in explosion yield, depth of burial, near source material properties and earth structure. The work was performed under Contract Number DNA 001-73-C-0167. Col. J. T. Jones was the ARPA Program Manager and Mr. Clifton B. McFarland was the DNA Project Scientist.

Dr. J. Theodore Cherry was the S³ Project Manager for the study. Professors Charles B. Archambeau and David G. Harkrider of the California Institute of Technology were consultants on the project. Their interaction with Dr. Thomas C. Bache, Dr. Gerald A. Frazier and Mr. Kenneth G. Hamilton have made the teleseismic codes viable prediction tools.

TABLE OF CONTENTS

Preceding page blank

TABLE OF CONTENTS (Cont.)   Page

I. INTRODUCTION

This report presents theoretical predictions of tele-seismic ground motion from underground nuclear explosions. The theoretical predictions, which are presented in the form of synthetic seismograms, are obtained from a deterministic computer model which merges nonlinear shock code calculations in the near-field with seismic code calculations of far-field stress wave propagation through a realistic earth model. The application of this computer model to study dependence of teleseismic ground motion on explosion yield, depth of burial, near-source material properties, tectonic stress release and the earth structure between source and receiver is the sub-ject of this report.

Assuming spherical symmetry, the explosion representa-tion in terms of an equivalent elastic source (the reduced displacement potential, RDP) is calculated using a one-dimensional, Lagrangian finite-difference code (SKIPPER). This shock wave code requires, as input, a description of the near source material response to arbitrary stress load-ing. The shock wave from the high pressure cavity which con-tains the rock vaporized by the explosion is then propagated to a radius at which the response is linear elastic. The RDP is then obtained from the calculated displacement or velo-city history of a particle in the elastic region.

The teleseismic body and surface wave codes accept the SKIPPER calculated RDP and propagate it through a given heterogeneous earth model. The body wave code uses ray theory in a radially stratified earth model while the sur-face wave code assumes a flat earth model and sums the vertically trapped modes of propagation. The shock wave code and its interaction with the body and surface wave codes has been described by Cherry, et al.[1] The details

5

of the surface wave calculations are given by Harkrider.[2]
The ray theory used in the body wave calculation may be
found in Bullen.[3]

In Section II of this report the calculation of the
equivalent elastic source (RDP) for explosions in tuff,
granite and sandstone are described. A study of the sur-
face waves emanating from explosions in these three media
is presented in Section III. In Section IV the correspond-
ing body wave calculations are presented.

A major goal of this investigation has been to deter-
mine the dependence of body and surface wave magnitudes, m_b
and M_s, on the important parameters characterizing the ex-
plosions which are listed in the first paragraph. Since
theoretical seismograms at teleseismic distances are now
routinely obtained, m_b and M_s are picked directly from the
seismograms in a standard manner and compared to observations.
In this way the model parameters controlling m_b and M_s are
identified.

For a given earth structure, M_s is found to be directly
proportional to $\log_{10} \psi(\infty)$, the logarithm of the steady state
value of the RDP. On the other hand, body wave magnitude is
found to be strongly influenced by depth of burial and near
source compressional velocity, as well as $\psi(\infty)$. The shape of
the source spectrum has no influence on M_s and only a minor
effect on m_b. Also, while tectonic stress release may add
considerable complexity to the P wave train, it has little
effect on m_b. For both body and surface waves, the importance
of an accurate earth structure model is emphasized.

The deterministic approach used in this research, fea-
turing a synthesis of results from rock mechanics, linear and
nonlinear continuum mechanics, computational physics and seis-
mology, now permits a detailed analysis of the factors controlling
the teleseismic signature of a nuclear explosion.

6

II. CALCULATED SOURCE FUNCTIONS

2.1 THE REDUCED DISPLACEMENT POTENTIAL

SKIPPER[1, 4] is a Lagrangian, finite-difference code that numerically simulates a propagating stress (shock) wave in one space dimension. The code is capable of carrying the stress field into the small displacement elastic regime and yet flexible enough to permit appropriate material response formulations in the large displacement nonlinear regime.

For a spherically symmetric explosion source the reduced displacement potential, ψ, is given by

$$U(t,r) = - \frac{\partial}{\partial r} \frac{\psi(\tau)}{r} = \frac{\psi}{r^2} + \frac{\dot{\psi}}{r\alpha} , \qquad (2.1)$$

where

$U(t,r)$ = radial particle displacement at t and r in the elastic region

α = the compressional velocity in the earth medium

t = time

r = radial position

$\tau = t - r/\alpha$ = retarded time

$\dot{\psi} = d\psi/d\tau$ = the reduced velocity potential (RVP)

Since ψ is only a function of τ in the elastic region, its wave form does not change with changing r. Therefore, Eq. (2.1) may be used to determine ψ at any radius in the elastic zone. A subroutine exists within the SKIPPER code that numerically integrates Eq. (2.1) at various specified radii from the center of the explosion. The fact

7

that ψ should be invariant with the radius provides an important verification that the specified radii are in the elastic region.

The following equations show the relation between the RDP (and its derivatives) and particle velocity (u), radial stress (T_{rr}), tangential stress ($T_{\theta\theta}$) and the hydrodynamic component of stress (P):

$$u = - \frac{\partial}{\partial r}\left(\frac{\dot{\psi}}{r}\right) = \frac{\dot{\psi}}{r^2} + \frac{\ddot{\psi}}{r\alpha} , \qquad (2.2)$$

$$T_{rr} = -\rho\left[\frac{\alpha^2 P}{k} + 4\beta^2\left(\frac{\psi}{r^3} + \frac{\dot{\psi}}{r^2\alpha}\right)\right] , \qquad (2.3)$$

$$T_{\theta\theta} = -\left(\frac{k - 2/3\mu}{k}\right) P + 2\mu\left(\frac{\psi}{r^3} + \frac{\dot{\psi}}{r^2\alpha}\right), \qquad (2.4)$$

$$P = -\left(\frac{T_{rr} + 2T_{\theta\theta}}{3}\right) = k \frac{\ddot{\psi}}{r\alpha^2} , \qquad (2.5)$$

where

    k = the bulk modulus,

    μ = the shear modulus,

    ρ = density,

    $\alpha = \sqrt{\dfrac{k + 4/3\mu}{\rho}}$,

    $\beta = \sqrt{\dfrac{\mu}{\rho}}$ = shear wave velocity.

These equations show that only the hydrodynamic component of stress will attenuate as r^{-1} over the entire elastic region. Also, from Eq. (2.1) the steady-state value of

the RDP is given by

$$\psi(\infty) = r^2 U(\infty, r) \tag{2.6}$$

where $U(\infty, r)$ is the steady-state (static) displacement at the radius, r.

Both the body wave and surface wave teleseismic codes accept the equivalent source function in the frequency domain. Since the RDP, ψ, has a finite steady-state value, its Fourier transform is difficult to evaluate numerically. The RVP, $\dot{\psi}$, has a steady-state value of $\dot{\psi}(\infty) = 0$, so that its Fourier transform is bounded at zero frequency. If $\hat{\dot{\psi}}$ is the Fourier transform of the RVP, then at zero frequency

$$\hat{\dot{\psi}}(\nu = 0) = \int_{-\infty}^{\infty} \dot{\psi}(\tau) d\tau = \int_{0}^{\infty} \frac{d\psi}{d\tau} d\tau .$$

Therefore, since $\psi(0) = 0$,

$$\hat{\dot{\psi}}(0) = \psi(\infty) \tag{2.7}$$

All our calculated source functions will be presented in the $\hat{\dot{\psi}}$ format. Equation (2.7) relates an important time domain parameter, $\psi(\infty)$, to the value of the RVP transform at zero frequency.

We will find it convenient to scale the source function, calculated from SKIPPER, to different explosion yields. Table 2.1 gives the appropriate cube root scaling for each of the listed variables. This scaling follows from the assumption that cavity volume (L^3) is directly proportional to yield (W). Therefore $L \sim W^{1/3}$. Since the wave velocity in the medium is independent of yield, then $T \sim W^{1/3}$.

We have found[4] that the scaling given in Table 2.1 is in fact applicable to SKIPPER calculations having the same properties but differing greatly in the explosion yield.

9

TABLE 2.1

SCALING RULES FOR THE LISTED VARIABLES

r	cm	L	$W^{1/3}$
ν	sec^{-1}	T^{-1}	$W^{-1/3}$
τ	sec	T	$W^{1/3}$
ψ	cm^3	L^3	W
$\hat{\psi}$	cm^3 sec	$L^3 T$	$W^{4/3}$
$\dot{\psi}$	cm^3/sec	$L^3 T^{-1}$	$W^{2/3}$
$\hat{\dot{\psi}}$	cm^3	L^3	W

10

2.2   TUFF

The technique used in SKIPPER to obtain the pressure component (P) of the equation of state has been presented in detail in previous reports[1,4] and only a brief summary will be given here.

The code initially assumes a pressure equilibrium mixing of grain density tuff and water, where the mix is obtained by specifying f, the mass fraction of water. Figures 2.1a and 2.1b show the Hugoniot and a few release isentropes for these two constituents. Figure 2.2 shows the result of mixing the constituents of Fig. 2.1 using f = 0.17.

Partial saturation is developed by specifying both the initial void fraction, ϕ_0, and the rate of irreversible void collapse during pressure loading. Figure 2.3 shows the loading and release P-v curves that result from adding five percent air-filled porosity (ϕ_0 = 0.05) to the mix of Fig. 2.2. Also shown in the figure are the experimentally determined unloading data for Unit 3 tuff at the NTS Diamond Dust site.[5] The pressure state labeled P_c in the figure represents the state at which total irreversible pore collapse occurs, while P_e gives the (elastic) pressure at which irreversible pore collapse begins.

We have assumed that material strength depends on the pressure (P) and internal energy (e) and is governed by a relation of the form

$$S_{ij}S_{ji} \leq \frac{2}{3} Y^2(P,e), \qquad (2.8)$$

where $S_{ij} = T_{ij} - \delta_{ij}P$ is the stress deviator tensor and

$$Y(P,e) = \frac{Y_m}{P_m} P \left| 2 - \frac{P}{P_m} \right| \left| 1 - \frac{e}{e_m} \right| , \qquad P < P_m ,$$

$$= Y_m \left| 1 - \frac{e}{e_m} \right| , \qquad\qquad P > P_m , \qquad (2.9)$$

$$= 0 \qquad\qquad , \qquad\qquad e > e_m .$$

11
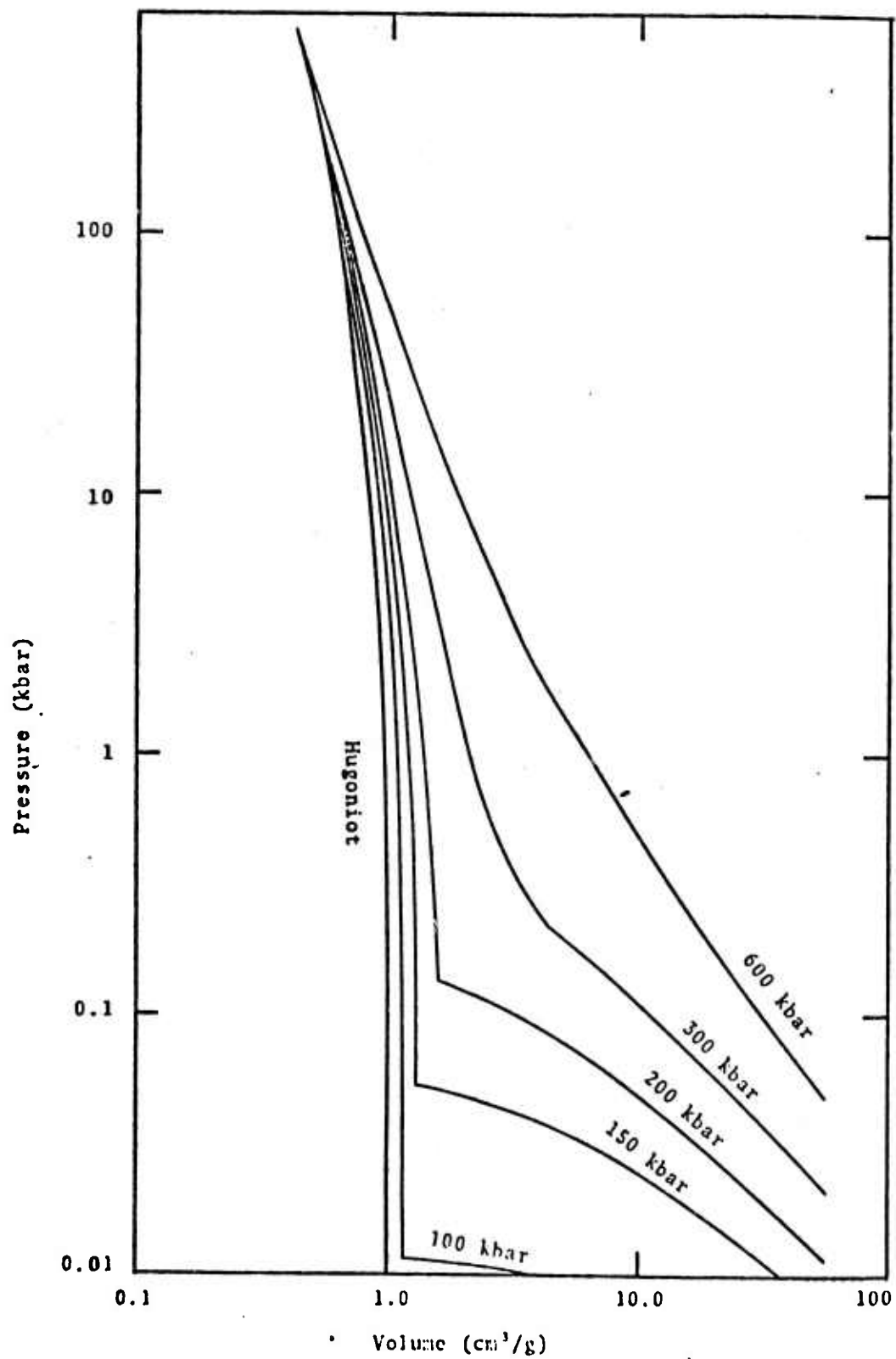
Fig. 2.1a--Hugoniot and release isentropes for water.
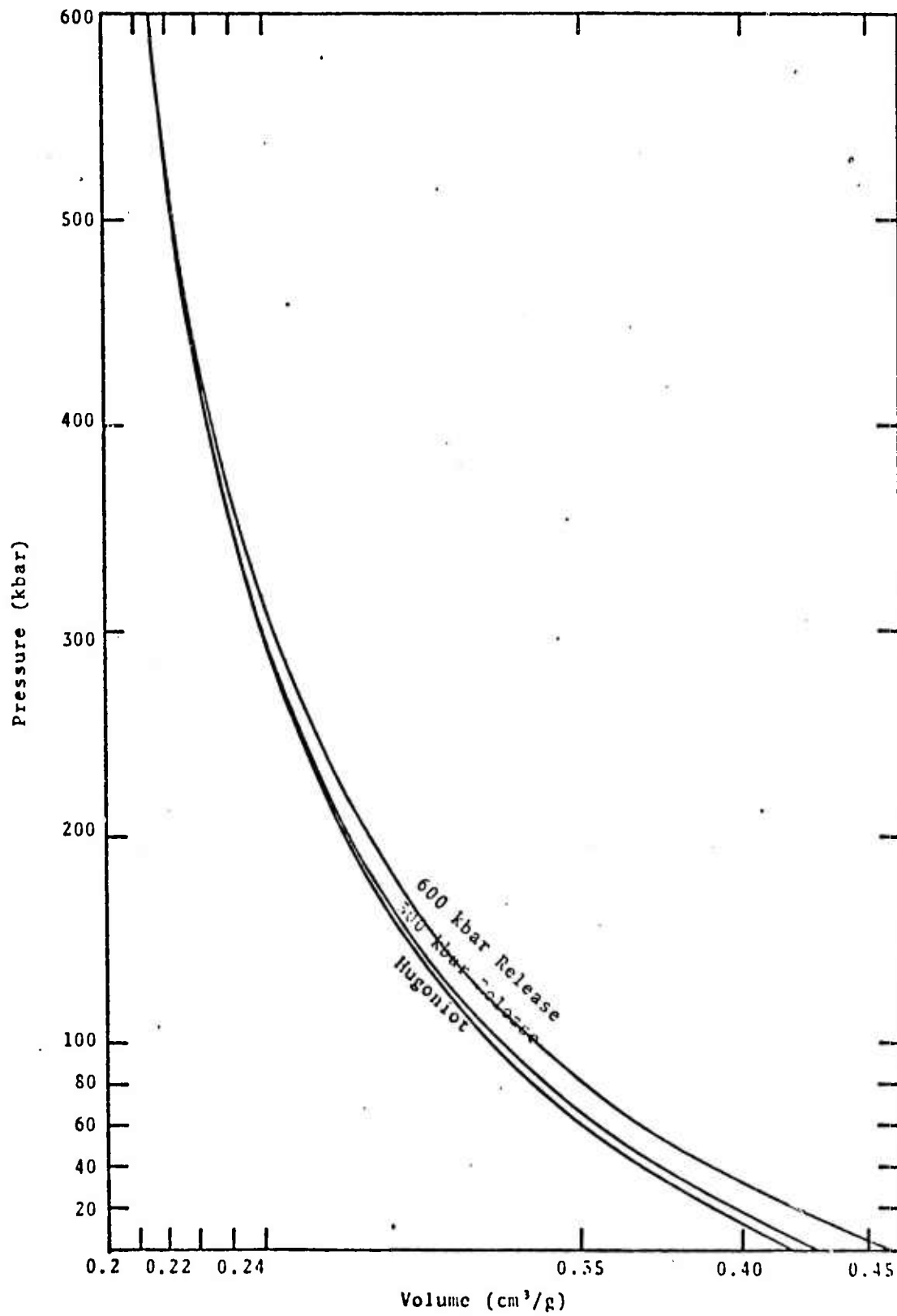
Fig. 2.1b--Hugoniot and release isentropes for tuff, ρ_0 = 2.4 g/cc.
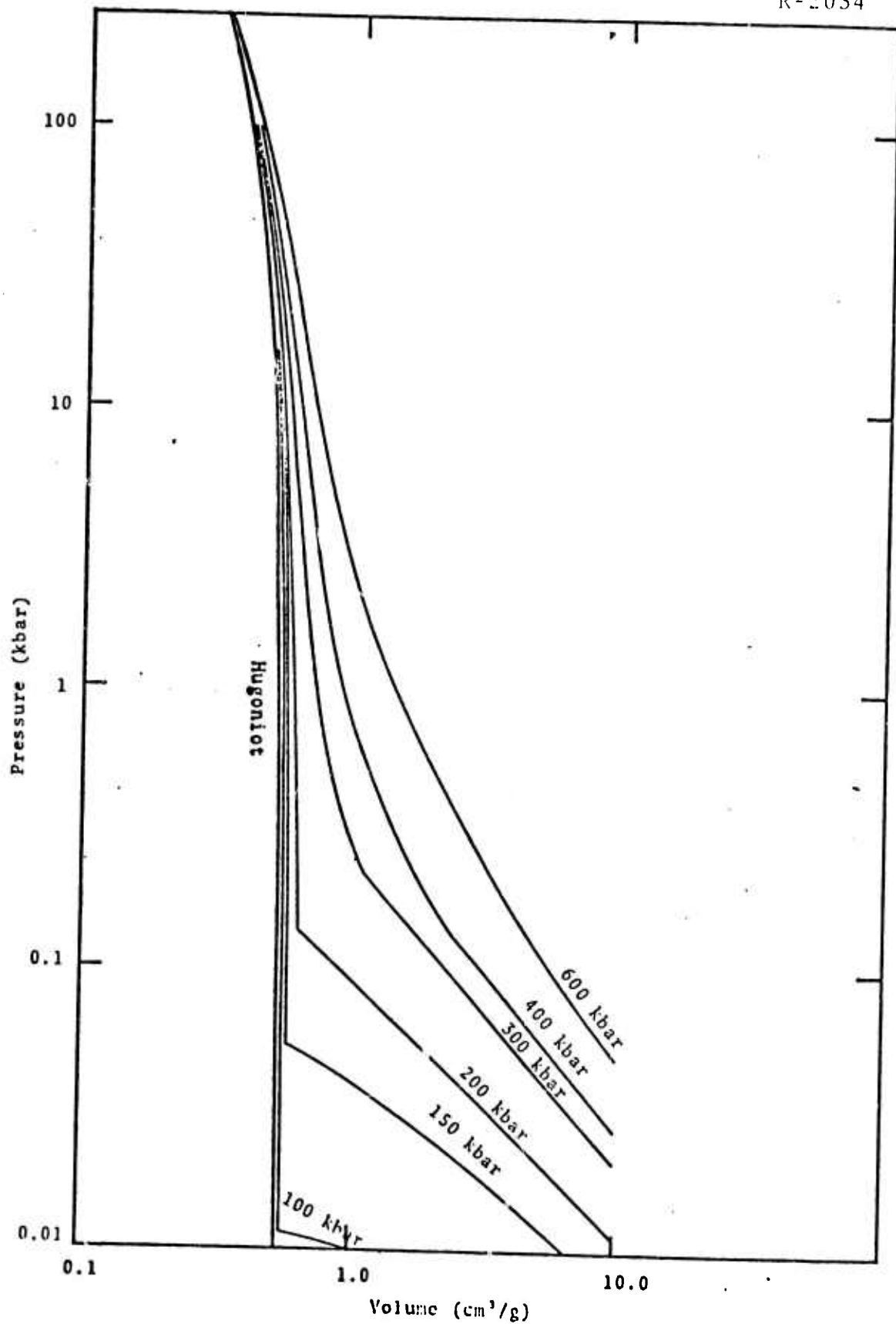
Fig. 2.2--Hugoniot and release isentropes for saturated tuff (f = 0.17).
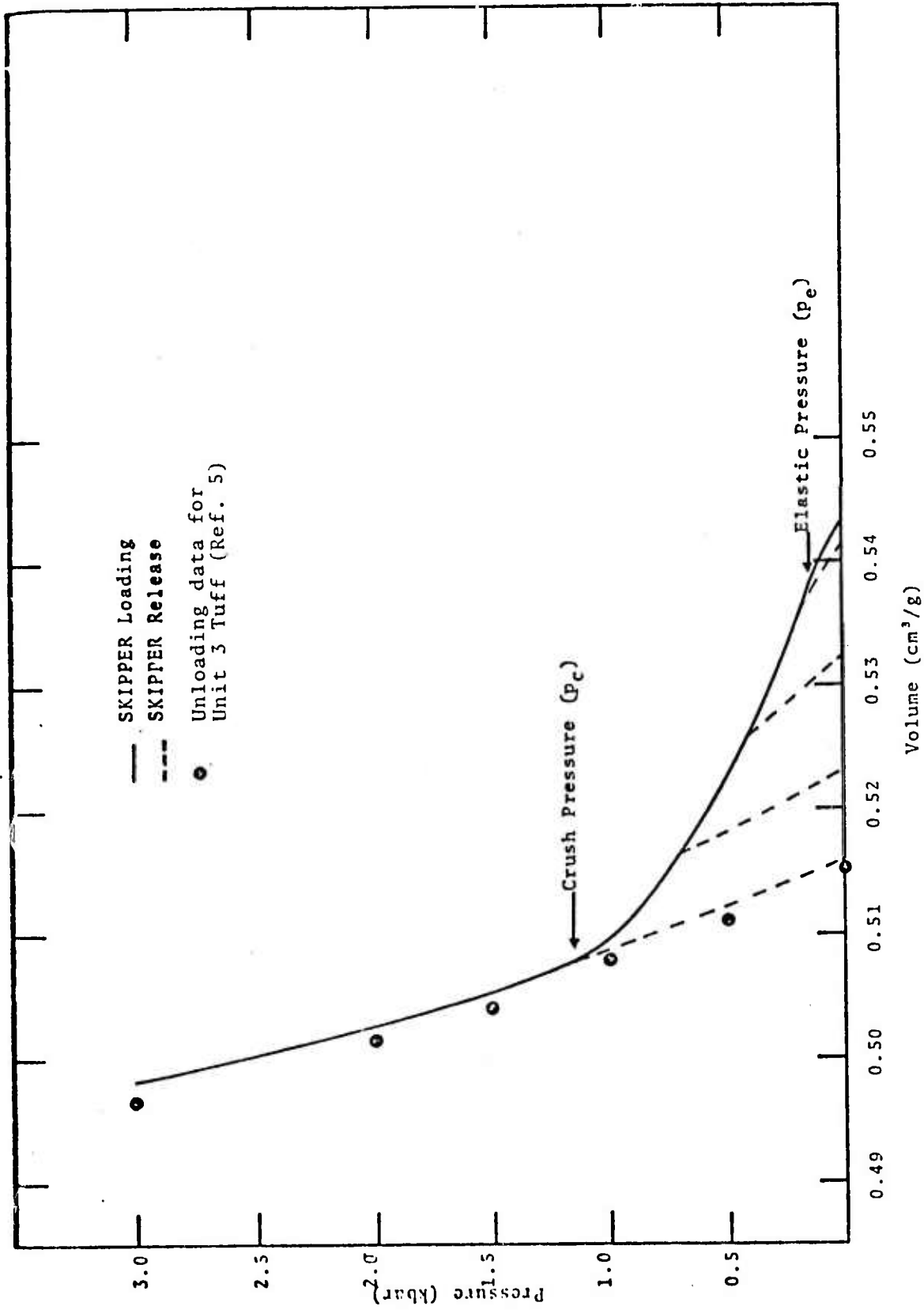
Fig. 2.3--Loading and release P-v curves for partially saturated tuff ($f = 0.17$, $\phi_0 = 0.05$).

For a given stress state in which two of the principal stresses are equal, Y_m corresponds to the maximum allowable stress difference that the material is able to support. Reported values of Y_m for the tuff from the Diamond Mine and Diamond Dust sites range between 0.4 and 2.0 kbar.[5] We have used the range as a guide for the input variable Y_m.

For spherical symmetry, Eq. (2.8) becomes

$$|S_{rr}| \leq \frac{2}{3} Y \qquad (2.10)$$

where S_{rr} is the deviatoric stress component in the radial direction. When $|S_{rr}|$ exceeds $\frac{2}{3} Y$, at some point in the SKIPPLR calculation then we set

$$S_{rr} = \frac{2}{3} Y (\text{sign } S_{rr}). \qquad (2.11)$$

This equation of state formulation has been used in order to determine the important material properties that control the source spectrum.[4] It has also been used to provide an excellent pre-shot prediction of the ground motion for the Mine Dust HE test.[6]

Most of the nuclear explosions in NTS tuff, having yields large enough to give an adequate sampling of ground motion at teleseismic distances, were below the water table. Figure 2.4 shows DOB versus $W^{1/3}$ for those events having unclassified yields.[7,8] BILBY was located in Area 3 at NTS. Pahute Mesa was the location of the remainder of the shots shown in the figure.

Since the degree of saturation depends on permeability, there is no assurance that the rock environment below the water table is completely saturated. Hence, it is instructive to show the effect of air-filled porosity of the RVP. Appropriate source calculations have been performed by Cherry, et al.,[4] and are listed as T-1, T-2, T-3, T-4 in Table 2.2. Calculations

16
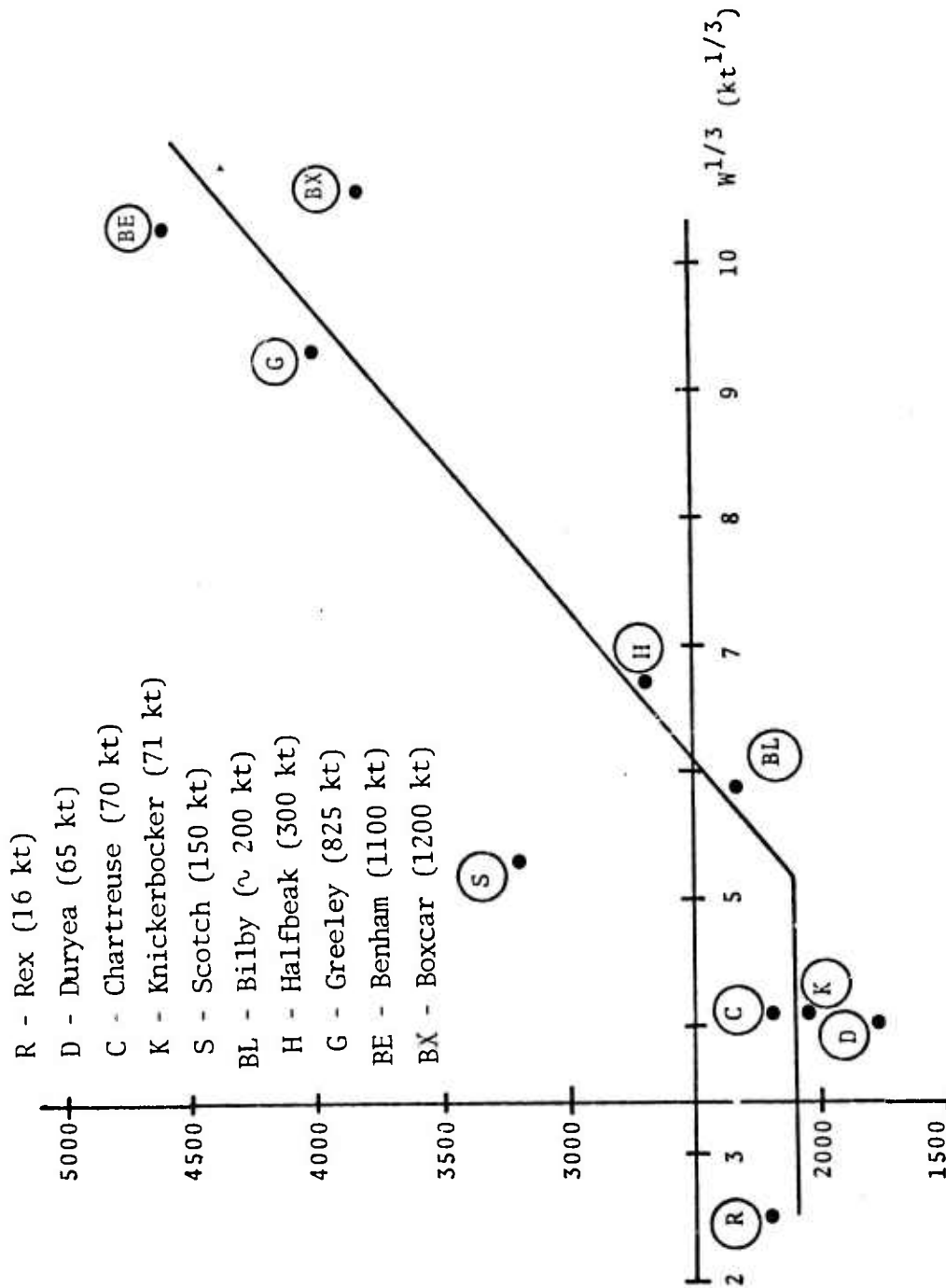
Fig. 2.4--Depth of burial (DOB) versus the cube root of the shot yield ($W^{1/3}$). The linear segment has a slope of 350 $W^{1/3}$. All events, except Bilby, were located below the water table in Pahute Mesa at NTS.

T-5 and T-6 are new and are intended to show the effect of over-burden pressure on the RVP. All the results listed in the table are for a hypothetical source yield of 0.02 kt.

TABLE 2.2

SUMMARY OF SKIPPER CALCULATIONS IN TUFF

Calculation Symbol	ϕ	Y_m(kbar)	ρ_0 gm/cc	P_0 (kbar)	R_{cav}(m)	R_{el}(m)	$\hat{\dot{\psi}}(0)$ (m³)	DOB (ft)	$m_1 - m_i$
T-1	0	0.5	1.94	0.116	3.41	27.5	7.4	2000	0
T-2	0.02	0.5	1.90	0.116	3.60	21.0	3.6	2040	0.31
T-3	0.05	0.5	1.84	0.116	3.64	18.0	2.1	2110	0.55
T-4	0.05	1.0	1.84	0.116	3.10	13.0	1.35	2110	0.74
T-5	0.05	1.0	1.84	0.179	3.0	12.0	1.25	3250	0.77
T-6	0.05	1.0	1.84	0.274	2.9	10.0	1.15	4500	0.81

In Table 2.2

ϕ_0 = volume fraction of air-filled porosity

Y_m = maximum material strength

ρ_0 = initial density

P_0 = overburden pressure

R_{cav} = calculated final cavity radius

R_{el} = calculated radius at which the stress wave enters the elastic region, i.e., the radial extent of the "shatter" zone.

$\hat{\dot{\psi}}(0)$ = zero frequency value of RVP; also equals late time value of RDP, $\psi(\infty)$

DOB = depth of burial = $P_0 (\rho_0 g)^{-1}$

$m_1 - m_i = \log_{10} \dfrac{\psi_1(\infty)}{\psi_i(\infty)}$ = approximate (assumes a flat spectrum and no surface reflection) change in M_s and m_b if material is changed from T-1 to T-i.

Parameters common to all calculations were

f = mass fraction of water = 0.17

α = compression velocity = 2.4 km/sec

P_e = elastic pressure = 0.075 kbar

P_c = crush pressure = 0.5 kbar

μ = shear modulus = 40 kbar

P_m = pressure at which material sustains maximum
  strength (Y_m) = 0.6 kbar.

Figure 2.5 compares the calculated source functions $|\hat{\dot{\psi}}|$ for T-1, T-3 and T-4. While the calculations were run using a source yield of 0.02 kt, the scaled frequency axis corresponding to a yield of 1000 kt is also given in the figure (see Table 1.1). Increasing the porosity from zero (T-1) to 0.05 (T-3) decreases the RVP by a factor of 3.5 for frequencies less than 1 Hz and yields up to 1000 kt. If, in addition, the maximum material strength, Y_m, is increased by a factor of 2.0 (T-1 to T-4), the RVP is reduced by a factor of 5.5.

The effect of the various source functions $|\hat{\dot{\psi}}|$ of Fig. 2.5 on body wave and surface wave magnitude are given in Table 2.2 in the m_1-m_i column. From the table we find that increasing the dry porosity from zero (T-1) to 0.02 (T-2) causes a magnitude decrease of 0.31. The effect of air-filled porosity on $\hat{\dot{\psi}}(0)$ is shown in Fig. 2.6. Since $\hat{\dot{\psi}}(0)$ scales as the device yield (Table 1.1), then 1 kt in T-1 is equivalent to 3.7 kt in T-3.

Finally the effect of increased depth of burial on $\hat{\dot{\psi}}(0)$ is available from calculations T-4, T-5 and T-6. Increasing the DOB from 2110 ft (P_0 = 116 bars) to 4500 ft (P_0 = 247 bars) causes a magnitude decrease of only 0.07 units (0.74 - 0.81). As shown in Section IV, the major DOB effect on m_b is caused by the interference between P and pP.
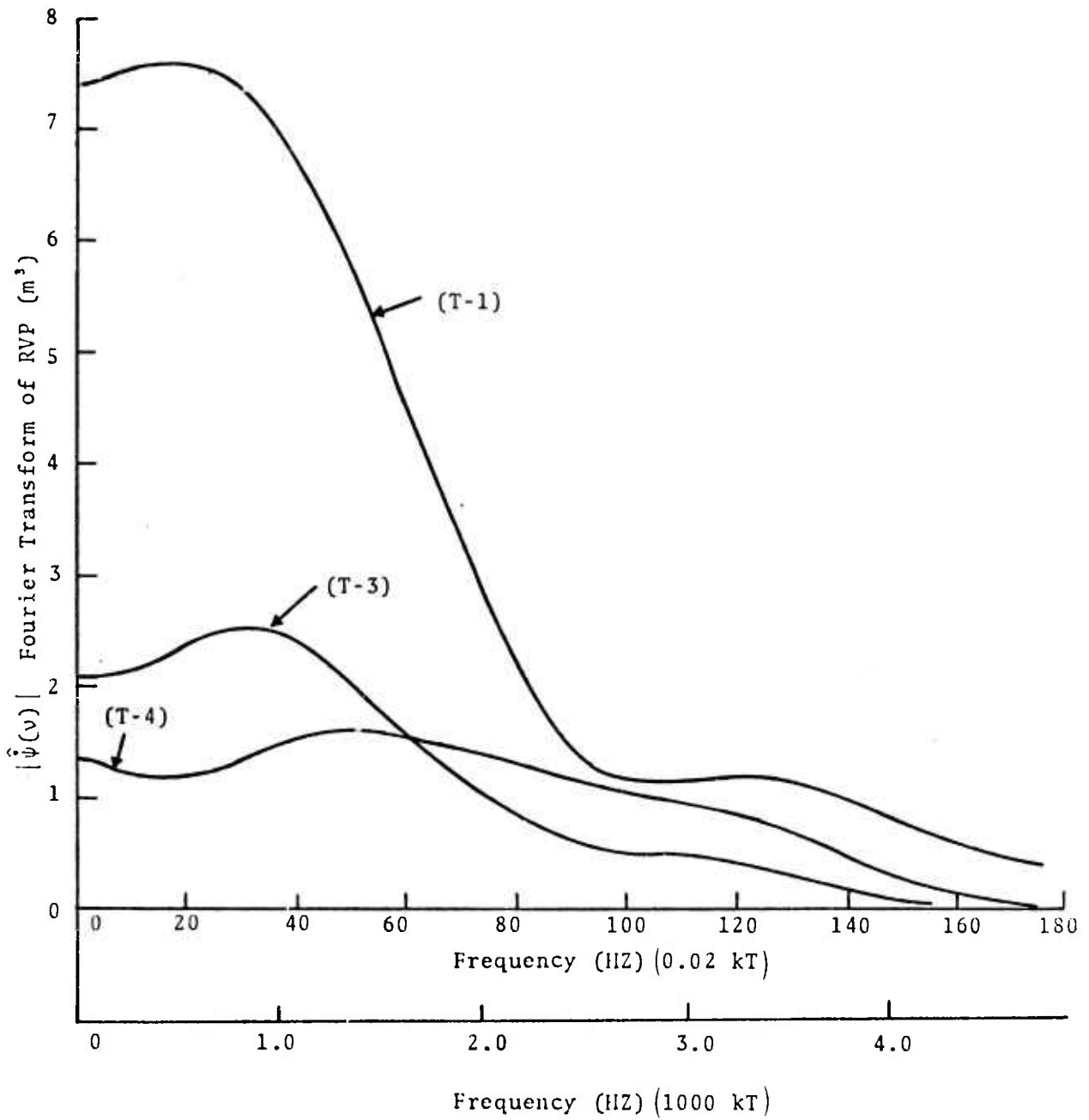
Fig. 2.5--Comparison of source functions for 0.02 kt from Calculations (T-1), (T-3) and (T-4).
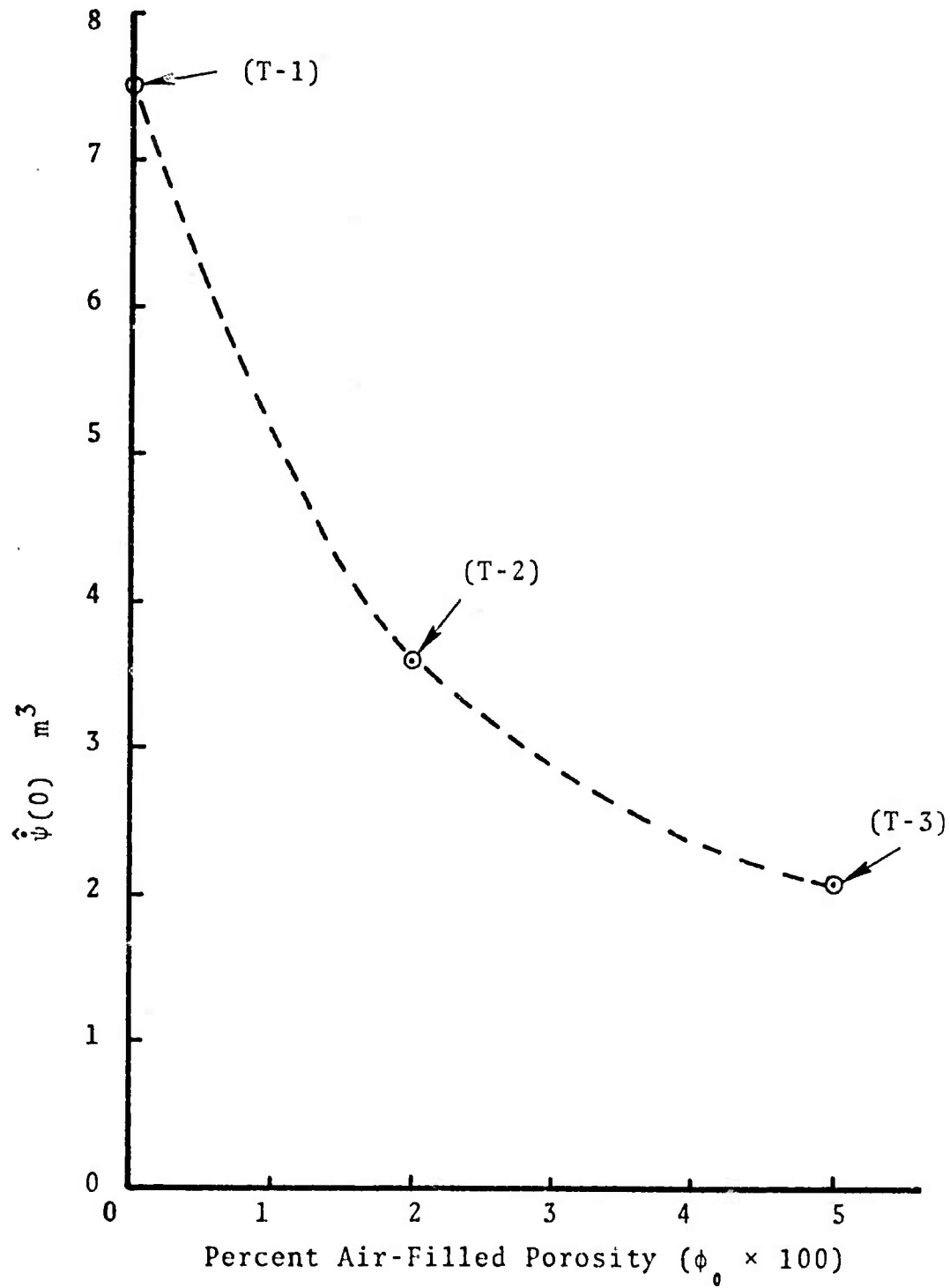
Fig. 2.6--Effect of air filled porosity on $\hat{\dot{\psi}}(0)$ for Calculations (T-1), (T-2) and (T-3).

2.3   SANDSTONE

Rulison and Rio Blanco were nuclear explosive, gas stimulation experiments in sandstone. The Rulison experiment was located in the Rulison basin of Colorado, where a single 40 kt device was detonated at a depth of 8442 ft. Rio Blanco was in the Piceance Basin where three 30 kt devices were simultaneously detonated in a vertical emplacement hole at depths of 5840, 6230 and 6690 feet.

An equation of state for sandstone was developed from quasistatic test data published by Schock, et al.,[9] and high pressure sandstone Hugoniot data published by Terhune.[10] Figure 2.7 shows pressure versus specific volume developed from the quasistatic tests. Figure 2.8 merges the static data in the P-v plane with the high pressure Hugoniot data. The maximum stress difference allowable under shock loading was taken to be Y_m = 4.3 kbar. This was assumed to occur at P_m = 10 kbar. The material strength relation is given by Eq. (2.9).

TABLE 2.3
SUMMARY OF SKIPPER CALCULATIONS IN SANDSTONE

Calculation Symbol	α km/sec	Y_m(kbar)	P_m(kbar)	ρ_0(gm/cc)	P_0(kbar)	R_{cav}(m)	R_{el}(m)	DOB (ft)	$\dot{\xi}(0)$ (m^3)
S-1	3.7	4.3	10	2.52	0.5	2.3	16	6300	2.0
S-2	3.7	4.3	10	2.52	0.6	2.2	14	8400	1.8

The results of Table 2.3 are for a hypothetical source yield of 0.02 kt and may be compared directly with those listed for tuff in Table 2.2. S-1 corresponds to a DOB appropriate for Rio Blanco while S-2 was run at the Rulison depth.

Figures 2.9 and 2.10 show the calculated source functions for S-1 and S-2. These sandstone source functions are similar to the T-3 RVP for tuff shown in Fig. 2.5. Given the same source function for different materials, body wave amplitudes will depend only on the compressional velocity, α, in Eq. (2.1).
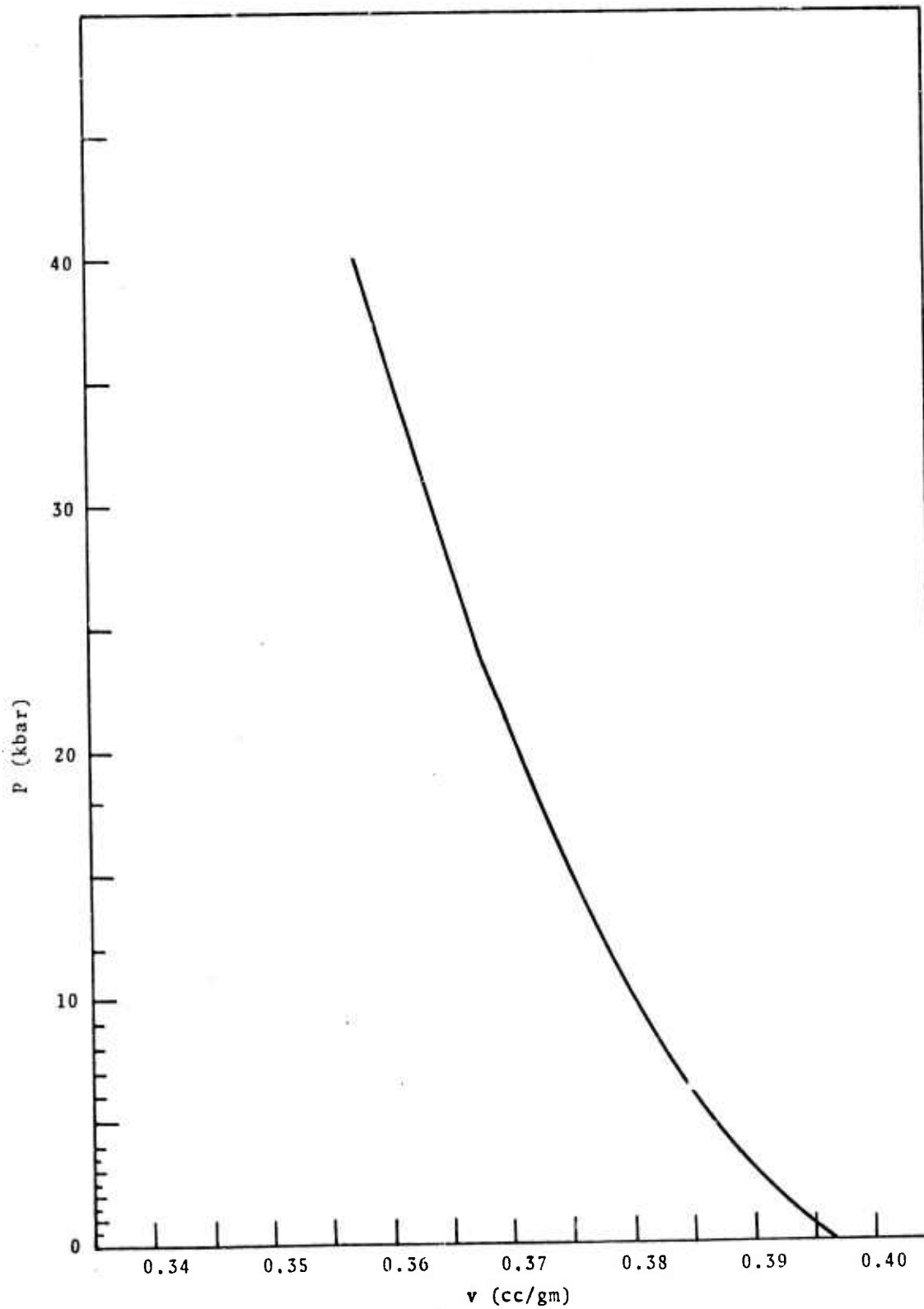
Fig. 2.7--Pressure (P) versus specific volume (v) for sand-[9] stone from the static test data of Schock, et al.

23
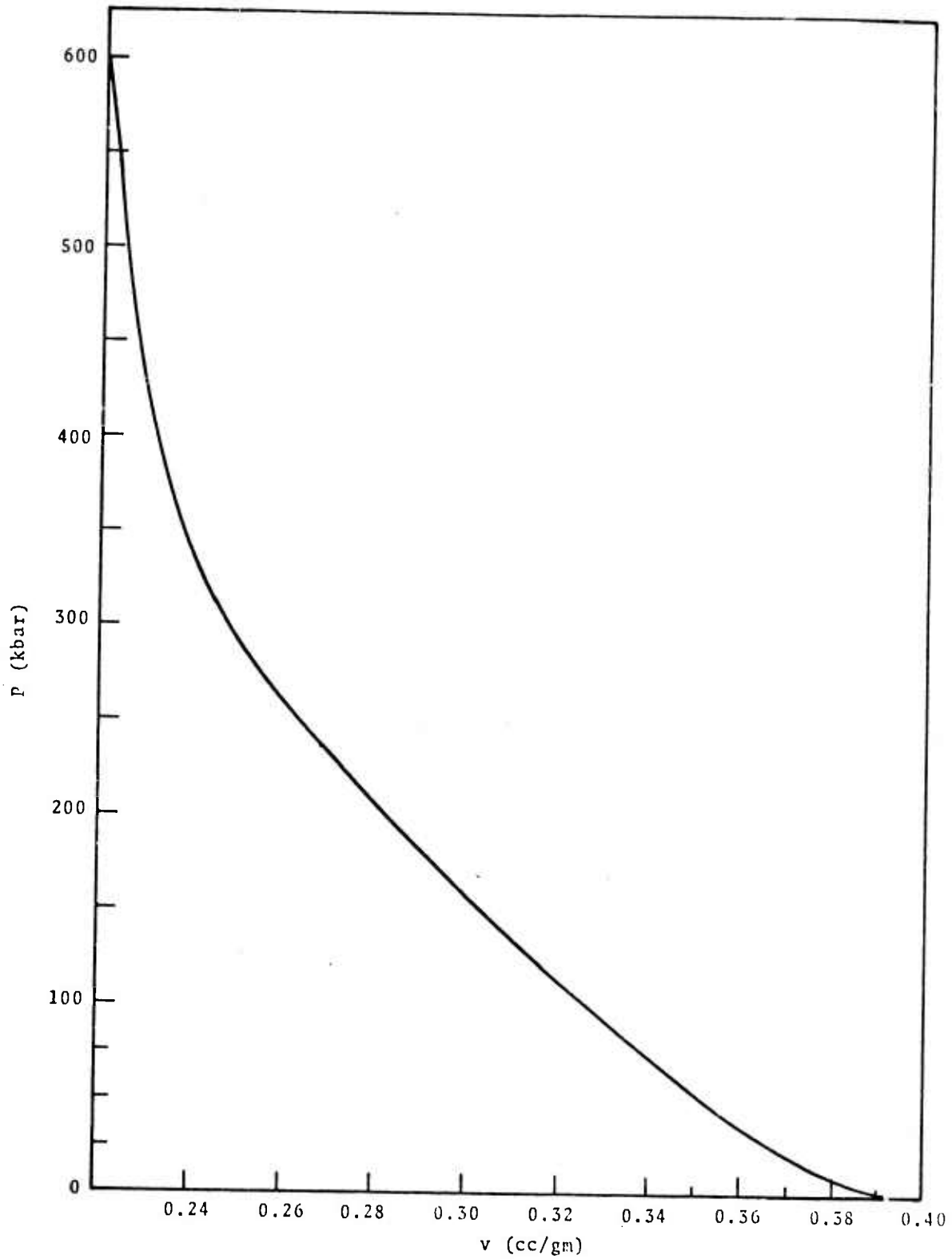
Fig. 2.8--Pressure (P) versus specific volume (v) for sand-
stone, merging the low pressure data of Fig. 2.7
with the high pressure Hugoniot data reported by
Terhune.[10]
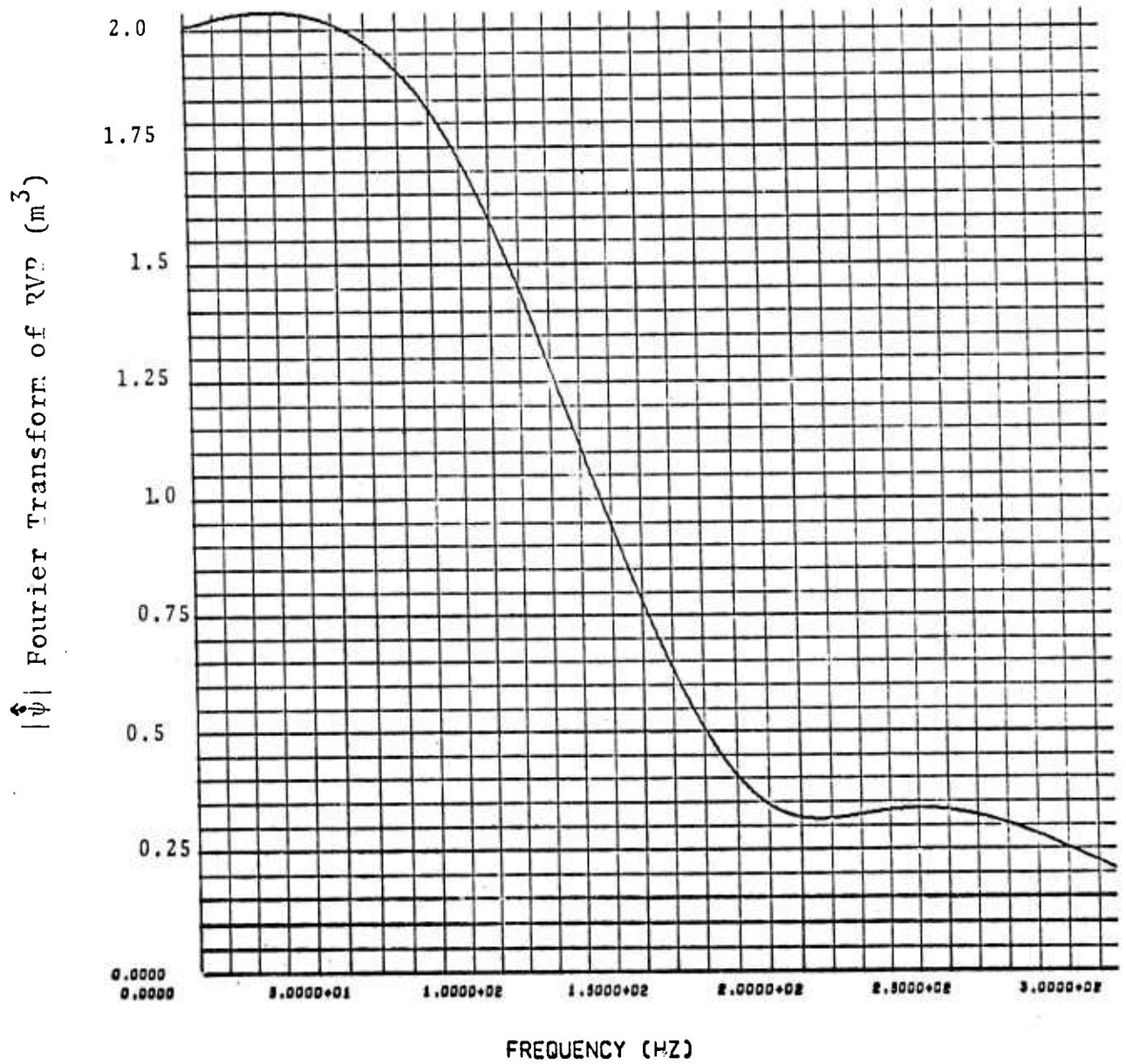
Fig. 2.9--$|\hat{\psi}|$ for 0.02 kt, Calculation S-1.
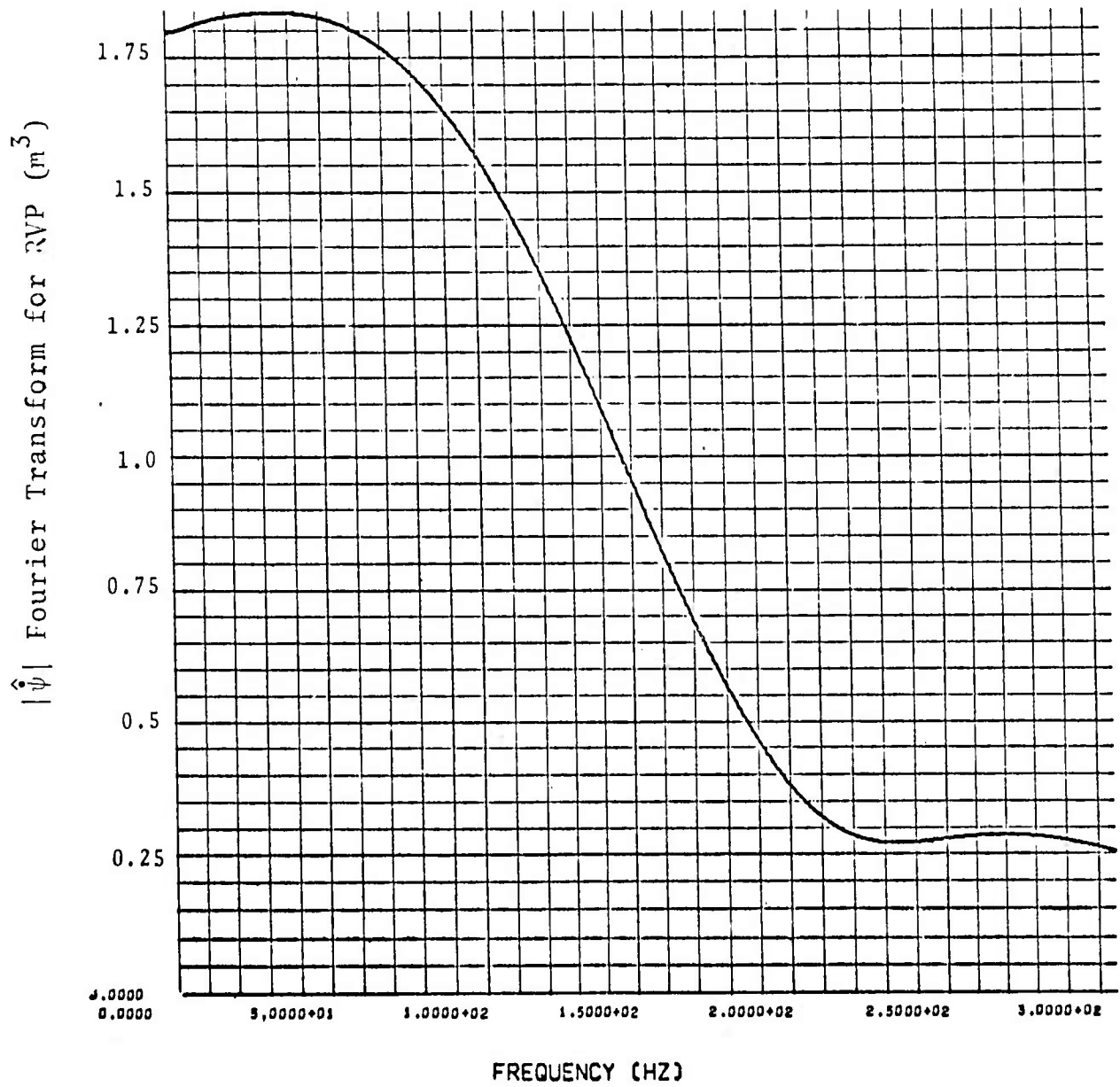
Fig. 2.10--$|\hat{\dot{\psi}}|$ for 0.02 kt, Calculation S-2.

The results given in Tables 2.2 and 2.3 also show that the final cavity radius (R_{cav}) is not simply related to $\dot{\hat{\psi}}(0)$ or, equivalently, $\psi(\infty)$. For example, S-1 and T-3 have almost identical values of $\psi(\infty)$ but quite different final cavity radii. It is therefore important that Eq. (2.6) only be applied to the elastic region defined by $r \geq R_{el}$.

2.4 GRANITE

Granite source functions have been calculated based on the NTS granite compressibility data of Stephens and Lilley[11] and the strength data of Heard.[12] Figure 2.11 is taken from Heard and shows the effect of water content (pore pressure) on the strength of Hardhat granodiorite. The dry granite is three times stronger than wet granite in which the pore (fluid) pressure equals the confining pressure.

Two calculations were run at hypothetical yields of 0.02 kt changing only the material strength. The calculation G-1 used the dry strength data of Fig. 2.11 and G-2 used the wet strength data shown in the figure. The source functions for these two calculations are shown in Figs. 2.12 and 2.13. The results of the calculations are summarized in Table 2.4.

TABLE 2.4

SUMMARY OF SKIPPER CALCULATIONS FOR GRANITE

Calculation Symbol	α km/sec	Y_m (kbar)	P_m (kbar)	ρ_0 (gm/cc)	P_0 (kbar)	R_{cav} (m)	R_{el} (m)	DOB (ft)	$\psi(0)$ (m³)
G-1	5.6	20	22	2.67	0.120	1.82	33.6	1500	2.2
G-2	5.6	6.67	22	2.67	0.120	2.51	65.9	1500	8.2

The overburden pressure, P_0, was chosen to correspond to the DOB of Piledriver, a 60 kT event in granite at NTS. "Free field" ground motion from this event was processed by William R. Perret at Sandia Laboratory. The reduced

27
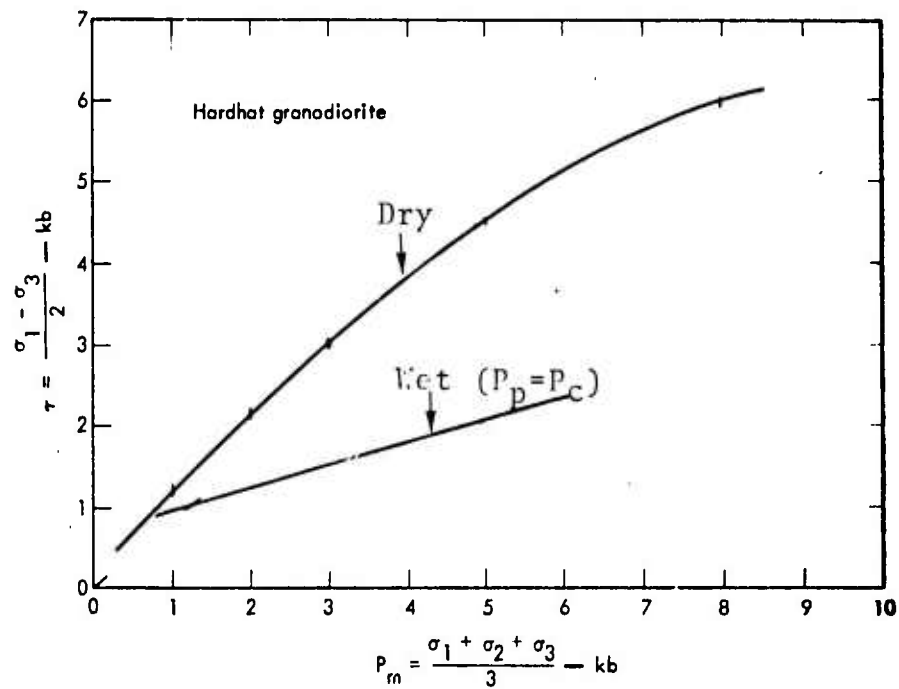
Fig. 2.11--Failure envelopes for Hardhat granodiorite tested in compression, 25°C, at a strain rate of 10^{-4}/sec, from Heard [12].

28
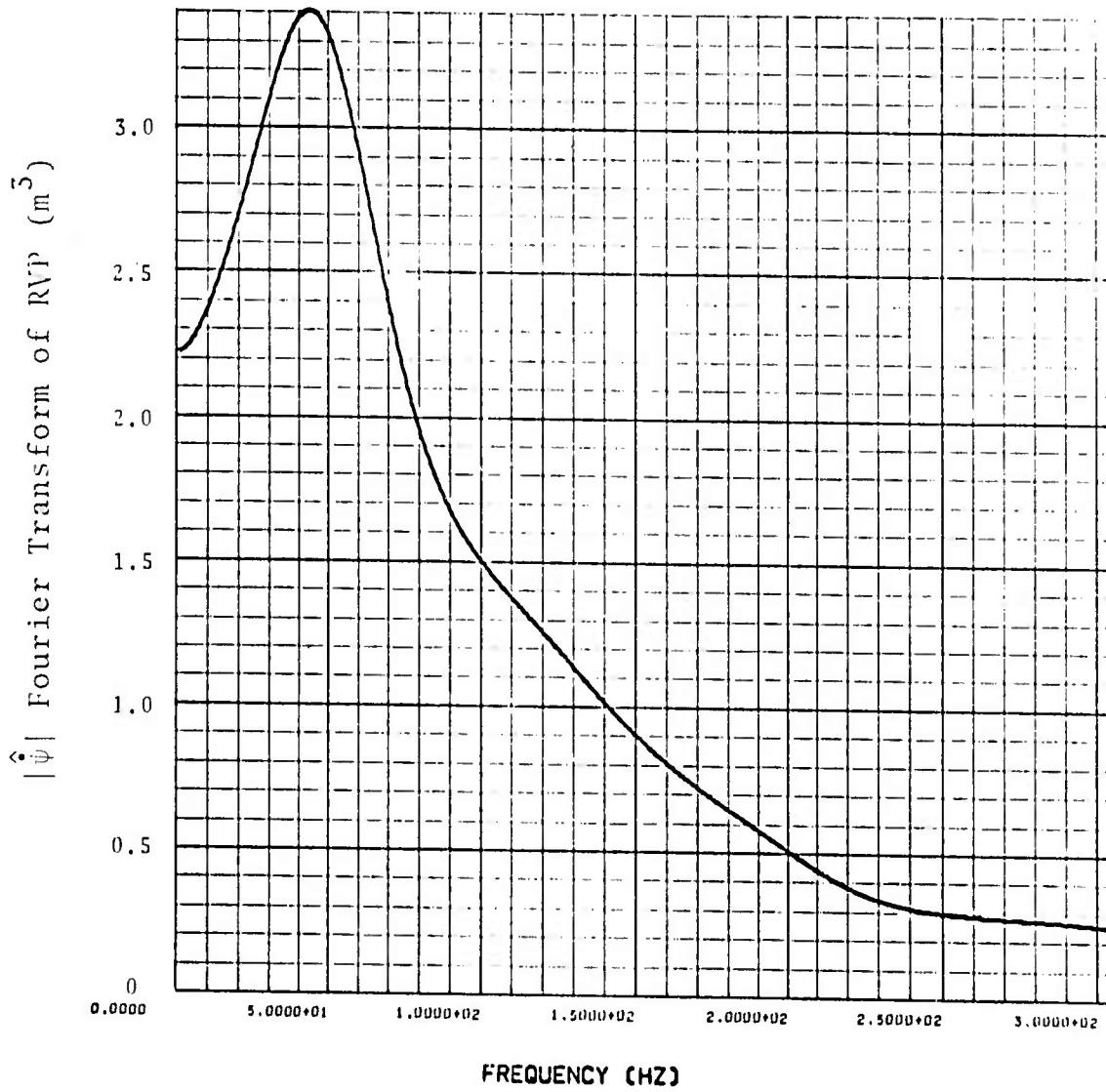
Fig. 2.12--$|\hat{\dot{\psi}}|$ for 0.02 kt, calculation G-1.
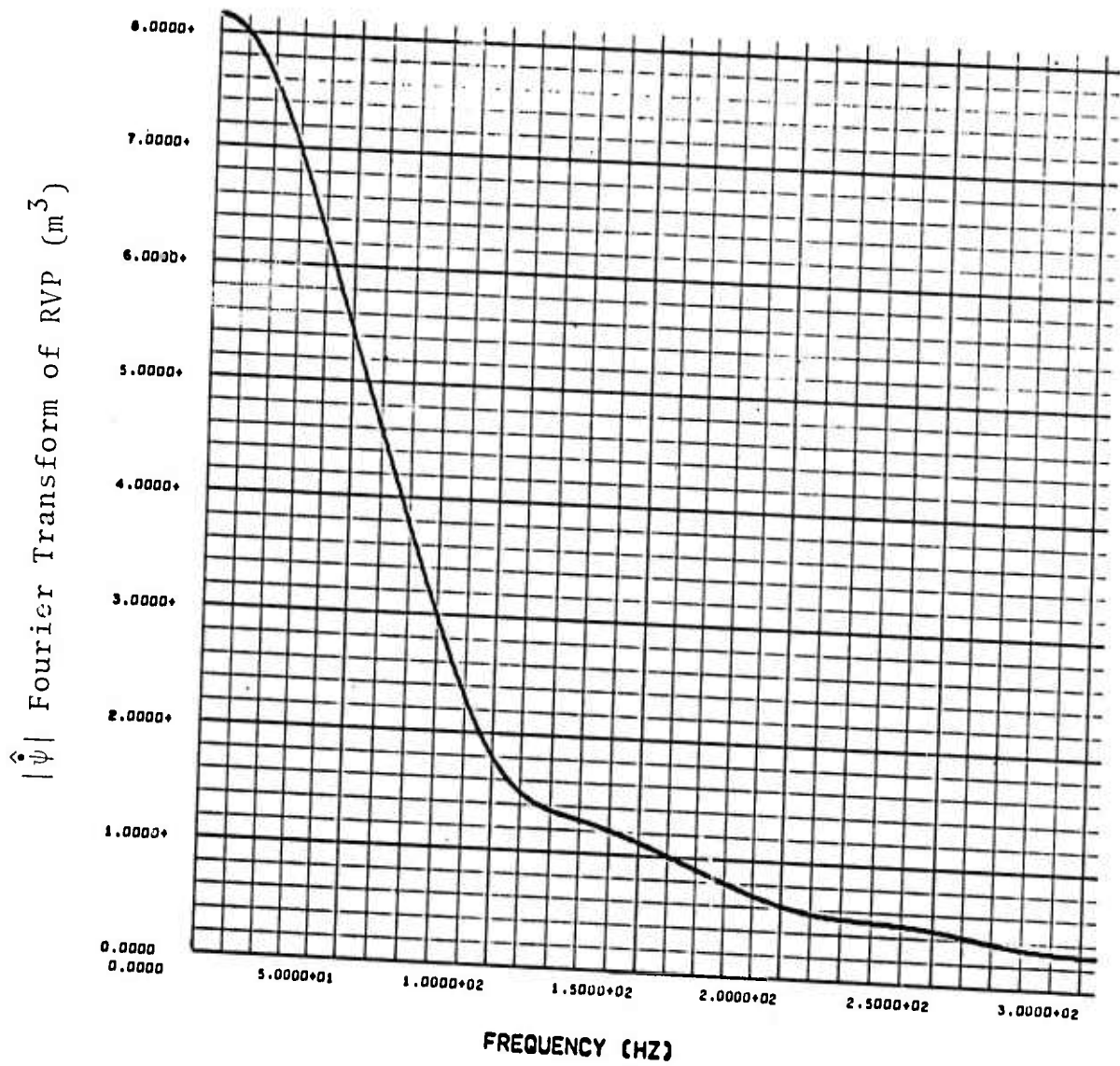
Fig. 2.13--$|\hat{\dot{\psi}}|$ for 0.02 kt, calculation G-2.

displacement potentials that he obtained, scaled to 0.02 kt
at Station 2403 (r = 2000 ft), Station 1503 (r = 2803 ft)
and Station 2803 (r = 2803 ft), are shown in Figs. 2.14, 2.15
and 2.16. The calculated RDP from G-1 and G-2 are given in
Figs. 2.17 and 2.18.

The agreement between the calculated and observed re-
duced displacement potentials is poor. Even though $\psi(\infty)$
from G-2 compares reasonably well with $\psi(\infty)$ from Stations
2403 and 2803 (8.2 m^3 versus 10.8 m^3 and 9 m^3), the time at
which $\psi(\infty)$ is attained is at least an order of magnitude
different between the calculated source function G-2 and
that observed at the two stations.

A possible explanation for the discrepancy is that the
observed ground motion at the three stations is not really
free field, i.e., additional arrivals have obscured the true
nature of the equivalent source from the explosion. For
example, the free surface reflection should arrive at Station
2403 at approximately 0.015 sec, where this time has been
scaled to 0.02 kt. Referring to Fig. 2.14, this arrival
occurs during the excursion of the RDP to its peak value of
16.1 m^3. Release of tectonic stress would be another possi-
bility and may explain the azimuthal variations of the RDP
from Station 1503 and 2803.

If the observed ground motion at the three stations
is indeed contaminated by additional events, then none of
the source functions from these stations will explain the
teleseismic observations from Piledriver and we will have
to depend on calculated source functions to explain the tele-
seismic data.

31
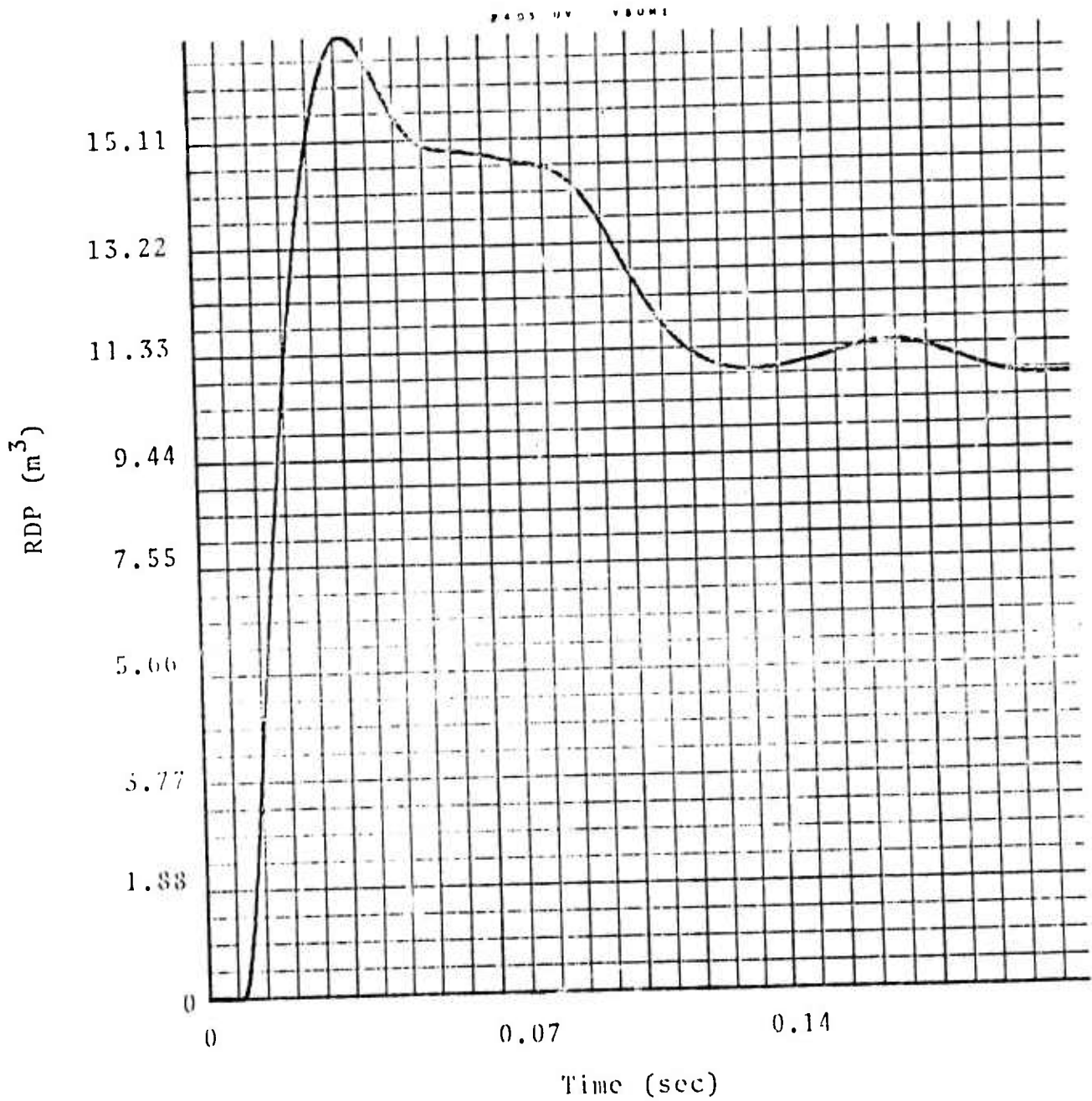
Fig. 2.14--Reduced displacement potential (RDP) at Station 2403 for Piledriver, scaled to 0.02 kt.
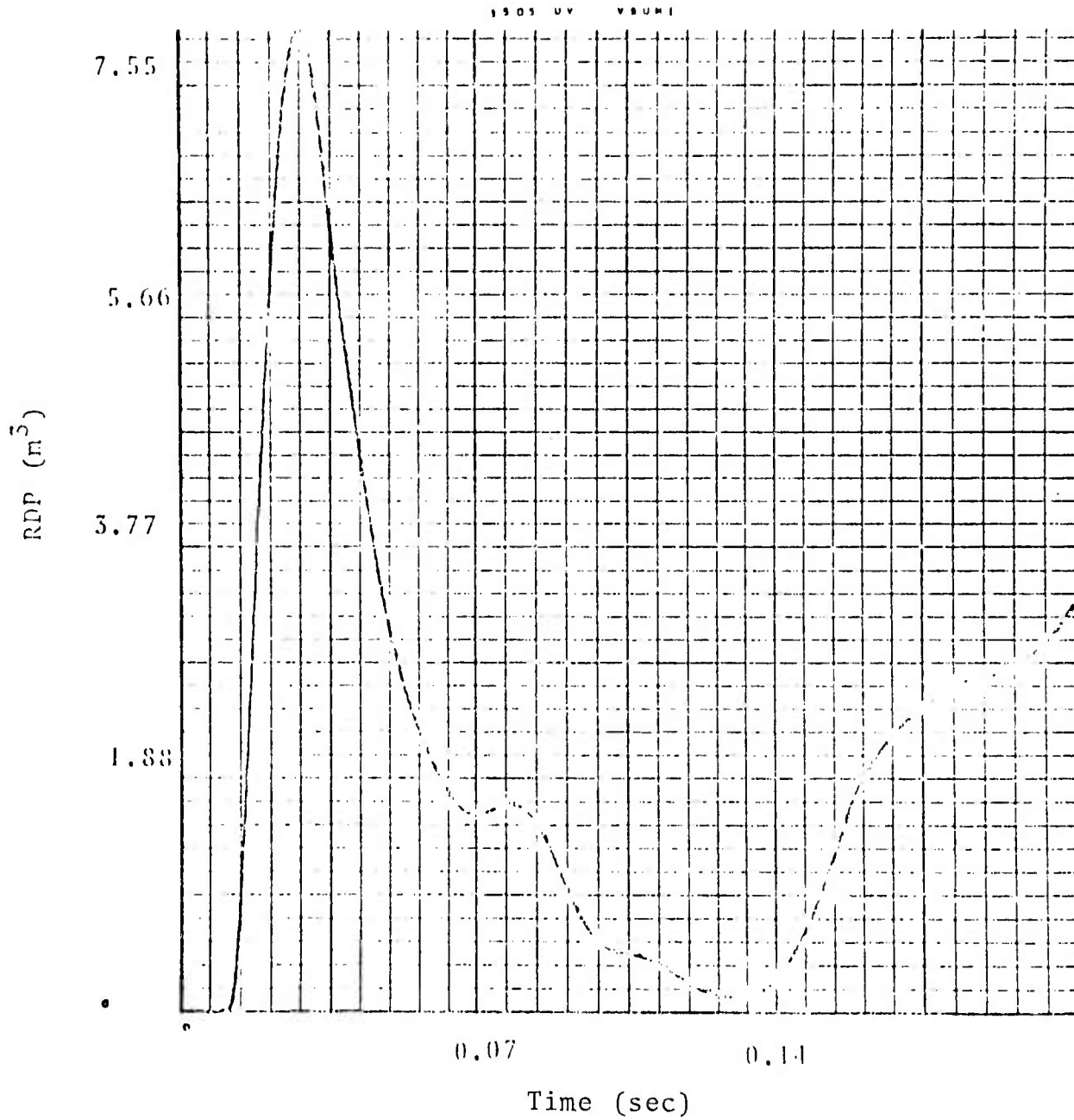
Fig. 2.15--Reduced displacement potential (RDP) at Station
1503 for Piledirver, scaled to 0.02 kt.
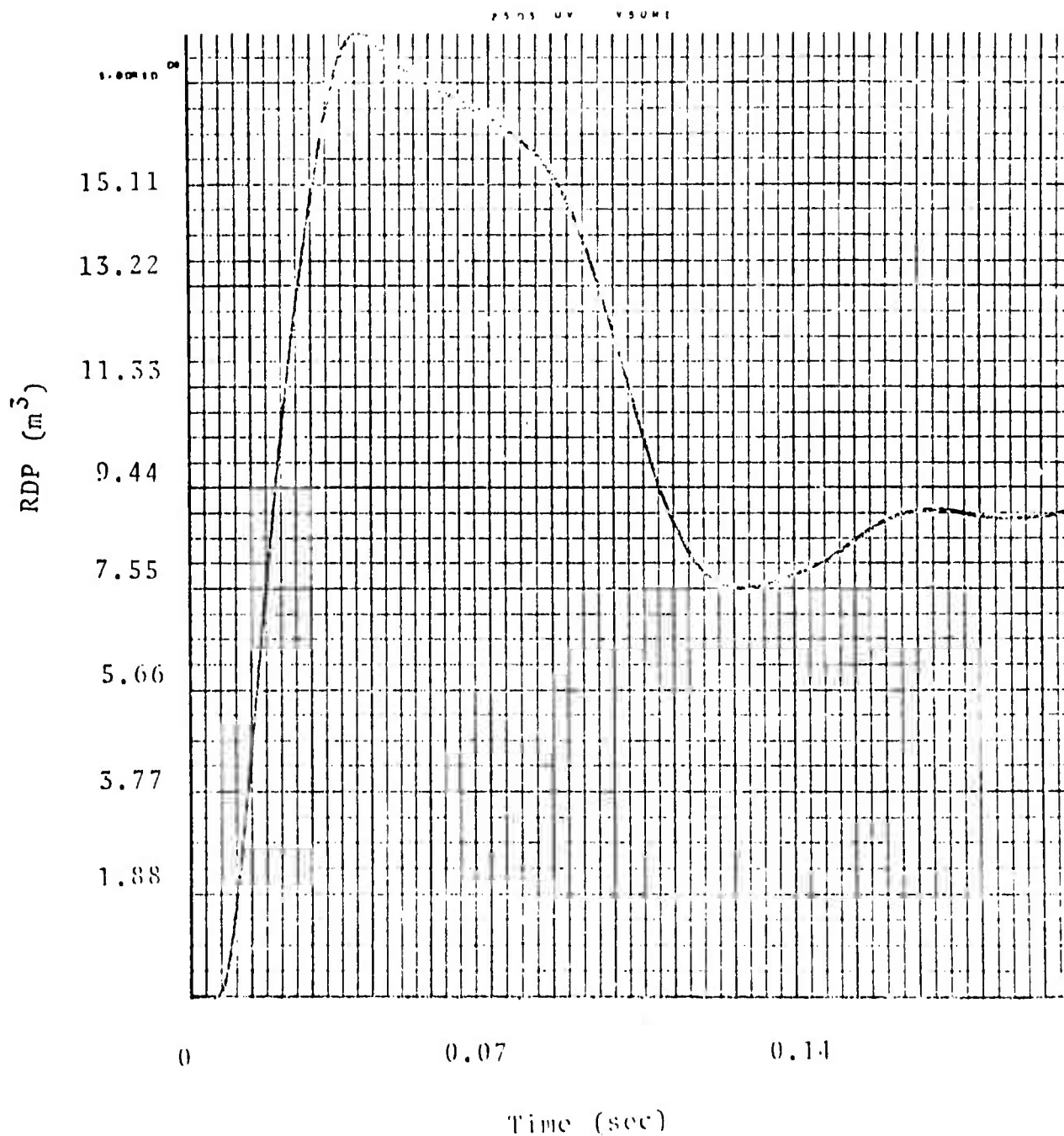
Fig. 2.16--Reduced displacement potential (RDP) at Station
2503 for Piledriver, scaled to 0.02 kt.
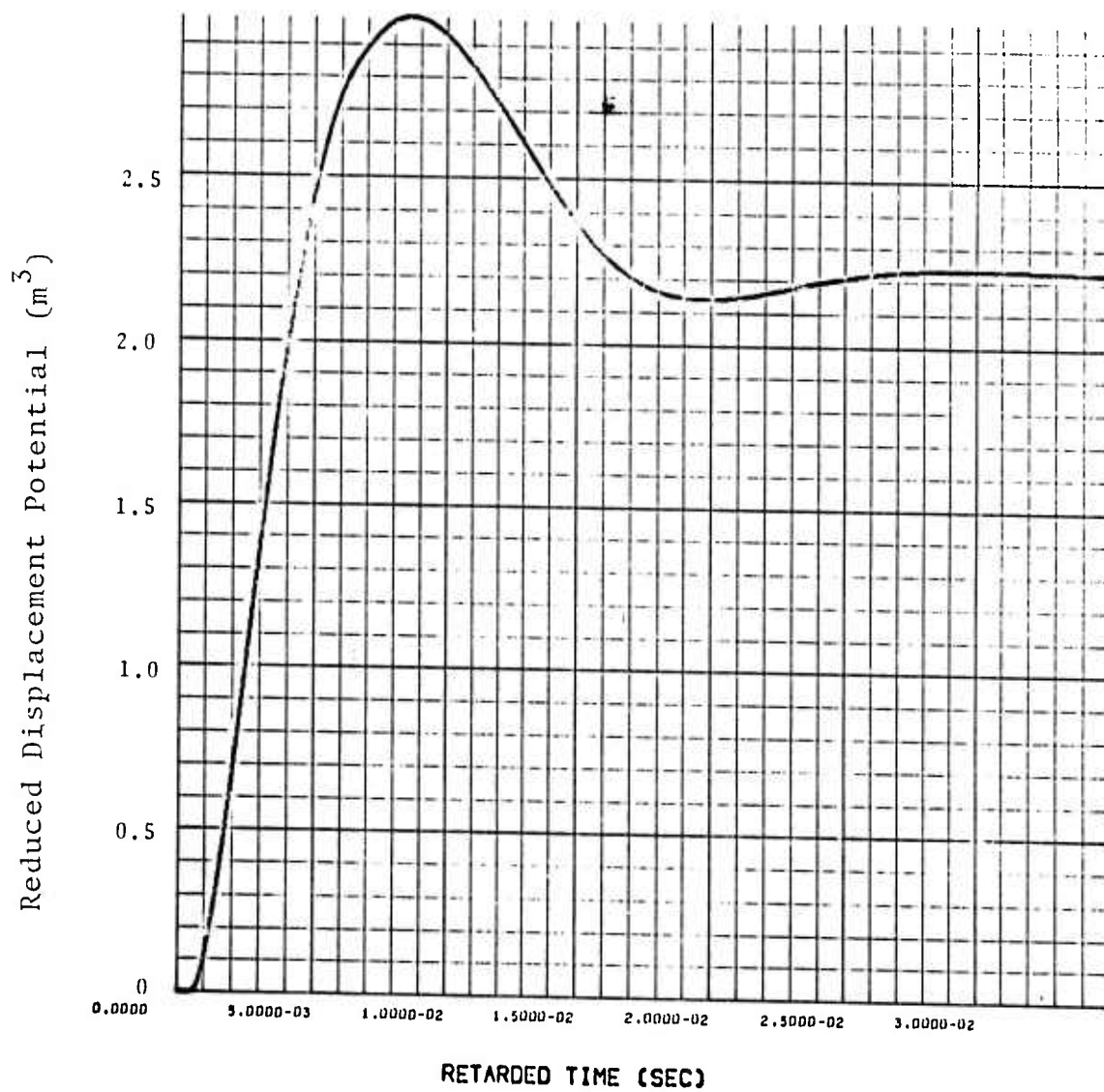
Fig. 2.17--Reduced displacement potential for calculation G-1.
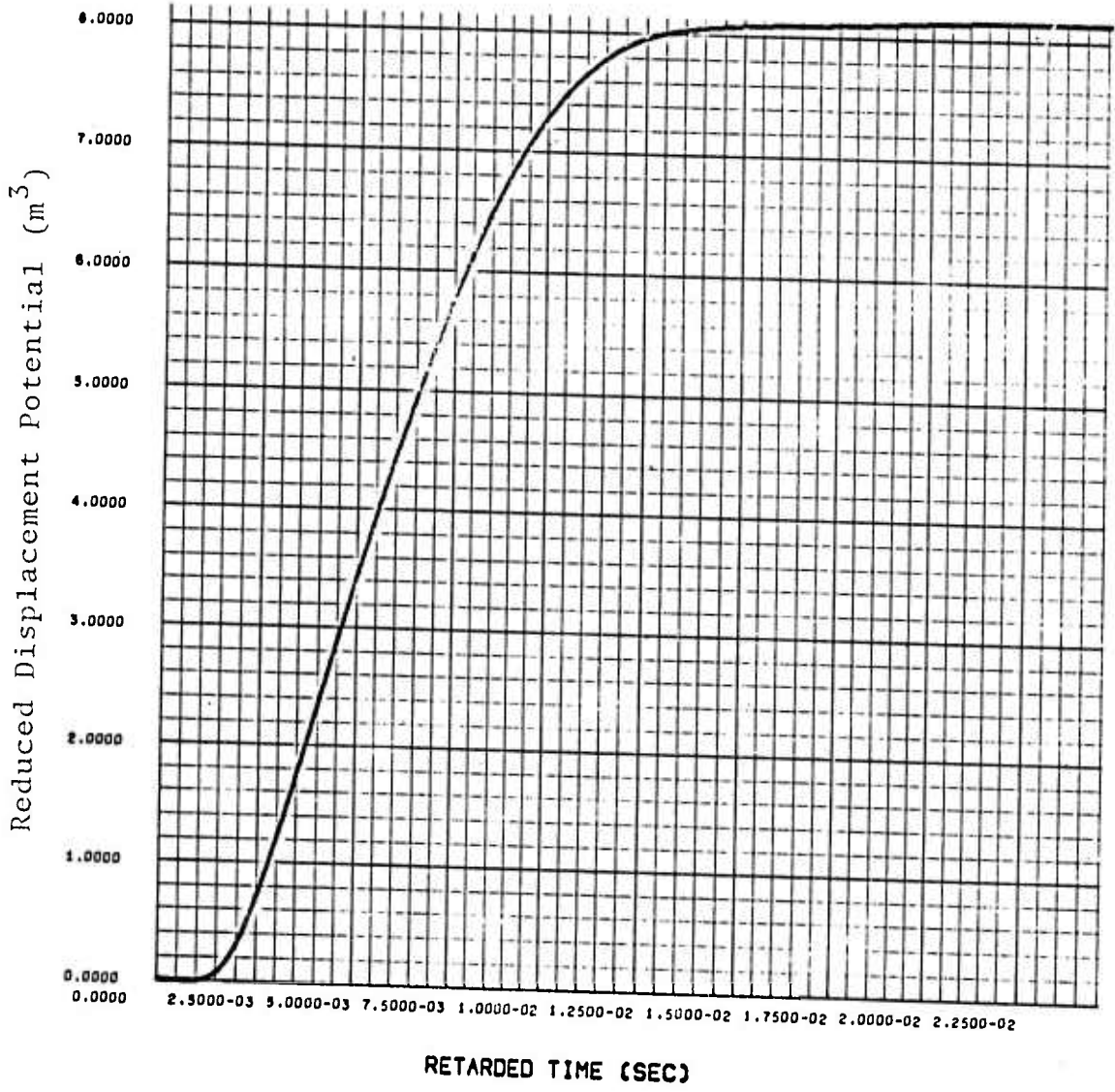
Fig. 2.18--Reduced displacement potential for calculation G-2.

III. SURFACE WAVES FROM UNDERGROUND EXPLOSIONS

3.1 INTRODUCTION

The surface waves radiated by underground explosions in general include both Rayleigh and Love waves. A computational method for generating synthetic seismograms for these surface waves has been developed by Harkrider[2] and made operational at S^3. The explosion source functions described in Section II may be input to the surface wave computer codes and the resulting teleseismic surface waves are then generated.

Treating the explosion as a spherically symmetric source (e.g., the SKIPPER calculation), only surface waves of the Rayleigh type are generated. The surface wave signature is then dependent on the steady state value of the reduced displacement potential ($\psi(\infty)$) and the velocity profile of the crust and upper mantle between source and receiver. The Rayleigh wave seismic record for this case is only weakly dependent on other parameters such as the burial depth of the explosion.

Many studies of surface waves from underground explosions [e.g., 13, 14] have concluded that some mechanism other than a spherically symmetric source was operational. Indications of this secondary phenomenon have included strong Love wave radiation and an azimuthal dependence of Rayleigh wave amplitudes. A superposition of a double-couple (quadrupole) source on the point source (monopole) due to the explosion has been successful in matching these observations. [13-16] A theory of tectonic stress release from explosions in prestressed media has been formulated by Archambeau[17] to calculate the double-couple contribution to the source. This theory has been included in our surface wave computational capability.

Teleseismic surface waves and the measurement of surface wave magnitude, M_s, are sensitive to both the explosion and the tectonic stress release contributions to the source. Many parameters enter into a specification of tectonic release and a detailed study of this contribution was not conducted for the surface waves. Our primary attention is directed to isolating the pure explosion component and determining its effect on teleseismic surface waves.

3.2 TELESEISMIC SURFACE WAVE CODES

The technique for propagating surface waves in a layered earth medium is described by Harkrider. [2] The earth structure is modeled using homogeneous isotropic layers and the response of the multilayered system is calculated using linear wave propagation theory for the vertically trapped modes of propagation. The eigenfunction can be calculated for any depth in the model.

The source is specified by the spherical wave multipole coefficients describing an equivalent elastic source. For explosions with tectonic release, only the monopole and quadrupole terms are required. The spherical wave coefficients are then converted to the corresponding cylindrical wave expansion coefficients associated with the set of potentials employed in the surface wave programs. These coefficients then serve as excitation factors in the Love and Rayleigh wave programs and combine with the eigenfunctions for the layered system to give predicted surface wave spectra at teleseismic distances.

The synthesis code uses the eigenvalues and eigenfunctions appropriate to the explosion depth to calculate the spectra at selected distances from the source. Anelastic absorption along the propagation path is computed using values of observed wave decay constants. The effect of the

38

earth's curvature on geometric spreading is also included.

Finally, synthetic seismograms are generated by a numerical transformation of the far field spectrum into the time domain. Suitable seismograph amplitude and phase response data may be included to construct a synthetic seismogram for a given instrument.

3.3. RAYLEIGH WAVES FROM UNDERGROUND EXPLOSIONS

The source functions calculated by the SKIPPER code (Section II) may be input to the surface wave codes to obtain teleseismic Rayleigh waves. The important parameters controlling this synthesis are the limiting values of the RDP $(\psi(\infty))$, the earth structure and, weakly, the depth of burial. The effect of these parameters is studied in this section.

3.3.1 Earth Structure

The influence of changing the velocity profile of the crust and upper mantle is indicated by performing several calculations using different models. Velocity-depth profiles for the three earth structure models studied are given in Fig. 3.1. All three models are intended for the structure in the vicinity of NTS and are therefore rather similar.

Synthetic seismograms at 4000 km from the three earth structure models are presented in Fig. 3.2. These seismograms include the effect of an LRSM Long Period seismometer. The relative magnification of this instrument is shown in Fig. 3.3. The seismograms are appropriate to the Piledriver event which was a 61 kt explosion at a burial depth of 463 meters in NTS granite. The SKIPPER source function G-1 was used (see Section 2.4).
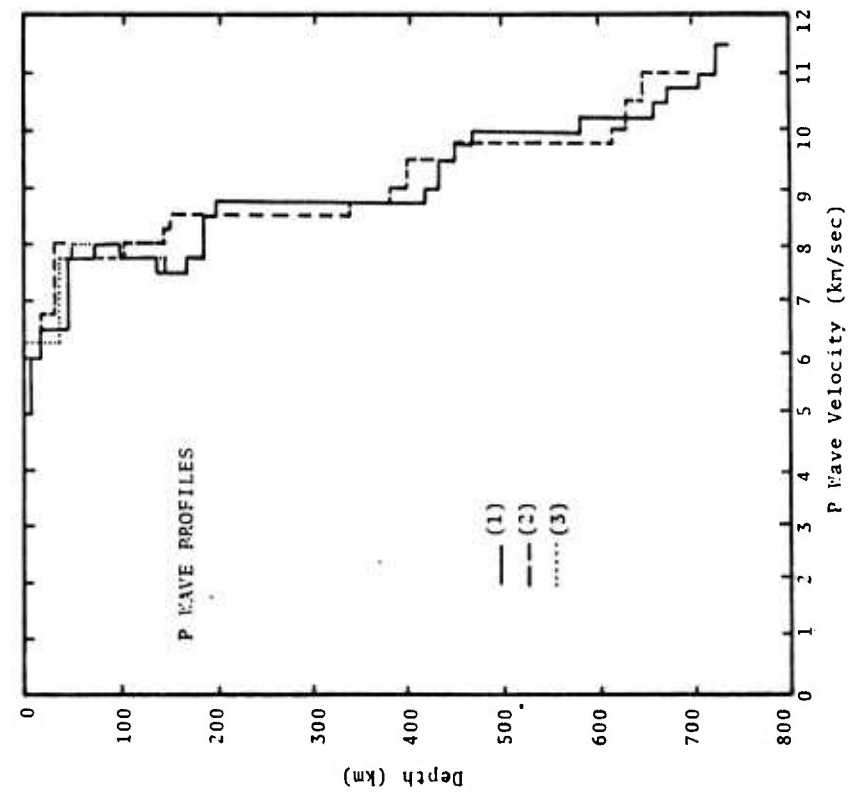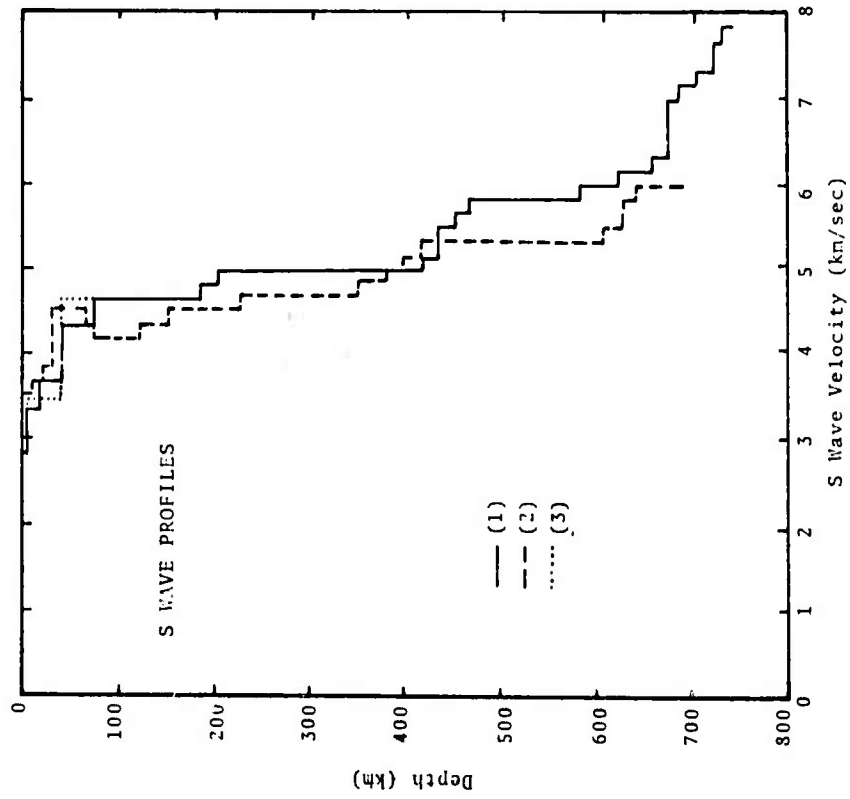
Fig. 5.1--P and S wave velocity versus depth for three models of the crust and upper mantle. Line (1) is Fallon to Ruth crust, over Helmberger mantle; line (2) is model CIT 109; line (5) is NTS Granite crust over Helmberger mantle.

40
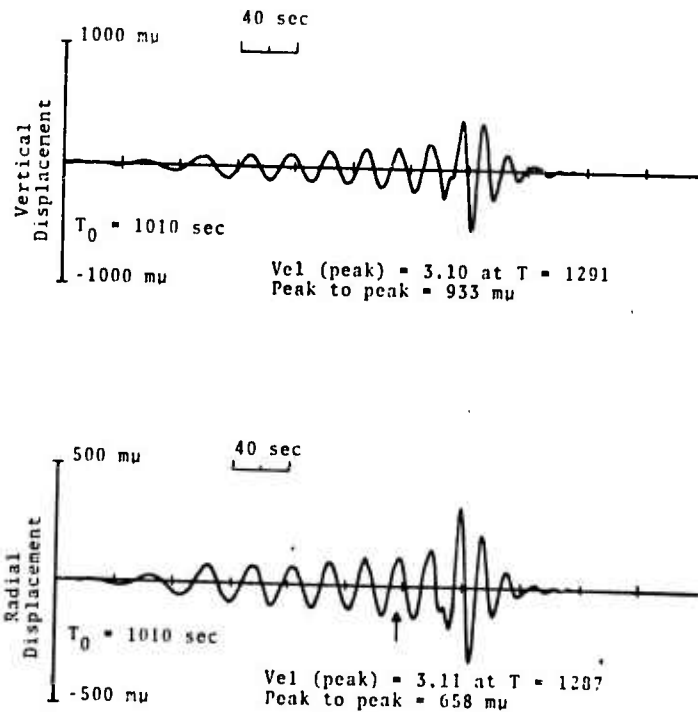
(a) Earth structure CIT 109.

Fig. 3.2--Rayleigh wave synthetic seismograms for the Piledriver event using three earth structure models. SKIPPER source G-1, epicentral distance 4000 km, depth of burial 463 meters, LRSM Long Period Seismograph. The 20 second phase on the radial motion record is indicated (↑).

Fig. 3.2 (Cont.)
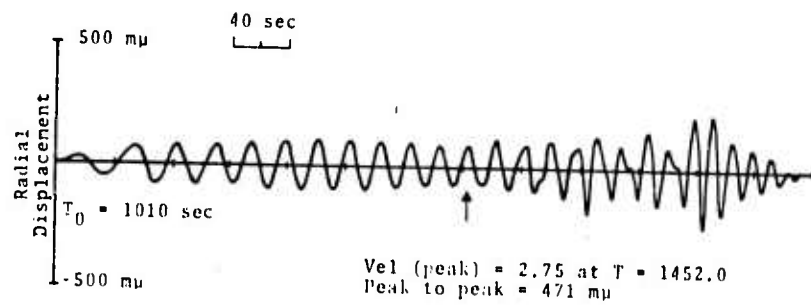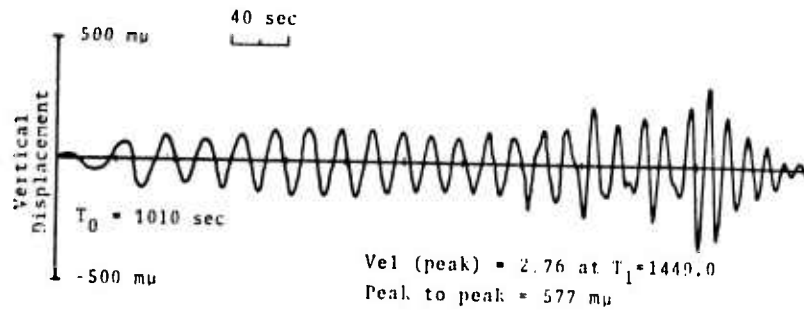
(b) Earth structure NTS granite crust/Helmberger mantle.
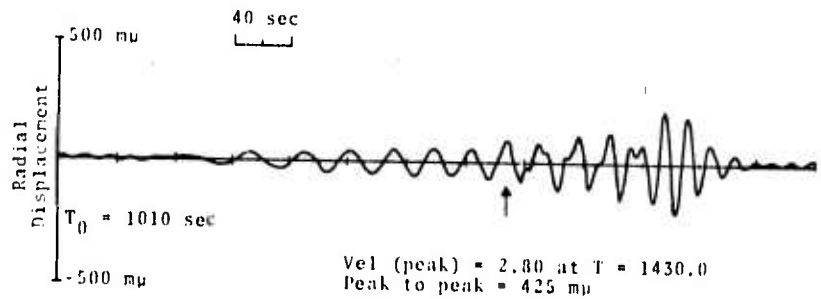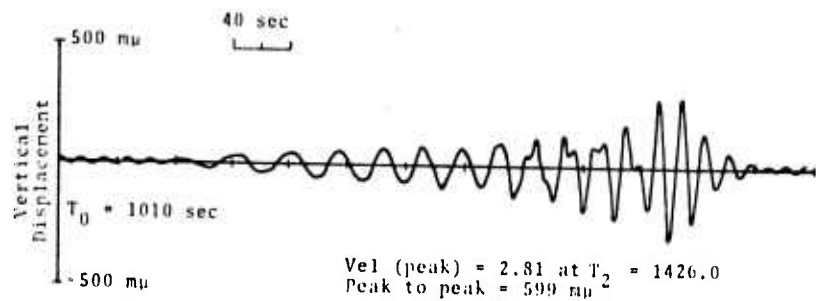
(c) Earth structure Fallon to Ruth/Helmberger mantle.
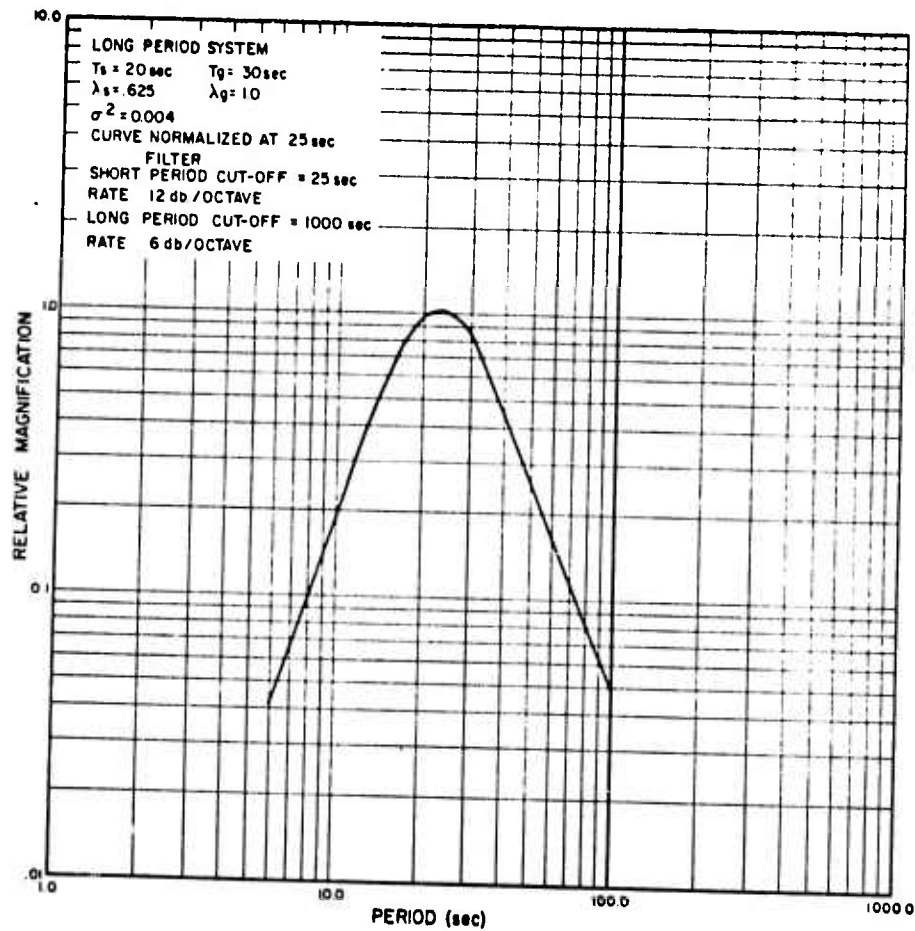
Fig. 3.3--Instrument response of the LRSM Long Period Seismograph (LRSM Shot Report [19]).

The earth structure affects both the arrival time and amplitude of the various frequency components. Surface waves from different events are often compared through a single number, the surface wave magnitude, M_s. The commonly used Gutenberg-Richter formula for M_s is[18]

$$M_s = \log A_H + 1.656 \log\Delta + 1.818 , \qquad (3.1)$$

where A_H is the maximum zero-to-peak amplitude in microns of the horizontal component of the fundamental mode Rayleigh wave having a period of about 20 seconds, and Δ is the epicentral distance in degrees. This formula is to be applied only for $15 < \Delta < 130$.

Several other definitions of M_s are commonly used. In this report we will refer to a modification of (3.1) to deal with maximum amplitudes different from 20 seconds which is,

$$M_s = \log \left(\frac{A_H}{T}\right) + 1.656 \log\Delta + 3.119 . \qquad (3.2)$$

For $T = 20$, (3.2) is identical to (3.1).

The LRSM instrument for which the seismograms of Fig. 3.2 were prepared is normalized to unity at 25 seconds. The instrument effect can be deleted by applying an instrument correction to the calculated M_s values, using the nominal magnification of Fig. 3.3. The instrument corrected M_s values, which represent true ground motion, will be denoted M_s^G.

In Table 3.1 the M_s values for the records of Fig. 3.2 are summarized. From the table we see that the earth structure can have a noticeable effect on M_s, even for these three similar structure models. A more significant variation in M_s results from choice of the phase of maximum amplitude, the Airy phase, for M_s measurements, rather than the

TABLE 3.1

M_s VALUES FOR THE SEISMOGRAMS OF FIGURE 3.3

Structure	Period	$A_H(\mu)$	M_s	M_s^G
CIT 109	20 sec 14 sec	0.125 0.329	3.49 4.07	3.52 4.34
NTS Granite/H.M.	20 sec 14 sec	0.105 0.235	3.42 3.92	3.45 4.19
Fallon to Ruth/H.M.	20 sec 14 sec	0.038 0.210	3.34 3.87	3.37 4.14

amplitude at 20 seconds. Values of M_s from the two are really not comparable.

A sampling of observed M_s values for Piledriver from LRSM data[19] is given in Table 3.2. These values were calculated by using the LRSM observed A/T values for the LQ phase recorded on LPR instruments in Eq. (3.2). The observed M_s values are somewhat greater than the computed values, which is expected since only explosion effects were considered in the calculations leading to Table 3.1. A strong tectonic release component was observed for the Piledriver event[16] and addition of this contribution would raise our M_s values. Further, the source function G-2 has a $\psi(\infty)$ which is 3.9 times greater than the $\psi(\infty)$ for G-1. As will be verified in subsequent sections, use of G-2 will increase all M_s, M_s^G values in Table 3.3 by 0.59.

At present we are limited to laterally homogeneous structure models. Propagation of surface waves through continental-oceanic boundaries or into regions of quite different crustal structure can, of course, result in average velocity-depth profiles quite different from those of Fig. 3.1 and have a significant effect on M_s measurements.

45
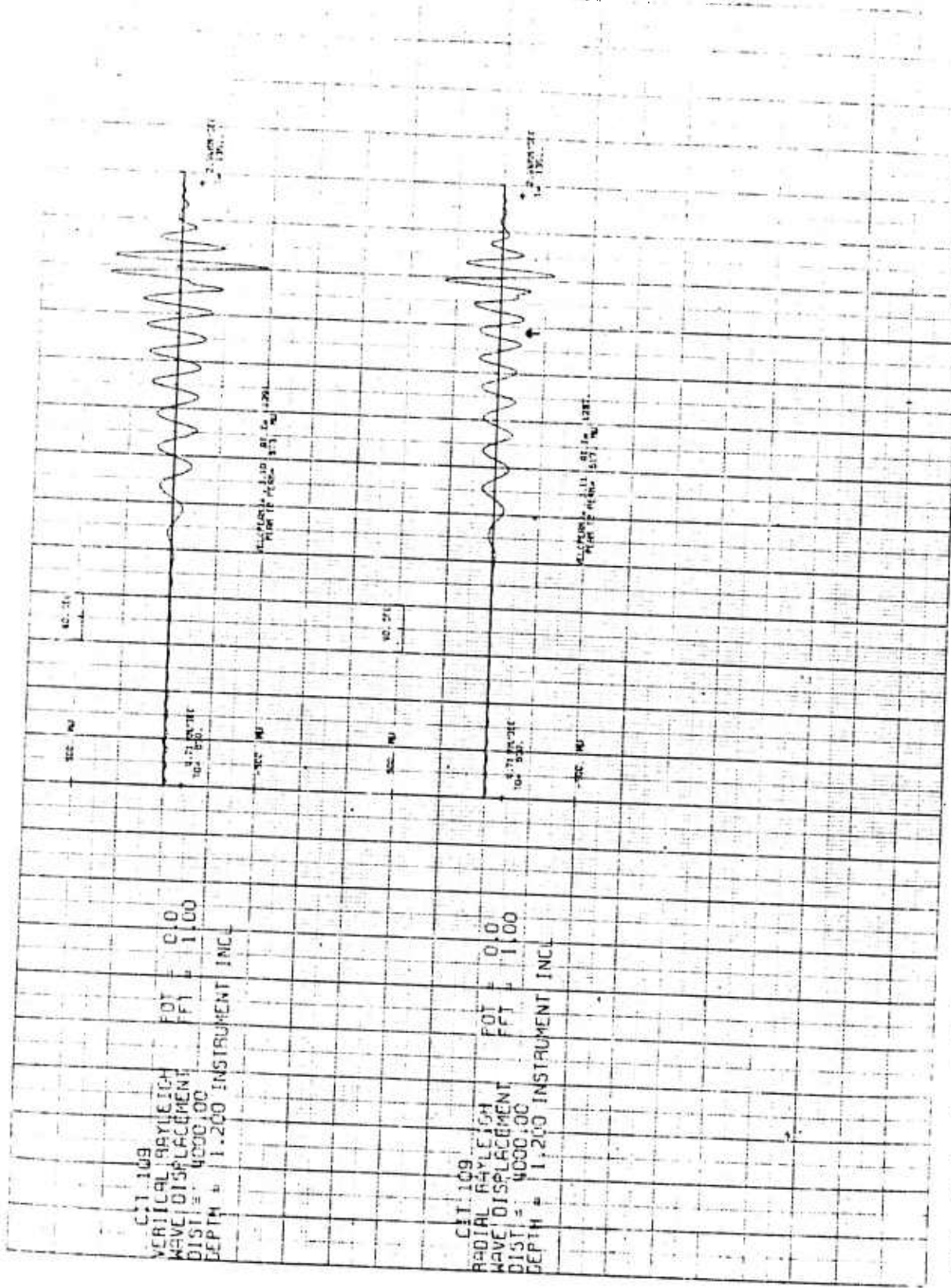
Fig. 3.4--Rayleigh wave synthetic seismograms for an explosion at a depth of 1200 meters in the NTS granite. Yield 61 kt, Source G-1, epicentral distance 4000 km, earth structure CIT 109.

TABLE 3.2

OBSERVED M_s VALUES FOR PILEDRIVER

Station	Distance	Period	A_H/T	M_s	M_s^G
SI-BC	2126	15 sec	0.199	4.54	4.75
AX2AL	2764	23 sec	0.022	3.78	3.79
BE-FL	3286	17 sec	0.057	4.31	4.42
SV3QB	4178	26 sec	0.014	3.86	3.87

3.3.2 Depth of Burial

The Rayleigh wave calculation leading to the seismogram of Fig. 3.2a is repeated at a burial depth of 1200 m. The two seismograms demonstrating depth of burial effects are shown in Fig. 3.4. Comparing Fig. 3.4 to Fig. 3.2a, the shape of the two is seen to be identical, with the only change being a small decrease in amplitude with increasing depth. The corresponding M_s values, which are virtually identical, are compared in Table 3.3.

TABLE 3.3

COMPARISON OF M_s FOR TWO DEPTHS OF BURIAL

Seismograph	Depth	Period	$A_H(\mu)$	M_s	M_s^G
3.2a	463 m	20 sec	0.125	3.49	3.52
		14 sec	0.329	4.07	4.34
3.3	1200 m	20 sec	0.120	3.48	3.51
		14 sec	0.309	4.04	4.31

3.4 RAYLEIGH WAVES FROM SELECTED EVENTS

The teleseismic surface waves from several underground explosions in tuff, sandstone and granite media will now be studied. Since surface waves are dependent on the low frequency behavior of the source, and since the calculated source functions are flat in the low frequency ($f < 0.2$ Hz) portion of the spectrum, the surface wave amplitudes are expected to scale with the steady state value of the RDP, $\psi(\infty)$.

The basic parameters characterizing several representative underground explosion events in the three source media are listed in Table 3.4. The value of $\psi(\infty)$ is calculated for the indicated yield by scaling the SKIPPER value which was calculated for a nominal yield of 0.02 kt. For example, from Table 2.2 the steady state RDP for T-4 is 1.35 m^3.

TABLE 3.4

DESCRIPTION OF SELECTED EXPLOSION EVENTS

Event	Source Medium	Yield	Depth	SKIPPER Source	$\psi(\infty)$ (m^3)
Bilby	Tuff	$\sim$200 kt	700 m	T-4	1.35×10^4
Rio Blanco	Sandstone	3×30 kT	1830 m	S-1	9.0×10^3
Rulison	Sandstone	40 kT	2573 m	S-2	3.6×10^3
Piledriver	Granite	61 kT	463 m	G-1	6.77×10^3
Knickerbocker	Tuff	75 kT	630 m	T-4	5.062×10^3
Greeley	Tuff	825 kT	1214 m	T-4	5.57×10^4
Benham	Tuff	1100 kT	1402 m	T-4	7.43×10^4

Using the scaling rule of Table 2.1, the $\psi(\infty)$ for Bilby is

$$\psi(\infty)_{200} = \frac{235}{0.02} \, \psi(\infty)_{0.02} = 13,500 \text{ m}^3 \ .$$

A sampling of the vertical and horizontal Rayleigh
wave synthetic seismograms for Bilby and Rio Blanco are
given in Figs. 3.5 and 3.6. Similar seismograms were con-
structed for Rulison. The earth structure CIT 109 was used
for these calculations. The comparable seismograms, using
the same earth structure, for the Piledriver event were
previously shown in Fig. 3.1a. Theoretical magnitudes for
these four events are summarized in Table 3.5.

The peak-to-peak amplitude, $2A_H$, from Table 3.5 is
plotted vs $\psi(\infty)$ in Fig. 3.7. The line of unit slope
through each data set is also shown on the figure. Recall
from Section 3.3.2 that the effect of increasing depth of
burial is a small decrease in Rayleigh wave amplitude.
Correlating the data of Fig. 3.7 with the depths for the
events from Table 3.4, we see that the deviation from the
line of unit slope is consistent with expected depth of
burial effects.

Since Rayleigh wave amplitudes scale directly with
$\psi(\infty)$, keeping depth of burial fixed, we can obtain M_s
estimates for the tuff events Knickerbocker, Greeley and
Benham by scaling the data of Tables 3.3 and 3.5. The re-
sults are summarized in Table 3.6.
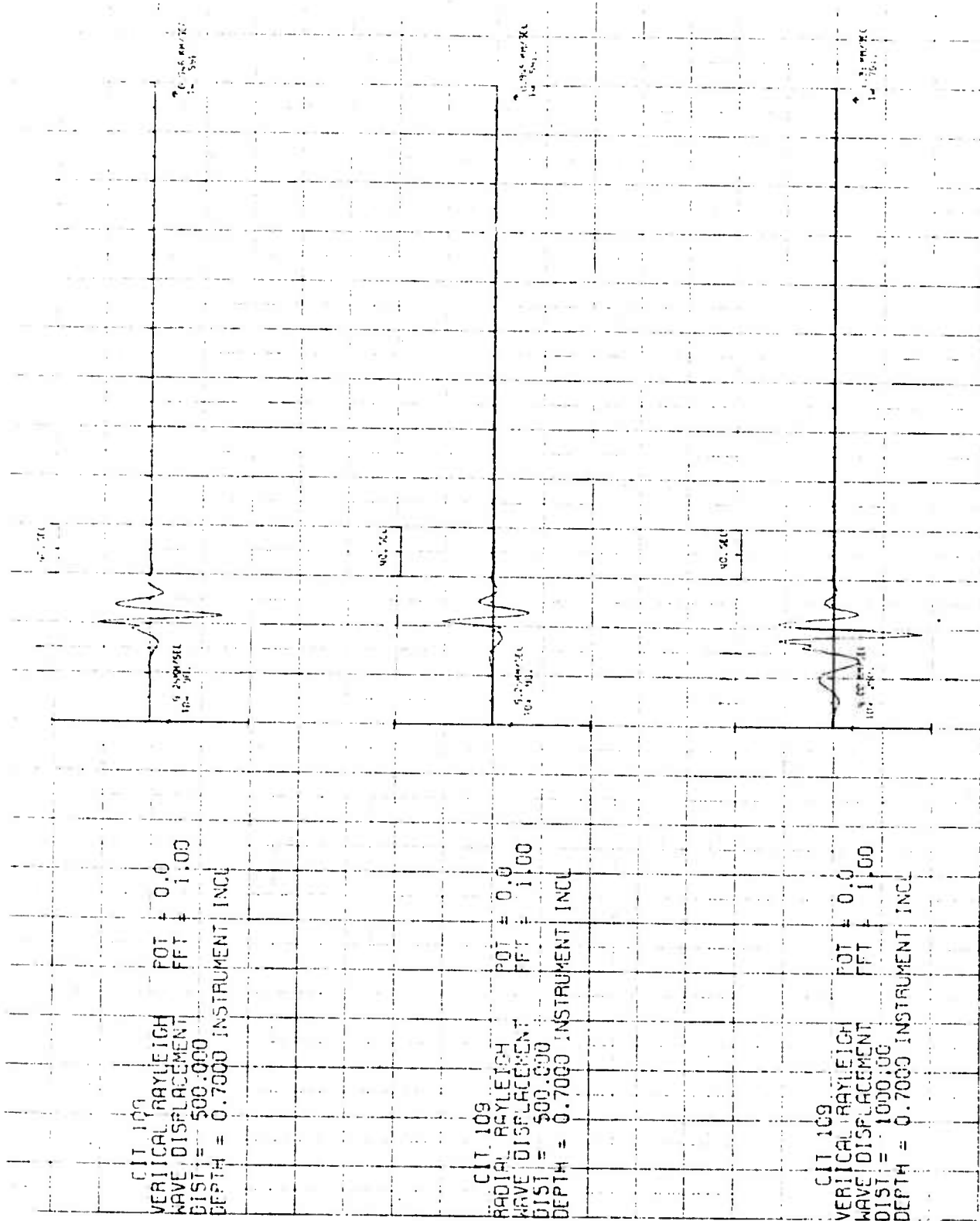
Fig. 3.5--Synthetic Rayleigh wave seismograms for the Bilby event. Yield Source T-4, DOB 700 meters, earth structure model CIT 109.

Fig. 3.5 (Cont.)

Fig. 3.5 (Cont.)

CIT 109
VERTICAL RAYLEIGH   POT = 0
WAVE DISPLACEMENT   FFT = 1
DIST = 3000.00
DEPTH = 0.7000 INSTRUMENT INCL

CIT 109
RADIAL RAYLEIGH   POT = 0.0
WAVE DISPLACEMENT   FFT = 1.00
DIST = 3000.00
DEPTH = 0.7000 INSTRUMENT INCL

CIT 109
VERTICAL RAYLEIGH   POT = 0.0
WAVE DISPLACEMENT   FFT = 1.00
DIST = 3000.00
DEPTH = 0.7000 INSTRUMENT INCL

52

Fig. 3.5 (Cont.)

CIT 109
RADIAL RAYLEIGH
WAVE DISPLACEMENT
DIST = 4000.00
DEPTH = 0.7000 INSTRUMENT INCL

POT = 0.0
FFT = 1.00

Fig. 3.6--Synthetic Rayleigh wave seismograms for the Rio Blanco event. Yield 3×30 kt, Source S-1, average DOB 1830 meters, earth structure model CIT 109.

Fig. 5.6 (Cont.)

Fig. 3.6 (Cont.)

Fig. 3.6 (Cont.)
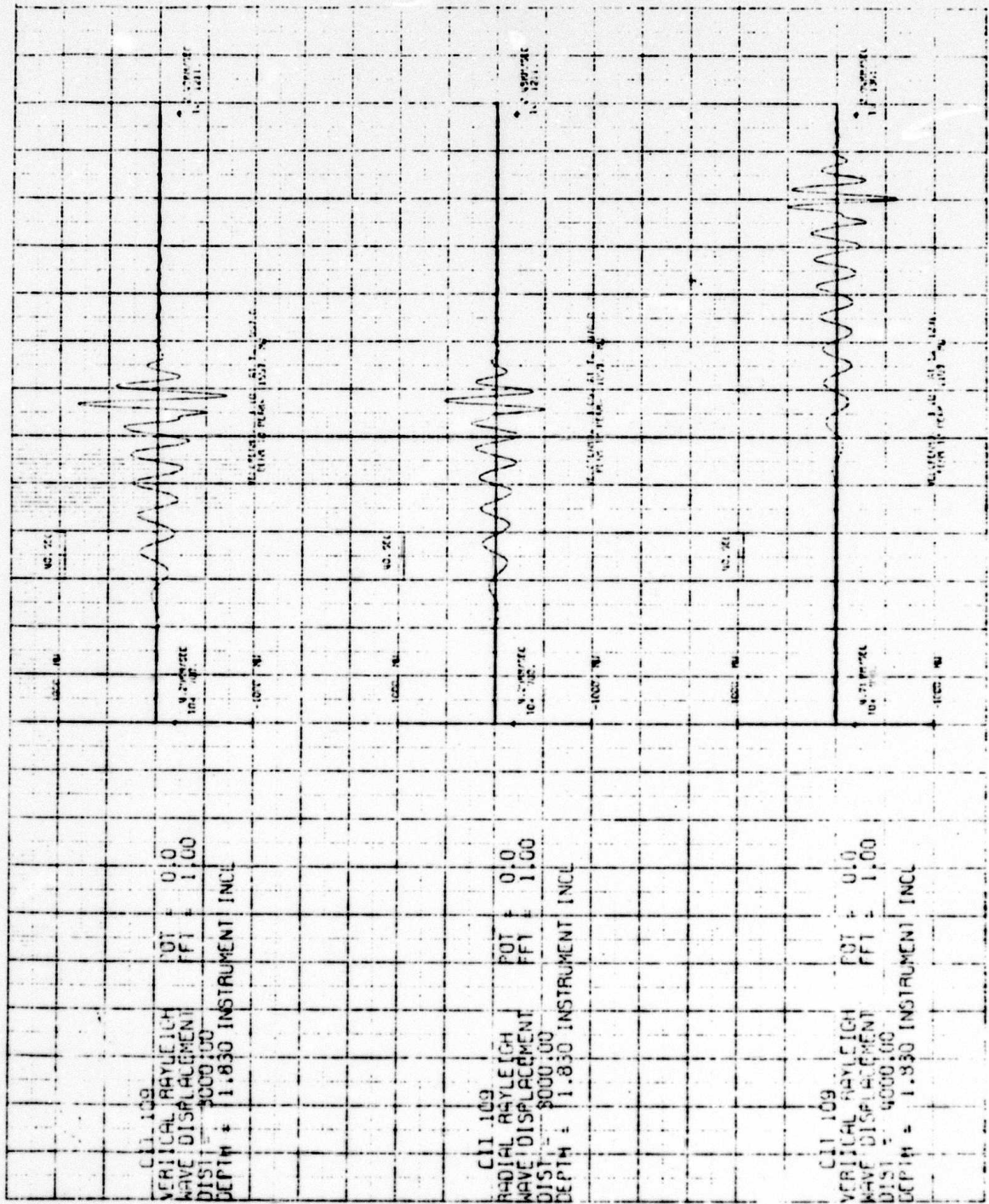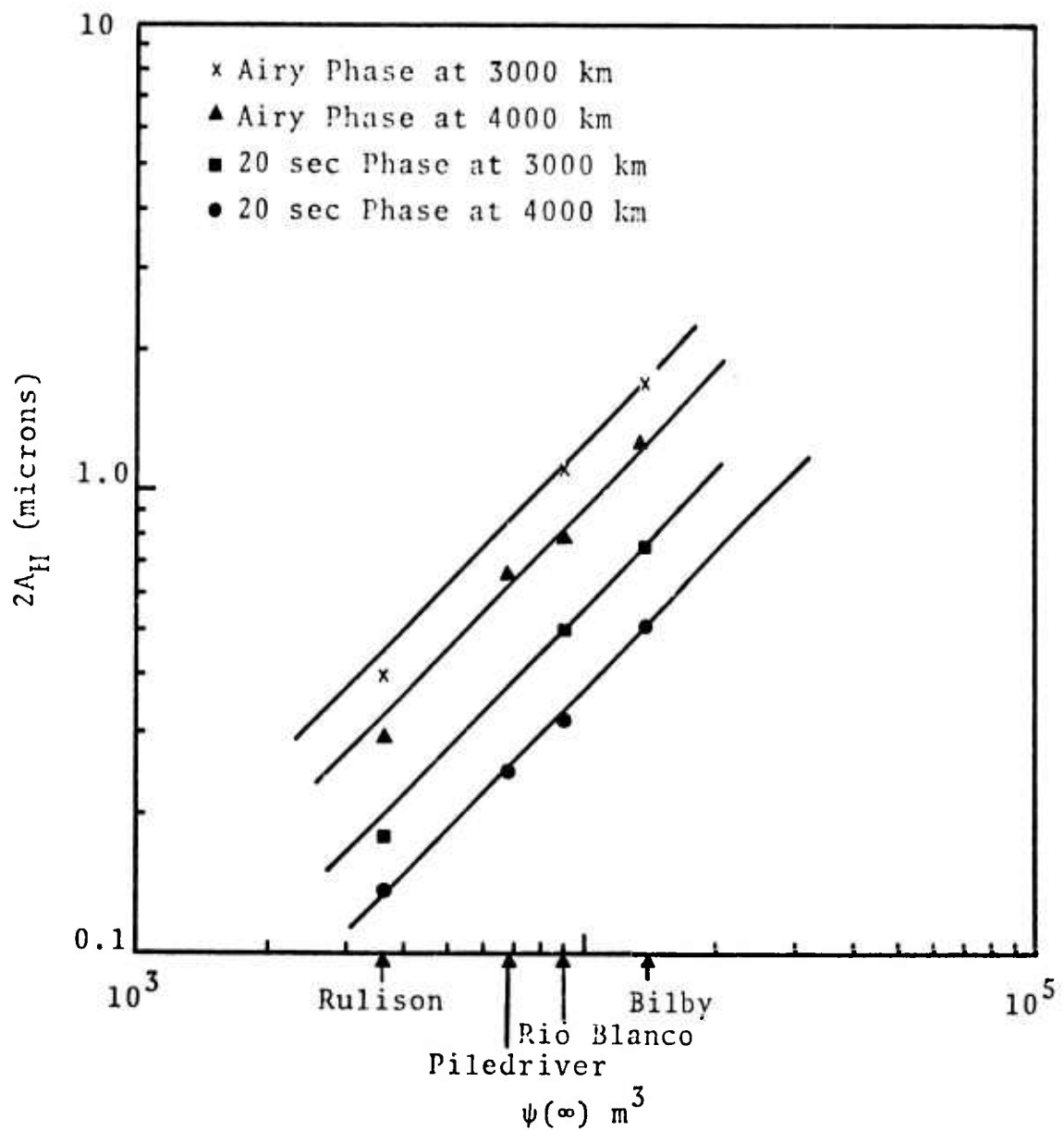
Fig. 3.7--Peak to peak amplitude of the radial Rayleigh wave, $2A_H$, for selected events versus the steady state value of RDP, $\psi(\infty)$. Lines of unit slope are shown with each data set.

TABLE 3.5

PREDICTED MAGNITUDES FOR SELECTED EVENTS

Event	Distance (km)	Period (sec)	$2A_{II}(\mu)$	M_s	M_s^G
Bilby	3000	20	0.72	3.75	3.78
	3000	14	1.7	4.27	4.54
	4000	20	0.49	3.8	3.82
	4000	14	1.24	4.34	4.61
Rio Blanco	3000	20	0.50	3.59	3.62
	3000	14	1.10	4.08	4.35
	4000	20	0.32	3.60	3.63
	4000	14	0.78	4.14	4.41
Rulison	3000	20	0.18	3.14	3.17
	3000	14	0.40	3.64	3.91
	4000	20	0.137	3.23	3.26
	4000	14	0.29	3.71	3.98
Piledriver	4000	20	0.25	3.49	3.52
	4000	14	0.66	4.07	4.34

TABLE 3.6

PREDICTED SURFACE WAVE RESULTS FOR KNICKERBOCKER, GREELEY
AND BENHAM AT 4000 KM

Event	Period (sec)	$A_{II}(\mu)$	M_s	M_s^G
Knickerbocker	20	0.093	3.36	3.39
	14	0.233	3.92	4.19
Greeley	20	0.987	4.39	4.42
	14	2.54	4.96	5.23
Benham	20	1.32	4.52	4.55
	14	3.39	5.08	5.35

3.5   COMPARISON OF OBSERVED AND COMPUTED M_s

Treating each event as a spherically symmetric explosion via the SKIPPER calculation, theoretical values for M_s have been computed for several representative events. A good comparison of these results with observed values requires further effort to collect observed data along with information on exactly how those data were reduced. However, some M_s data are on hand and we shall present the comparison, recognizing the possibility that inconsistent data reduction exists over the set.

A bar graph comparison of observed and computed M_s is presented in Fig. 3.8. The observed value for Benham is from the WWSSN reports, that for Rulison, Knickerbocker, Greeley and Bilby from Harkrider (private communication) and that for Piledriver from Table 3.2. Since different methods may have been used in computing M_s, the observed values are probably not consistent. The lower (left) points on the computed value bars correspond to M_s based on the 20-second phase.

Examining Fig. 3.8, we see that our M_s estimates are consistently low compared to the observations. This is not surprising since the effect of the anomalous shear wave component (tectonic release), present to some degree in every event, is to raise M_s. The addition of a tectonic release quadrupole source to the explosion source will then increase our computed M_s. The computational capability to accomplish this task is available to us, but has not yet been applied for surface waves. Also, from Section II, note that the source function T-4, which has been used for our tuff calculations, has the smallest $\psi(\infty)$ of the tuff source functions presented. Selection of one of the greater source functions, such as T-3, would scale the M_s for the tuff events accordingly.
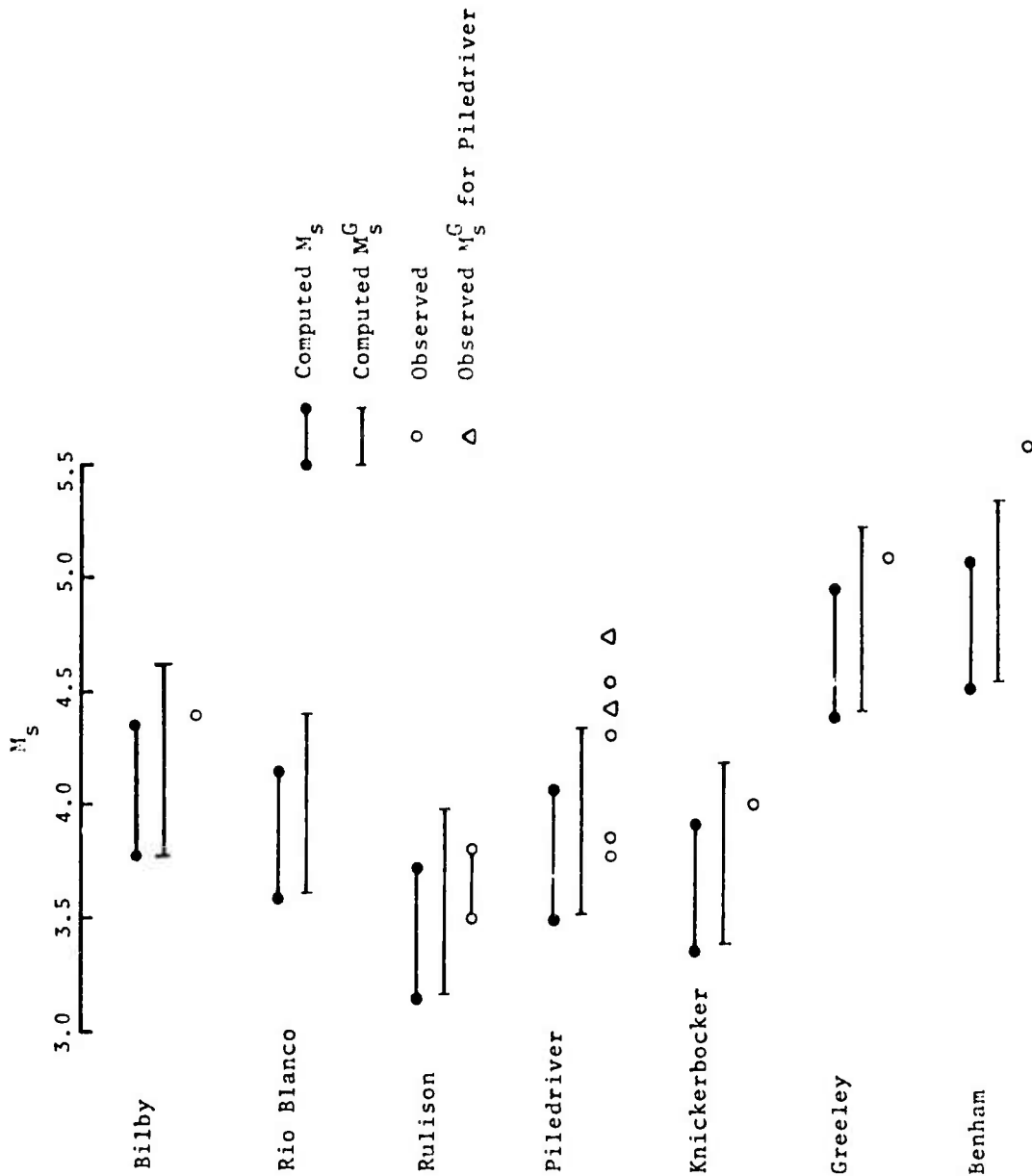
Fig. 3.8--Comparison of observed and computed M_s values for selected events.

For example, source T-3 results in a new M_s for the tuff events which is 0.2 units higher than those shown in Fig. 3.8. A similar upward scaling of M_s by changing source functions for the Piledriver calculation was mentioned in Section 3.3.1.

In summary, selection of a larger explosion source function, inclusion of tectonic release and modifying the assumed earth structure are all effective ways to increase the predicted values of M_s. Before any of these are invoked, it is important that an M_s data set be obtained that is self-consistent.

IV. TELESEISMIC BODY WAVES FROM UNDERGROUND NUCLEAR EXPLOSIONS

4.1   INTRODUCTION

The teleseismic signature of body waves excited by an underground nuclear explosion is affected by the various parameters which characterize the source, the receiver, and the earth structure through which the explosion generated stress wave is propagated. A computational model which embodies the main features of these parameters is now available.

Synthetic seismograms which provide accurate predictions of m_b and the basic shape of the first few seconds of the ground motion record at selected teleseismic distances are now routinely generated by computer codes operational at S^3. The application of these codes to study the dependence of m_b (and the time domain character of body wave arrivals) on the important parameters affecting teleseismic ground motion is the subject of this section.

4.2   THE BODY WAVE CODES

The program for computing teleseismic body waves is composed of three subprograms called SOURCE, TFRFNC and TIMSER. The role these subprograms play in the body wave program is the subject of the following discussion.

Description of the Source

The explosion source (which may include tectonic stress relaxation effects) is described by the displacement spectra (P, SH and SV) at a specified radial distance r (in the elastic regime), over a range of azimuthal angles θ and over a range of take-off angles ϕ. Equivalently, the source may be defined by the coefficients of the spherical wave function expansion of the outgoing waves. For a spherically symmetric explosion plus tectonic release, only the monopole and quadrupole compoents are present in the expansion. [17]

63

The reduced displacement potential (RDP) transform, $\hat{\psi}(\omega)$, is obtained from an appropriate SKIPPER calculation as discussed in Section II. The P wave displacement spectrum at a radius r due to a spherically symmetric explosion may be shown to be related to the RDP transform by,[1]

$$\hat{U}_r^{P_e} = \frac{(1 + k_p r)}{r^2} e^{-ik_p r}\psi(\omega) \ , \tag{4.1}$$

$$\hat{U}_\theta^{P_e} = \hat{U}_\phi^{P_e} = 0,$$

where the superscript P_e denotes the P wave from the explosion, the subscripts r, θ, ϕ are spherical coordinates, and $k_p \equiv \omega/v_p$ is the wave number for compressional waves. For a spherically symmetric explosion, only P waves are released. The program SOURCE reads $\hat{\psi}(\omega)$ and calculates the displacement spectrum $\hat{U}_r^{P_e}(r,\omega)$ due to the explosion.

The theory of the dynamic relaxation of tectonic stress due to the creation of a cavity and surrounding zone of fractured material in a prestressed geologic formation is given by Archambeau.[17] In this theory the tectonic component of the source is specified in terms of a quadrupole point source. Such an equivalent point source representation has been shown by Archambeau and others (e.g., Refs. [13-17]) to explain the anomalous Rayleigh wave radiation pattern and Love wave radiation from nuclear explosions. Calculation of the displacement spectra at a radius r from such a source is performed by SOURCE yielding the spectra $\hat{U}_i^{P_t}$, $\hat{U}_i^{S_t}$, where $i = r$, θ, ϕ and the superscripts P_t and S_t indicate the P and S waves due to the tectonic release.

Near-Source Free Surface Reflection

Having specified the equivalent elastic source, in a suitable format, the remainder of the calculation is carried

out in the linear regime. Therefore, individual frequency components may be separately propagated through the earth model and superposed at the receiver.

The program SOURCE also computes the reflected and converted (S to P and P to S) waves at the free surface for take-off angles of interest. Therefore, if $\hat{U}^P e$ and $\hat{U}^P t$ (r, ω) are the P wave displacement spectra due to the explosion and tectonic release which emanate from the source region at a take-off angle θ_p and azimuth ϕ_p, the program SOURCE will compute the additional displacements $\hat{U}^{pP} e$, $\hat{U}^{pP} t$, from the free surface reflections which also leave the source region along this ray (Fig. 4.1). An analogous calculation is carried out for S waves.

For computation of the near-source free surface reflection, SOURCE considers the source-to-surface material to be homogeneous and characterized by a separately input attenuation parameter Q and wave speeds v_p^{ss} and v_s^{ss}. The latter velocities are commonly selected to be the source region values from the SKIPPER calculation.

Earth Structure

As just described, SOURCE calculates the displacement spectrum for each of the various phases emanating from the source region at selected azimuths and take-off angles. In propagating these displacements to teleseismic distances, the effect of the earth's structure enters via multiplication by the complex transfer function, $A_p(\omega)$, which includes the radial spreading, attenuation and dispersion due to the path from source to receiver. While several methods for obtaining such transfer functions are available, the results of this report were obtained using the program TFRFNC.
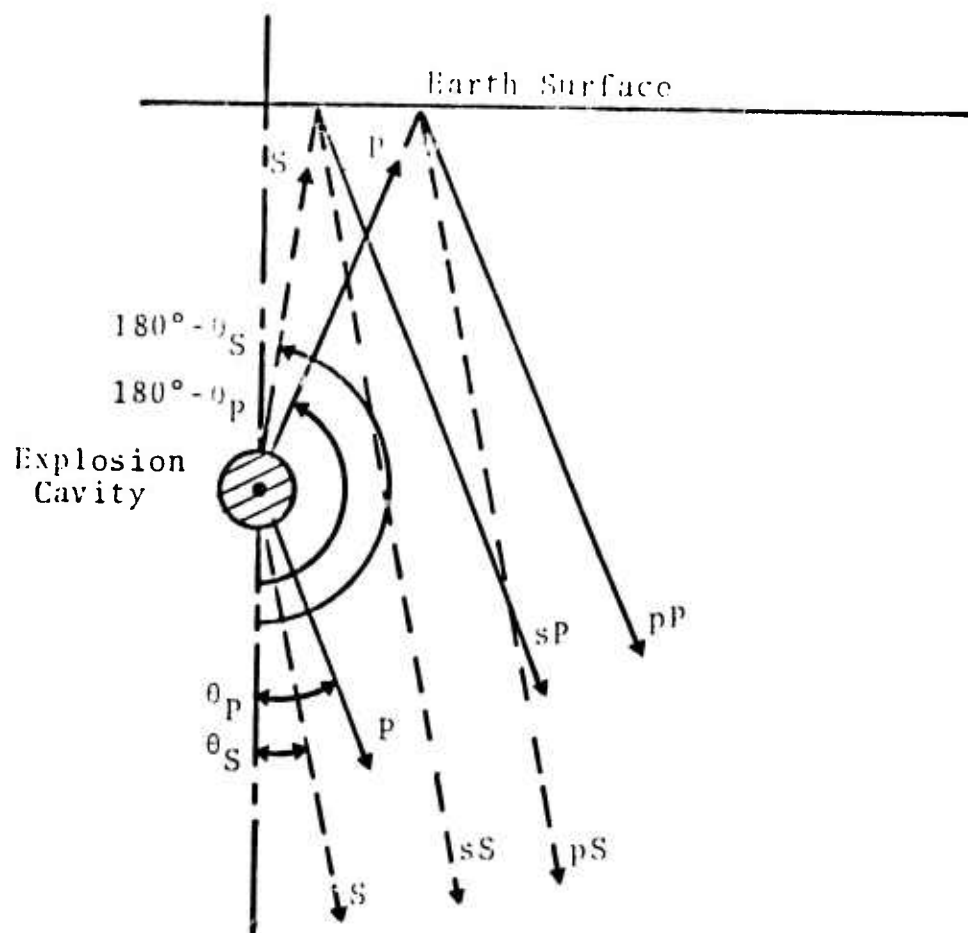
Fig. 4.1--Direct, reflected, and converted body waves leaving
the source region.

This program uses ray theory[20] to calculate the transfer functions for ray paths through a radially strati- fied earth model over a range of take-off angles. In addition to geometric spreading effects, the wave amplitudes are attenuated as

$$\tilde{U} = U e^{-\omega T/(2\,Q_p)},$$ (4.2)

where Q_p is the dissipation constant for the ray path corresponding to the take-off angle θ_p. A necessary conse- quence of the medium absorption (4.2) is dispersion. The relation between the two is discussed by Futterman[21] and Strick.[22] Using the formulation of Strick, dispersion is included by multiplying $\tilde{U}$ of (4.2) by

$$\exp\left[\frac{i\omega T}{\pi Q_p}\,\ell n\,(\omega_h/\omega)\right],$$ (4.3)

where ω_h is selected as a high frequency cutoff parameter and T is the travel time associated with waves of frequency ω_h. Thus, if A_p is the multiplication factor due to radial spreading, the total transfer function for the ray of take- off angle θ_p is

$$A_p(\omega) = \hat{A}_p\,\exp\left\{\frac{-\omega T}{2Q_p}\left[1 - \frac{2i}{\Pi}\,\ell n\,(\omega_h/\omega)\right]\right\}$$ (4.4)

Ground Motion at the Receiver

Multiplying by the transfer function $A_p(\omega)$ in SOURCE, the spectra of the various direct, reflected and converted displacement waves due to the explosion (and, if required, tectonic release) at points of interest in the teleseismic field are obtained. By applying suitable correction factors (see Appendix 2 of Ref. [1]), these may be converted into

the spectra of vertical, radial (from ground zero) and tangential ground motion at the receiver. True ground motion for each of the phases results from a Fourier synthesis into the time domain.

The program TIMSER applies a fast Fourier transform routine to the spectra of the individual phases arriving at the receiver. If the seismometer transfer function is included prior to the Fourier transformation, the ground motion record appropriate to a given instrument is obtained.

The seismogram for each mantle arrival is obtained by superposing the time records for the phases associated with a particular take-off angle (and ray path). Since several take-off angles (and mantle arrivals) may be associated with a given point in the teleseismic field, rather complex synthetic seismograms are obtained.

4.3 INVESTIGATION OF THE PARAMETERS AFFECTING m_b

4.3.1 Illustrative Calculations

Before proceeding with a detailed examination of the various parameters affecting teleseismic ground motion records, let us describe a few typical calculations.

Source Effects

Figure 4.2 shows a typical equivalent source representation, this one appropriate to the Handley event which was 1000 kt detonated at a depth of 1.2 km in tuff. The SKIPPER calculation for this event is denoted T-4 and was scaled to the Handley yield using cube root scaling (Table 2.1). The total displacement pulse and spectrum are shown as well as the same quantities including only far field terms (terms decreasing as r^{-1} in Eq. (4.11)). Only far field spectra and wave forms are important for teleseismic body

68
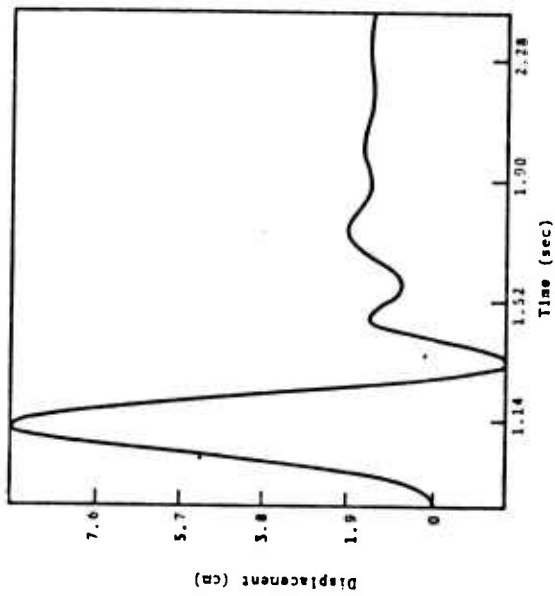
(a) Near plus far field displacement signal from explosion model T-4 (at radius R = 2.28 km).
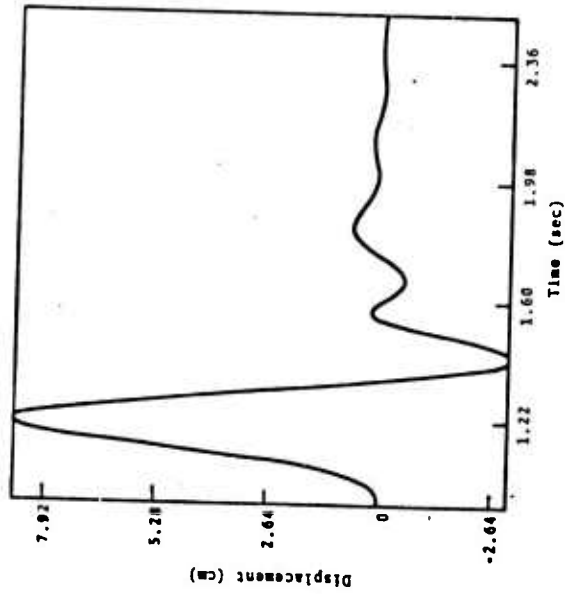
(b) Far field displacement signal from explosion model T-4 (at radius R = 2.28 km).
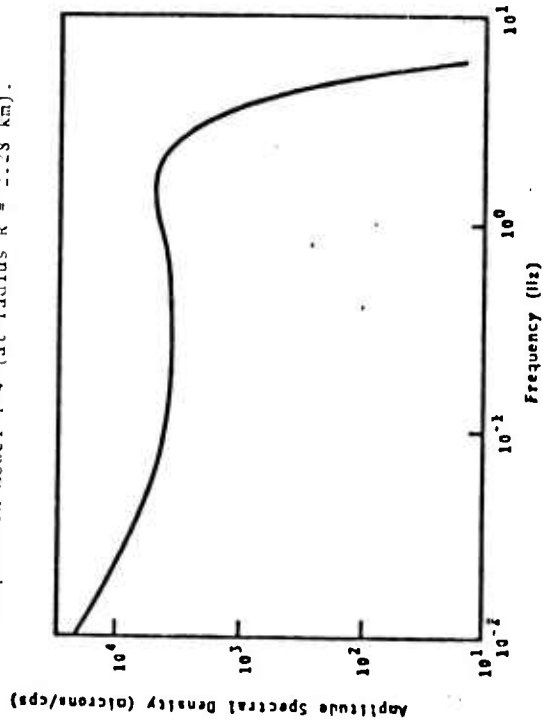
(c) Amplitude spectrum of near and far field radial displacement at a distance of 7.5 km.
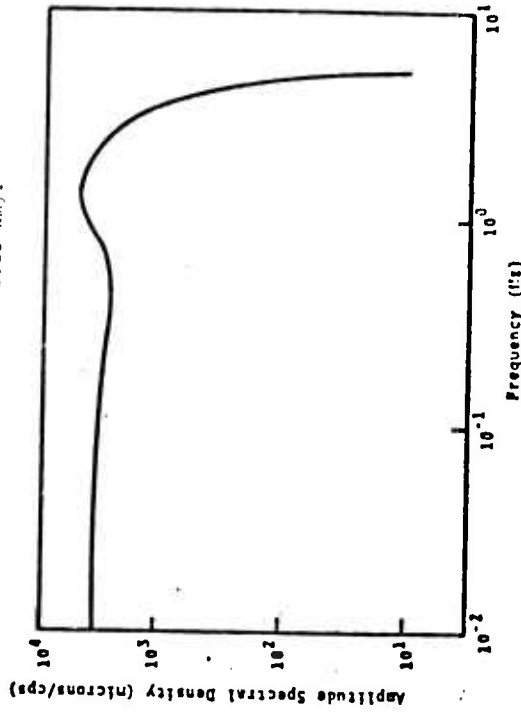
(d) Amplitude spectrum of far field radial displacement at a distance of 7.5 km.

Fig. 4.2--Theoretical signal and spectra from the explosion source model T-4 (tuff).

69

wave phases. Figure 4.3 shows the theoretical far field spectrum and elastic wave form predicted on the basis of a different tuff material model which is denoted T-1. These two source material models, T-4 and T-1, are representative of the variations of material properties for tuff.

The radiated wave form and signal spectrum due to tectonic release depend on the effective size of the prestressed region around the induced zone of failure. This region is characterized by an effective radius R_s. This radius can be taken to be very large, effectively infinite, or finite and on the order of, say, ten times the shatter zone dimension. These two choices result in different radiated seismic waves as illustrated in Fig. 4.4, which also shows how this difference is reflected in the amplitude spectrum of the pulse. From the figure we see that a finite R_s, reflecting a concentration of the initial prestress field or strong spatial variation, results in a peaked far field spectrum and a distinctive pulse shape. On the other hand, for R_s infinite the far field spectrum is flat and the signal pulse non-oscillatory. It is difficult to assess which of these conditions is most common or likely and we leave the issue with the comment that the choice of R_s has a nearly undetectable effect on the synthetic seismograms for short period P waves (the instrument filters out most of the difference and the rest is obscured by simultaneously arriving phases).

Teleseismic Spectra

Multiplying the source spectra (e.g., Fig. 4.3a) by the transfer function characterizing the earth, the source field is propagated to a teleseismic distance. In Fig. 4.5 the spectra due to the Handley explosion is shown at a distance of 4066 km. The earth model used is denoted CIT 109 Low Q (see Section 4.3.2). Both the direct P wave and

70
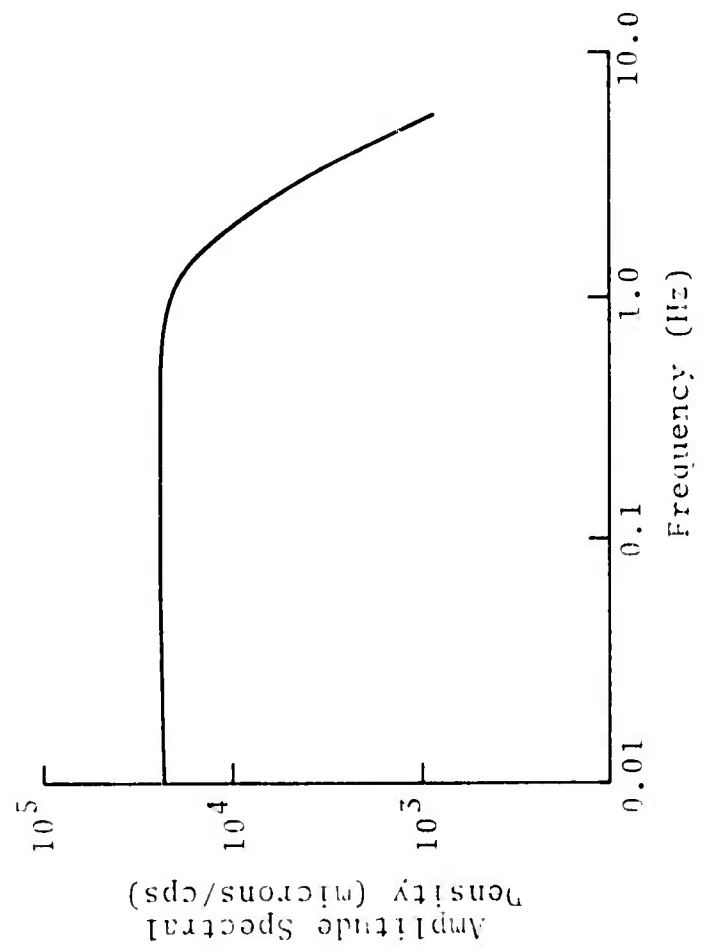
(a) Amplitude spectrum of far field radial displacement at a distance of 7.5 km.
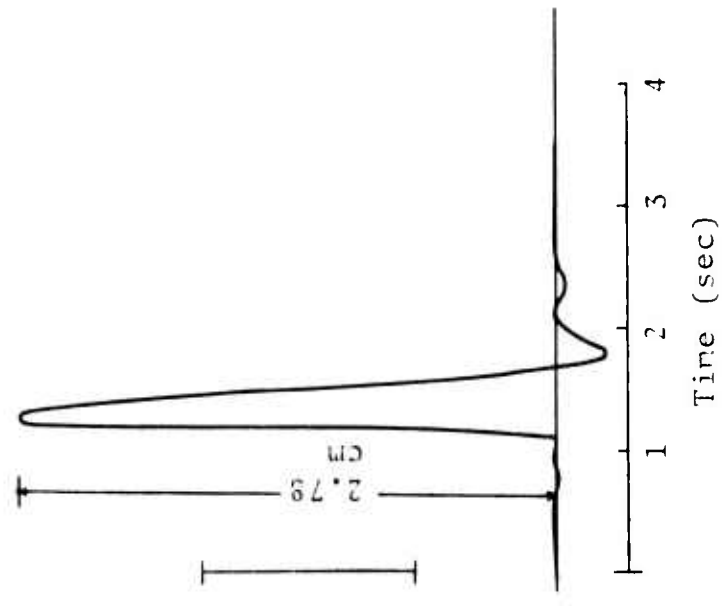
(b) Far field displacement signal from explosion model T-1 (at radius R = 2.28 km).

Fig. 4.5- Theoretical signal and spectra from the explosion source model T-1 (tuff).

71
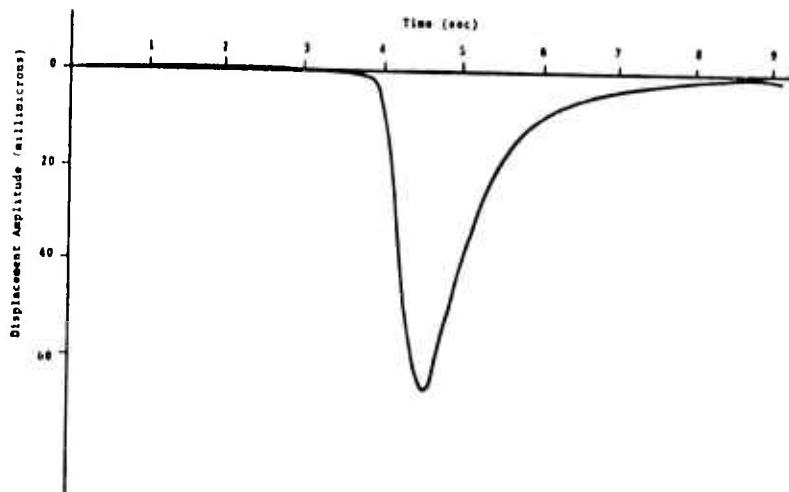
(a) Wave form for tectonic release with R_s infinite.
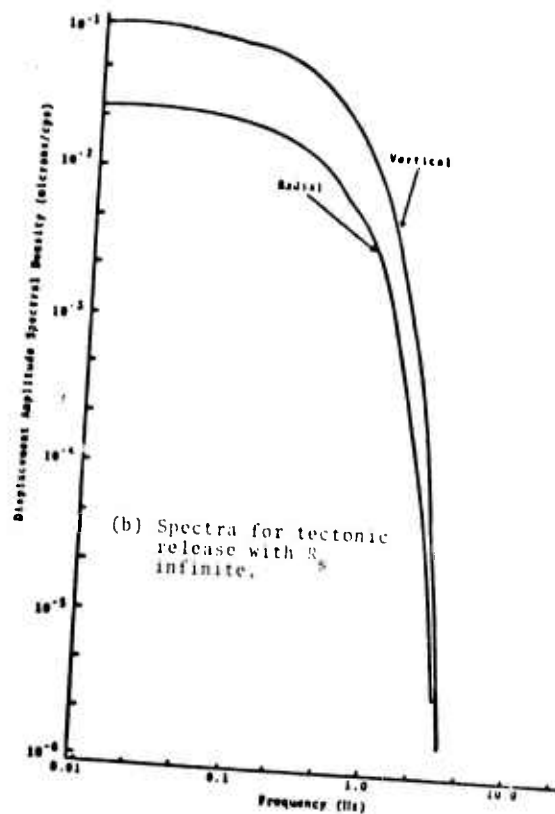
(b) Spectra for tectonic release with R_s infinite.
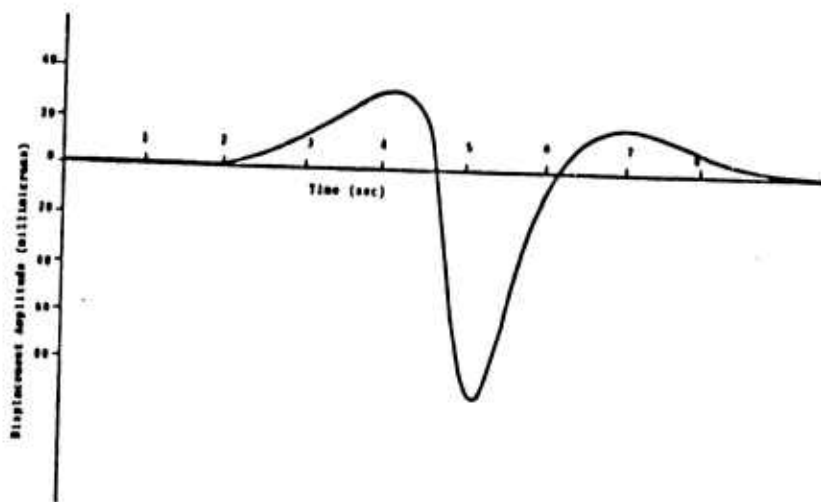
(c) Wave form for tectonic release with R_s finite.
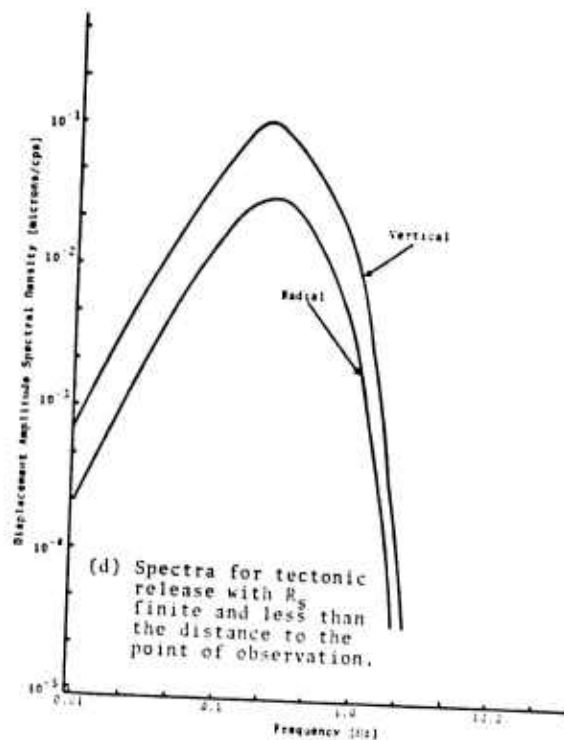
(d) Spectra for tectonic release with R_s finite and less than the distance to the point of observation.

Fig. 4.4--Comparison of S (or P) wave forms and spectra from tectonic release with R_s (relaxation zone radius) finite or infinite. The waves represent true ground displacement with the static offset removed. The source dimension is approximately 2 km with a prestress (shear) of 65 bars. The scales are appropriate for a distance of about 4,000 km with the earth structure and Q accounted for.
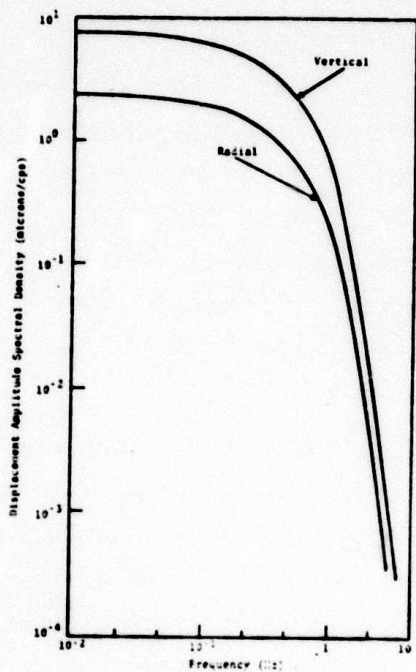
(a) Direct P wave from the explosion.
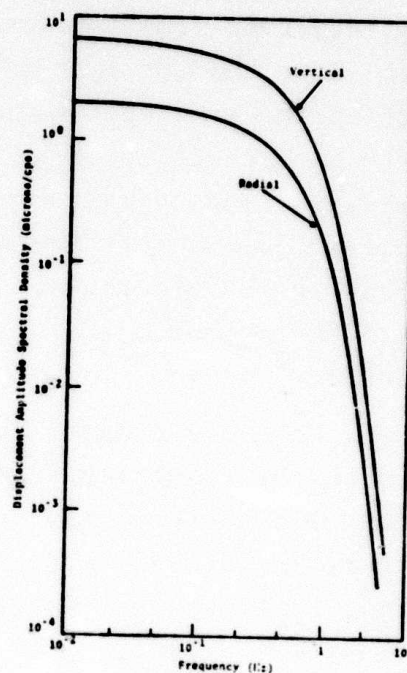
(b) Reflected P wave from the explosion.
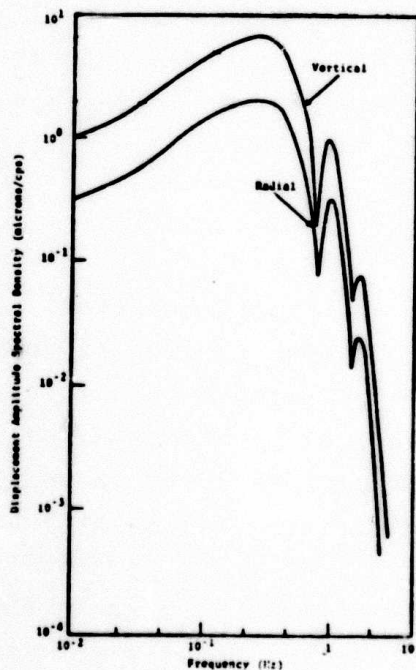
(c) Sum of direct and reflected P waves due to the explosion.
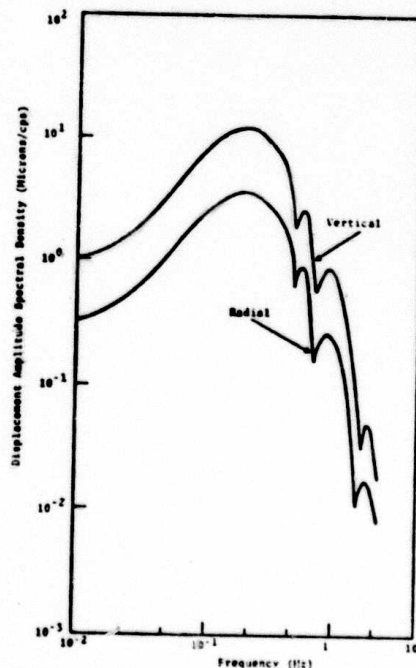
(d) Sum of direct, reflected and converted phases due to all sources (explosion & tectonic release).

Fig. 4.5--Theoretical spectra of explosion generated compressional arrivals from the Handley event at a distance of 4066 km and azimuth of 30°. CIT 109 Low Q model, explosion model T-1, source depth 1.2 km.

pP reflected from the free surface are included. Figure 4.5c shows the spectrum of P and pP combined. The spectral peaking and scalloped nature of the high frequency portion of the composite spectrum result from interference between the direct and reflected waves. In Fig. 4.5d the total spectrum due to both the explosion and tectonic components of the source are shown. This spectrum is somewhat more peaked and complex than Fig. 4.5c due to the tectonic release effects.

Figure 4.6 shows the individual spectra for the body wave phases resulting from tectonic release (with R_s finite), along with the complete spectrum of the composite signal from both explosive and tectonic source components (same as Fig. 4.5d). In this case the largest effect is due to the converted S to P wave, since tectonic release is primarily a source of shear wave energy. The sP_T phase can be as large or larger than the direct P wave from the explosion itself, depending on the stress field orientation and magnitude as well as on the size of the shatter zone created by the shock wave.

Seismograph Modulation

The spectra of Figs. 4.5 and 4.6 relate to actual ground displacement spectra at a point on the free surface of the earth. In order to obtain a meaningful comparison with observations, this signal must be modulated by the transfer function of the detector. Since we are interested in comparing predictions of the teleseismic field to LRSM station recordings, the transfer functions for the short period seismometers employed at these stations will be used in this report. Figure 4.7 shows the amplitude and phase response of the LRSM SP instrument. The gain has been normalized to unity at 1 Hz. Multiplying the spectra of Figs. 4.5 and 4.6 by this transfer function and performing an inverse Fourier
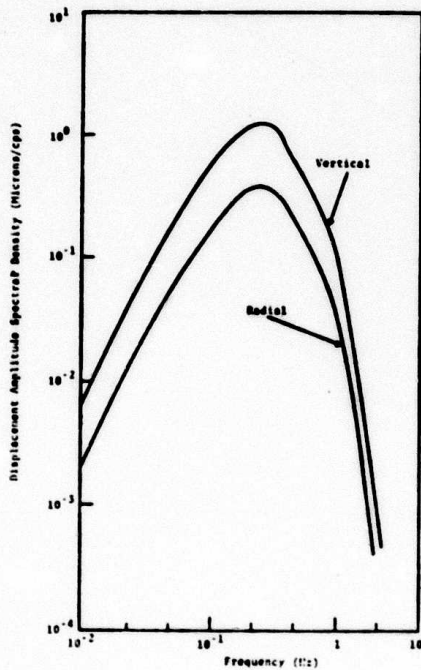
(a) Direct P wave from tectonic release.
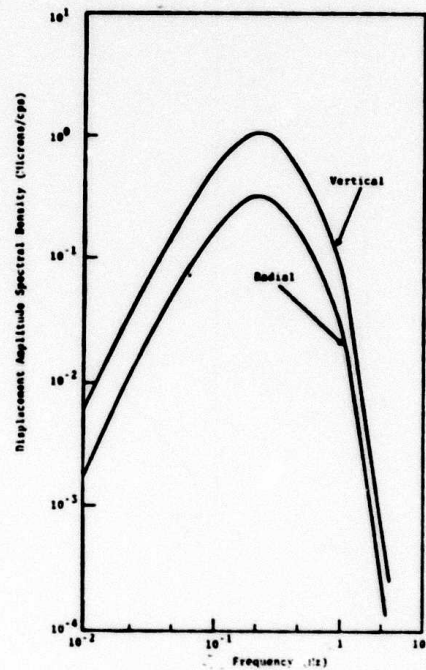
(b) Reflected P wave from tectonic release.
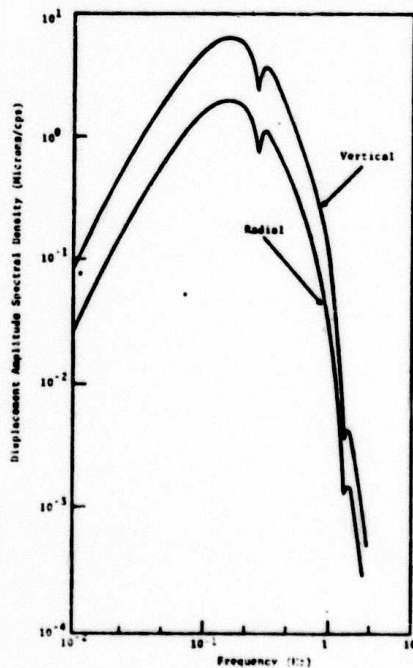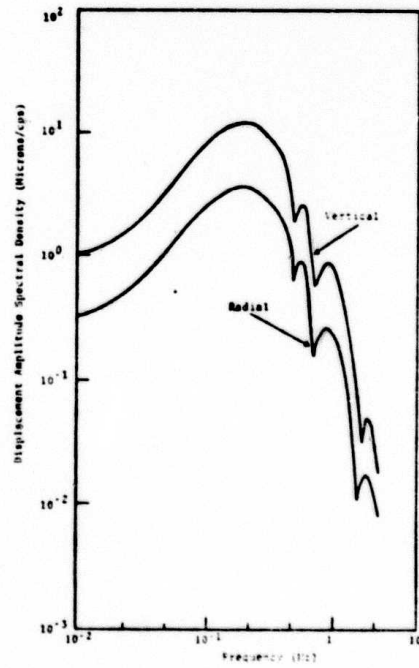
(c) Converted S to P wave from tectonic release.

(d) Sum of direct, reflected and converted phases due to all sources (explosion & tectonic release).

Fig. 4.6--Theoretical spectra of tectonically generated compressional arrivals from the Handley event at a distance of 4966 km. CIT 109 Low Q model, explosion model T-1, source depth 1.2 km.

75
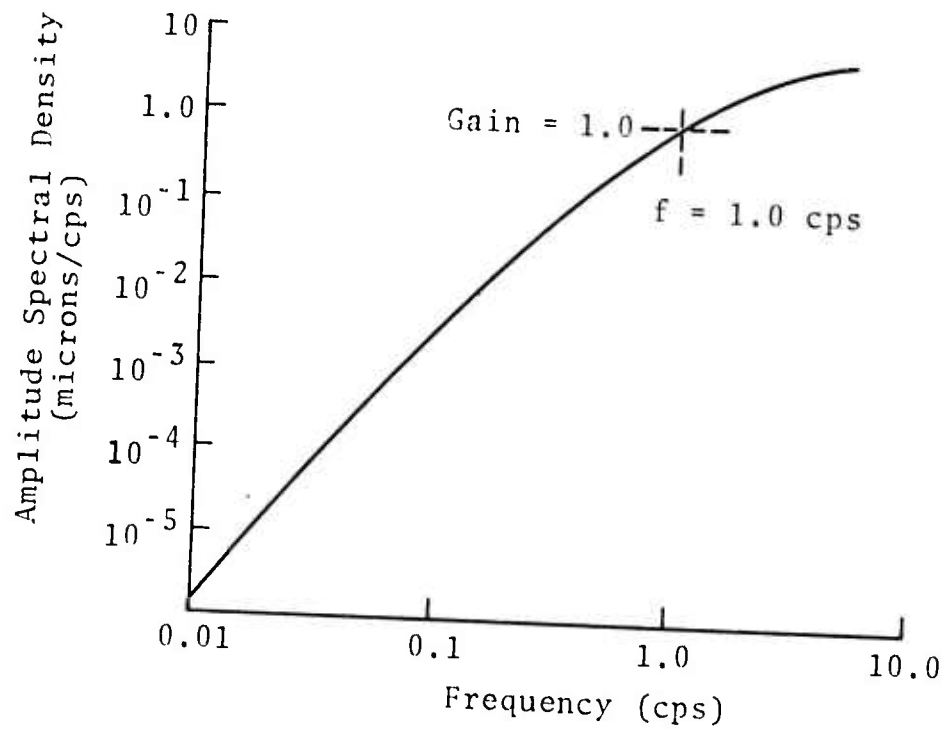
(a) Seismometer amplitude response.
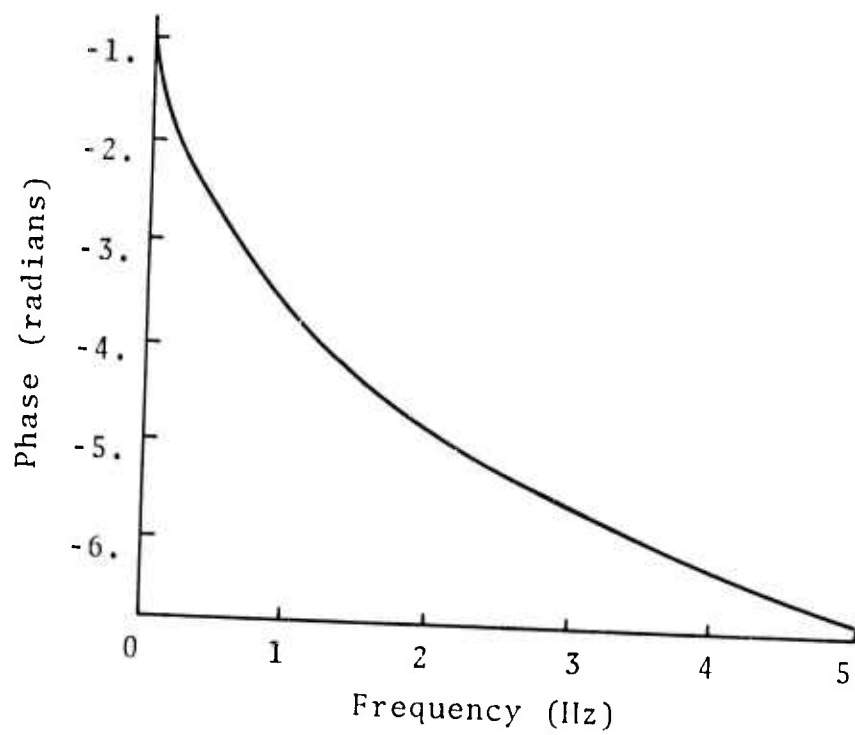
(b) Seismometer phase response.

Fig. 4.7--Transfer function for the short period LRSM seis-
mometer.

transformation, the time domain synthetic signal pulses are
obtained.

Figure 4.8 shows individual teleseismic compressional
pulses with those on the left corresponding to true ground
motion and those on the right the corresponding phases as
recorded on the LRSM short period seismometer. The seismo-
meter, which essentially measures particle velocity, has a
dramatic effect on the wave form.

Phase Summation

The process of summation of the individual phases (for
the vertical component of motion) in the time domain is illus-
trated in Fig. 4.9. The composite signal shown in Fig. 4.9f
corresponds to the first arrival mantle phase at 4066 km. It
is probable that this entire wave form would be taken to re-
present a single P wave and, for example, the "first arrival"
P wave spectrum would be computed from it, giving the spectrum
of Fig. 4.6d. On the other hand, it is clear that the first
motion is appropriate to the direct explosive P wave from the
source and the m_b value measured from peak to peak during
the first cycle would be unaffected by pP reflections and
tectonic release, even if the tectonic release were several
times larger than shown here.

Figure 4.10 shows the expected time domain composite
signals with and without tectonic release effects. The re-
sults of Fig. 4.9 and 4.10 are typical in that tectonic re-
lease may have an appreciable effect on the signal shape but,
in general, does not affect m_b. This is because the major
tectonic phase, sP_T, arrives too late while the earlier
arriving P_T and pP_T are too small to change m_b. Also
shown in Fig. 4.10 are synthetic seismograms including a
second mantle arrival. This illustrates our ability to gener-
ate a long time segment of the seismogram including all source

77
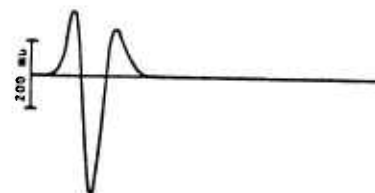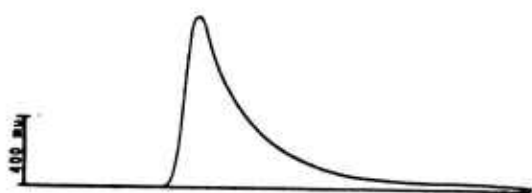
(a) Direct P wave from explosion.
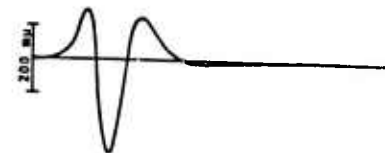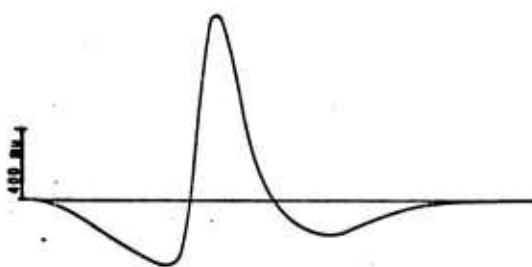
(b) Direct P wave from tectonic release.
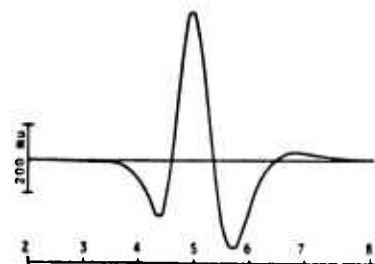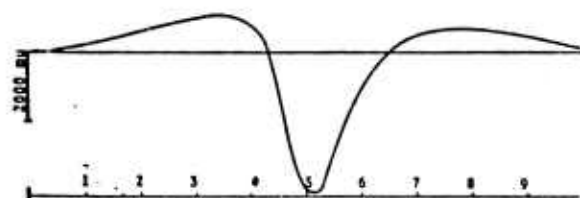
(c) Converted S to P wave from tectonic release.

Fig. 4.8--Comparison of the true displacement at the free surface and the seismometer output for the vertical components of displacement for phases from the Handley event. (Distance 4066 km, explosion source model T-4, prestress σ_{13} = 65 bars, source depth 1.2 km.)

78
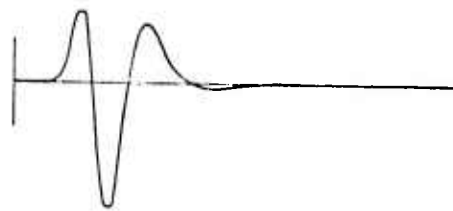
(a) Direct P wave from explosion (P_E)
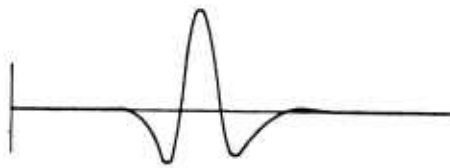
(b) Surface reflected P wave from explosion (pP_E)

(c) Direct P wave from tectonic release (P_T)

(d) Reflected P wave from tectonic release (pP_T)
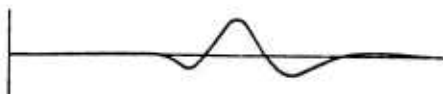
(e) Surface converted S to P wave from tectonic release (sP_T)
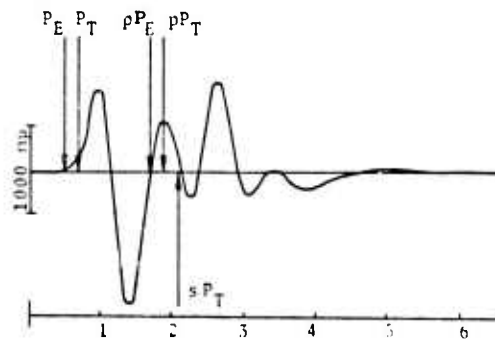
(f) Composite first mantle arrival series.

Fig. 4.9--Theoretical compressional (P) wave phases generated by the Handley explosion and associated tectonic release. The Handley event (1000 kT) modeled by the explosion source model T-1. Prestress (σ_{13}) for tectonic release taken to be 65 bars, shatter zone radius R_0 = 750 meters. Earth structure CIT 109--Low Q model. Distance 4066 km, azimuth 30°. Vertical component LRSM short period seismometer, source depth 1.2 km.
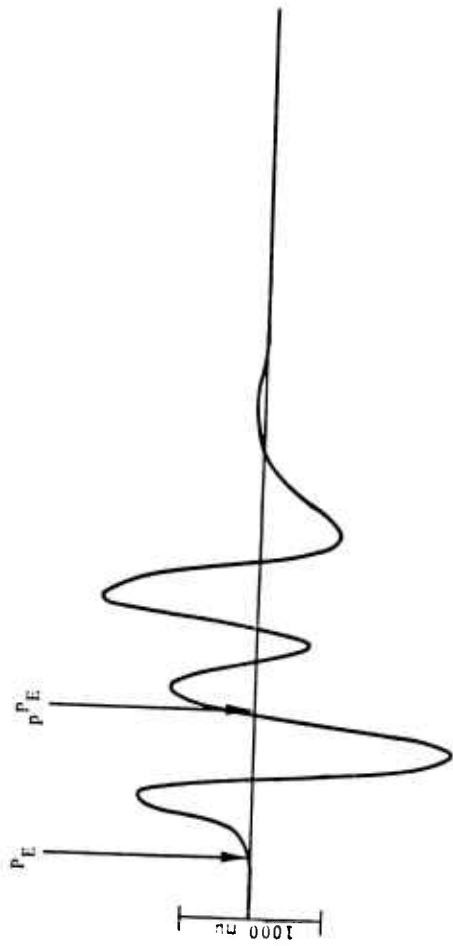
(a) First mantle arrival, explosion plus tectonic release.

(b) First mantle arrival, explosion only.
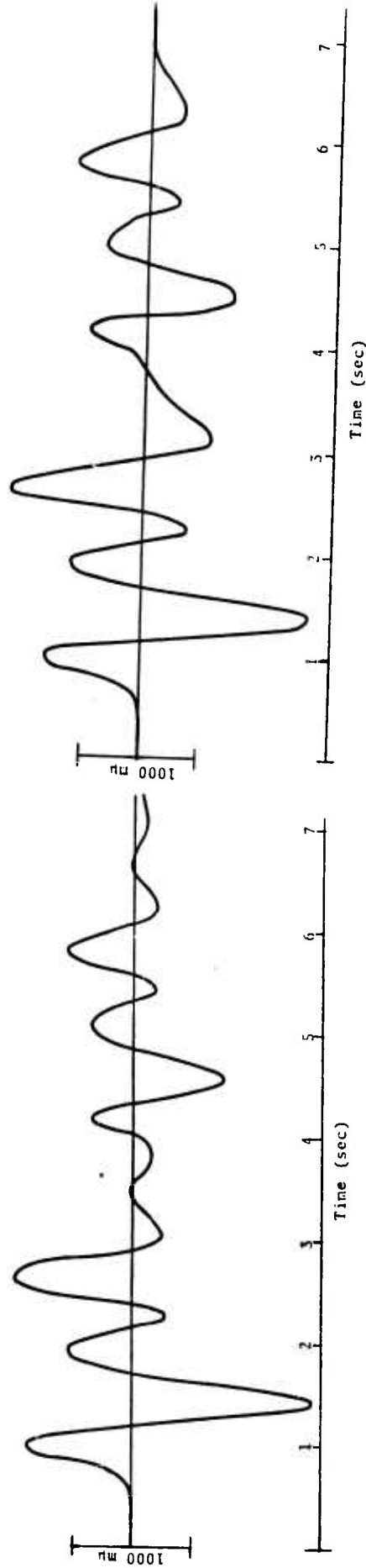
(c) First and second mantle arrivals, explosion plus tectonic release.

(d) First and second mantle arrivals, explosion only.

Fig. 4.10--Comparison of theoretical signals at 4066 km from Handley (1000 kT) explosion model with and without tectonic release. Explosion model was T-1, tectonic release based on 65 bar pure shear prestress ($\sigma 13$) and shock generated shatter zone of 750 meters in radius, source depth 1.2 km.

effects as well as free surface reflections. Further, we routinely generate the S (body) wave portion of the seismogram and surface waves (Section III) as well as the P waves, so that most of the complex signal train generated by an event is synthesized in a series of rather fast computations.

Typical Seismograms

To illustrate the degree of agreement that is possible with our computational model, we compared the observed signal from the Bilby event (200 kt in tuff) at LRSM station HNME (4066 km from the NTS site) to a synthetic seismogram in Fig. 4.11.* For this computation the tuff model T-3, which has a displacement pulse somewhat larger than that of T-4 (Fig. 4.2), was used. While the amplitude scale of the observed record is not known, the LRSM reported A/T of 107 millimicrons for HNME compares favorably with the A/T of 127 millimicrons for the first cycle of the synthetic seismogram.

The S wave portion of the synthetic seismogram for the event just described is portrayed in Figs. 4.12 and 4.13. In Fig. 4.12 the individual phases are shown along with their summation, the first mantle arrival, for both vertical and tangential motion. The first two mantle arrivals for the vertical and tangential components of motion are shown in Fig. 4.13.

---

*The synthetic seismograms of earlier figures were hand drawn from computer plots; hence the smooth curves. This and succeeding synthetic seismograms were drawn by an SC-4020 plotter. The small oscillations at the beginning of the record are introduced by the numerical Fourier transform.
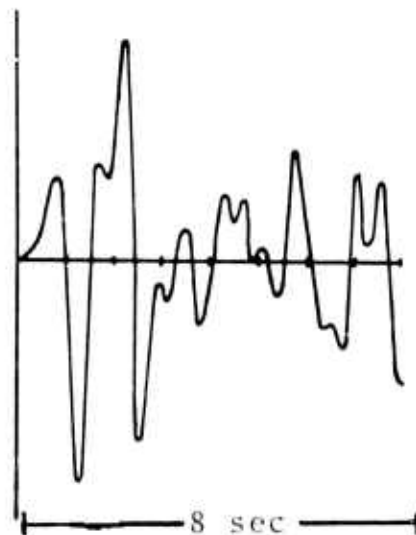
(a) HNME LRSM SPZ record for Bilby.
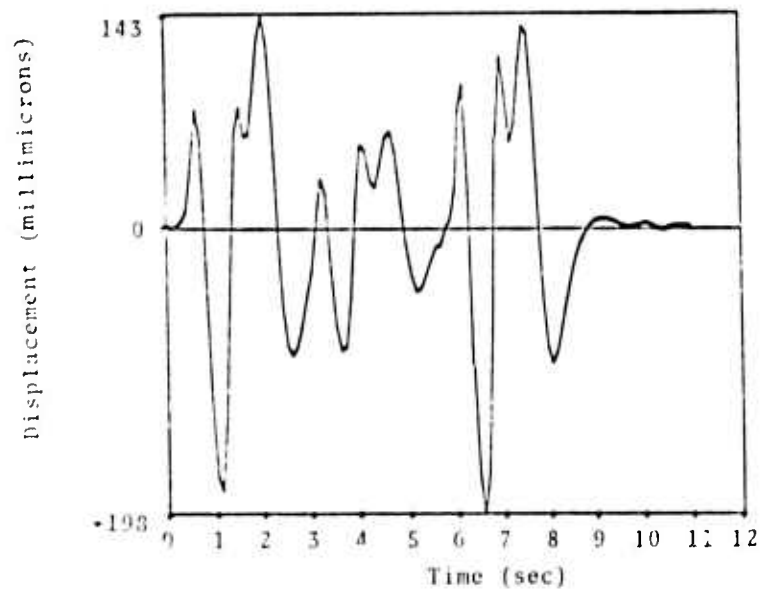
(b) Vertical displacement for explosion source model T-3 with tectonic release (prestress $\sigma_{12} = \sigma_{13} = 160$ bars, shatter zone radius $R_0 = 0.6$ km) propagated with earth model CIT 109 Low Q, source depth 0.7 km.

Fig. 4.11--Comparison of observed and theoretical seismograms for the Bilby event at HNME, 4066 from ground zero.
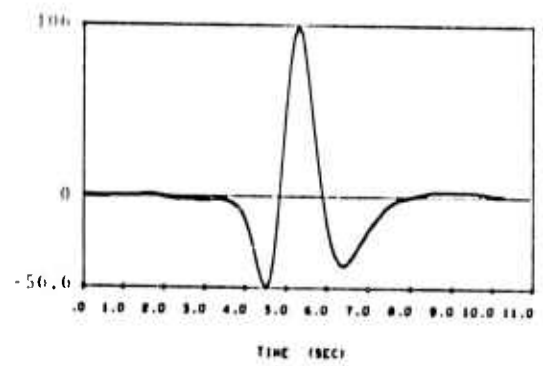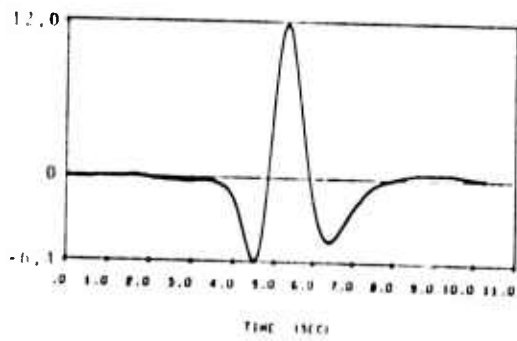
(a) Direct S-wave from tectonic source.
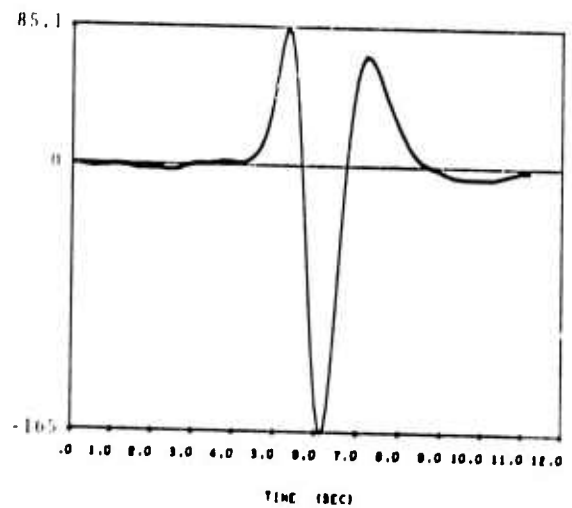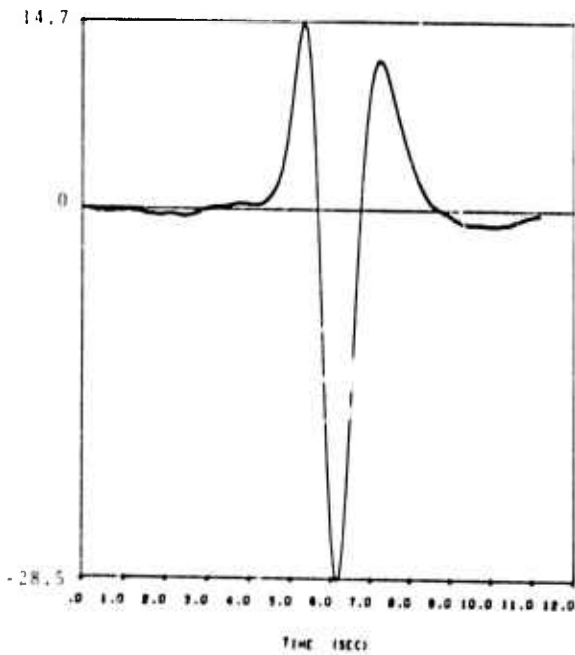
(b) Reflected S-wave from tectonic source.

Fig. 4.12--Construction of the first mantle arrival S-waves for vertical displacement (left column), and tangential displacement with respect to ground zero (right column). Displacements are displayed in millimicrons and times in seconds; the event parameters are given in Fig. 4.11.

83

Fig. 4.12 (Cont.)
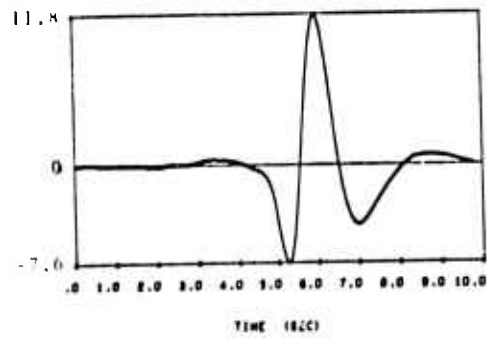
(c) Converted P to S wave from tectonic source.
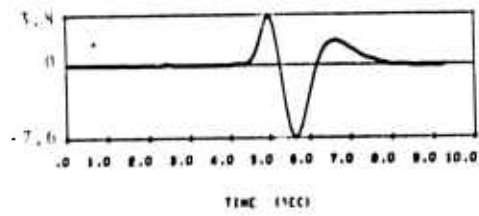
(d) Converted P to S wave from explosion source.
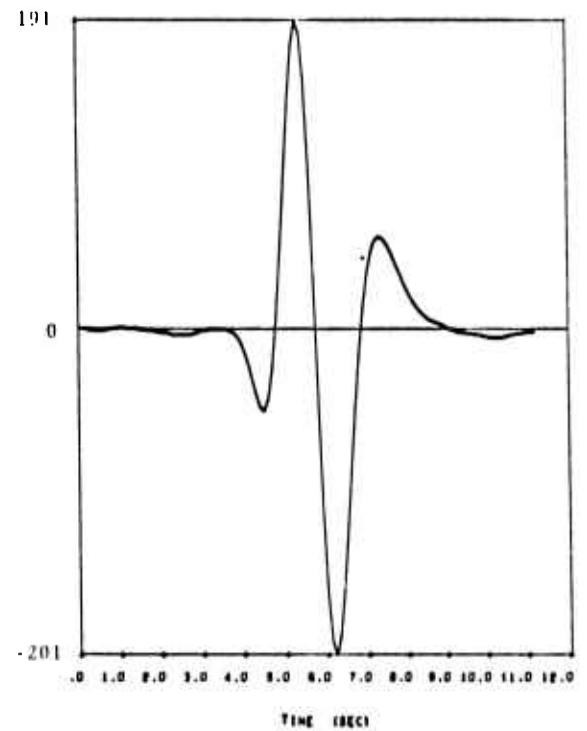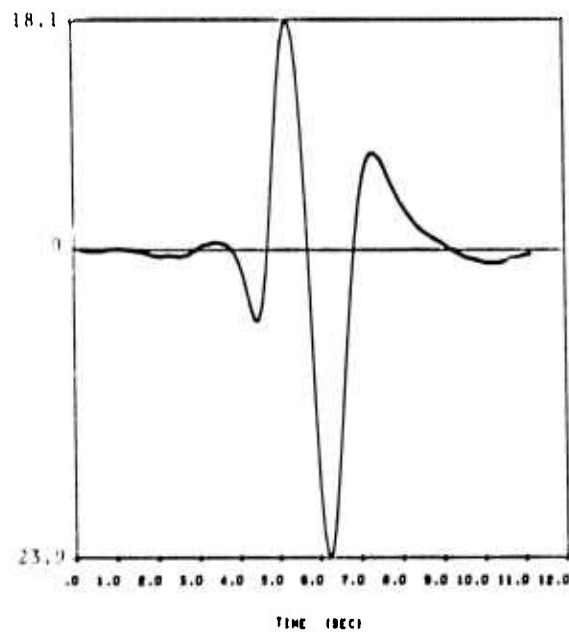
(e) Summation of S-wave. Zero on the time scale corresponds to 773.8 seconds from detonation time.

84
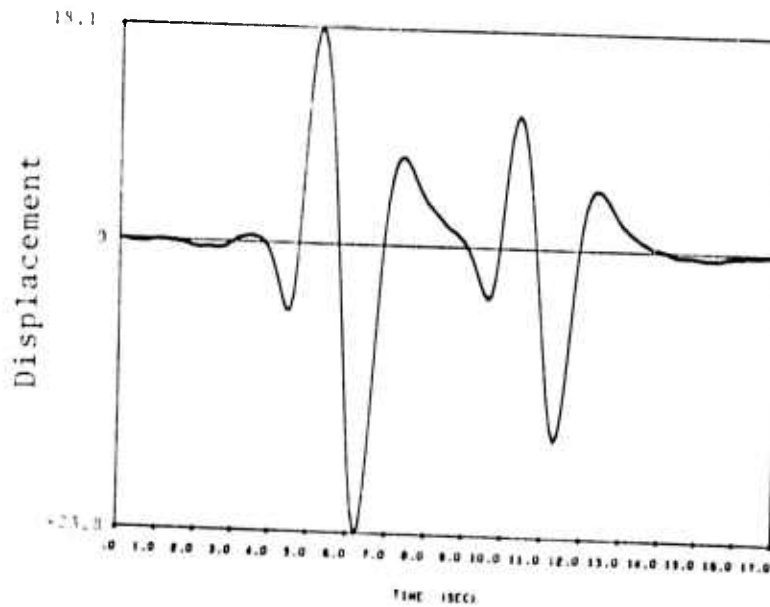
(a) Vertical displacement
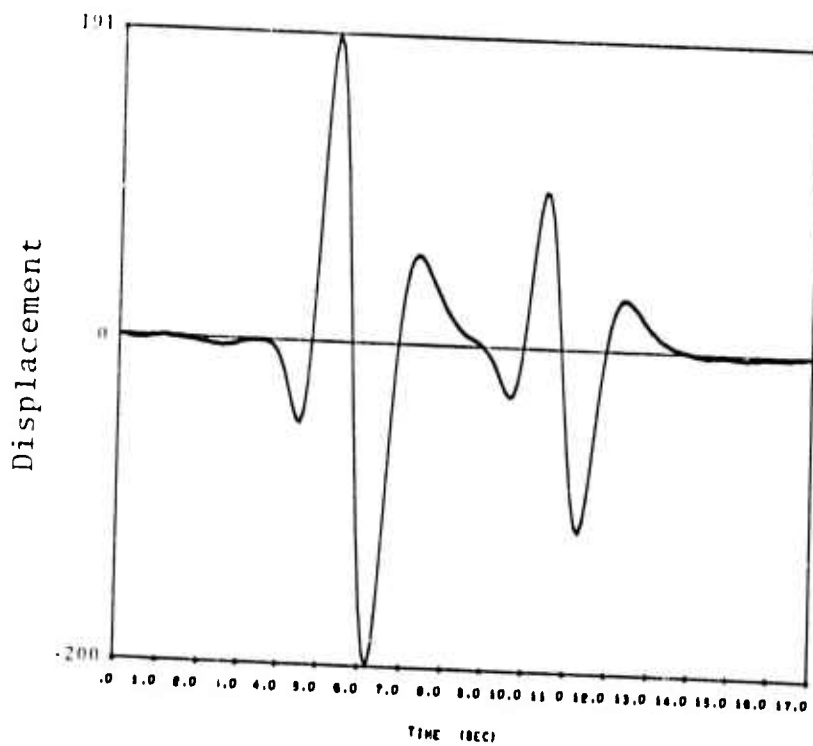
(b) Tangential displacement

Fig. 4.13--The first two mantle arrivals at 4066 km for the Bilby event described in Fig. 4.11. Displacements are in millimicrons, and times are in seconds. Zero on the time scale corresponds to 776.0 seconds from detonation time.

85

4.3.2 The Effect of Earth Structure on the Teleseismic Record

For reliable teleseismic amplitude predictions, one must have the most accurate earth model available. The arrival times of the various mantle arrivals are entirely dependent on the model used. Further, since the earth acts as a low pass filter, the amplitude and shape of the arriving phases are strongly dependent on the attenuation and dispersive properties of the earth model chosen. Therefore, the earth model must, at a minimum, specify the average compressional and shear velocities with depth, as well as the dissipation function, Q, as a function of depth.

Layered Earth Model

For the work of this report a layered earth model proposed by Archambeau, Flinn and Lambert[23] was used. This model, known as CIT 109, is appropriate, in terms of the upper mantle and crustal structure in the upper 200 km, to the Basin and Range Province of the Western United States. Below about 200 km lateral variations in structure within the earth are such that the velocity structure is a reasonable approximation to a mean earth velocity profile. In Figs. 4.14 and 4.15 the velocity depth profiles for compressional and shear waves are shown. The various upper mantle discontinuities including the low velocity zone and especially the velocity transitions at 400 and 650 km give rise to important later arriving body wave phases at teleseismic distances. The travel time curves showing the timing of all mantle P wave arrivals for the CIT 109 model are shown in Fig. 4.16, along with observations from the Bilby event. This figure shows that the first arrivals may often be followed, within a second or two, by a second arrival and within 5 or 10 seconds by as many as 3 or 4 arrivals. In some distance ranges these may be as large or larger than the true first
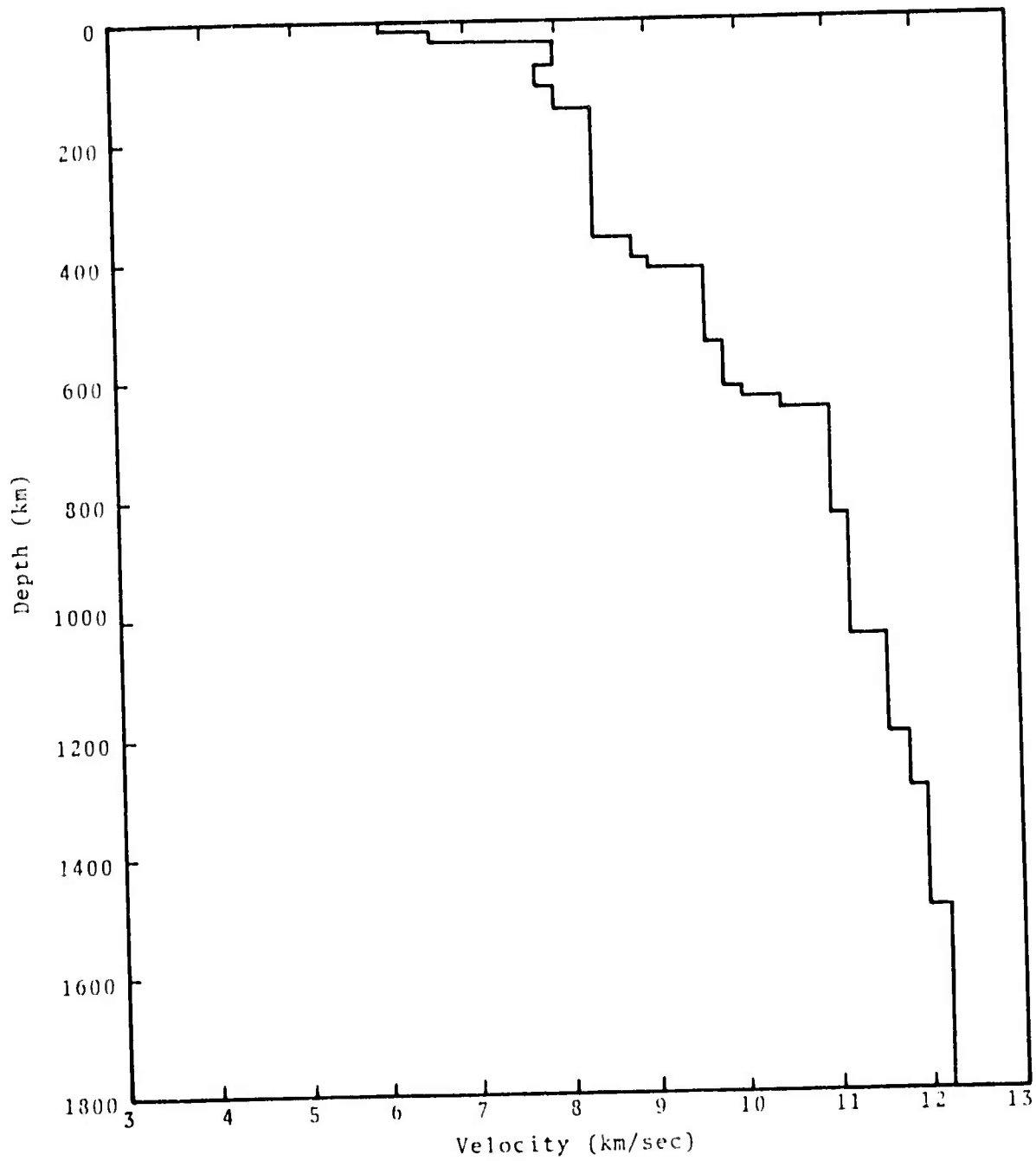
Fig. 4.14--CIT 109 compressional wave velocity versus depth pro-
file for the upper mantle, Basin and Range Province.
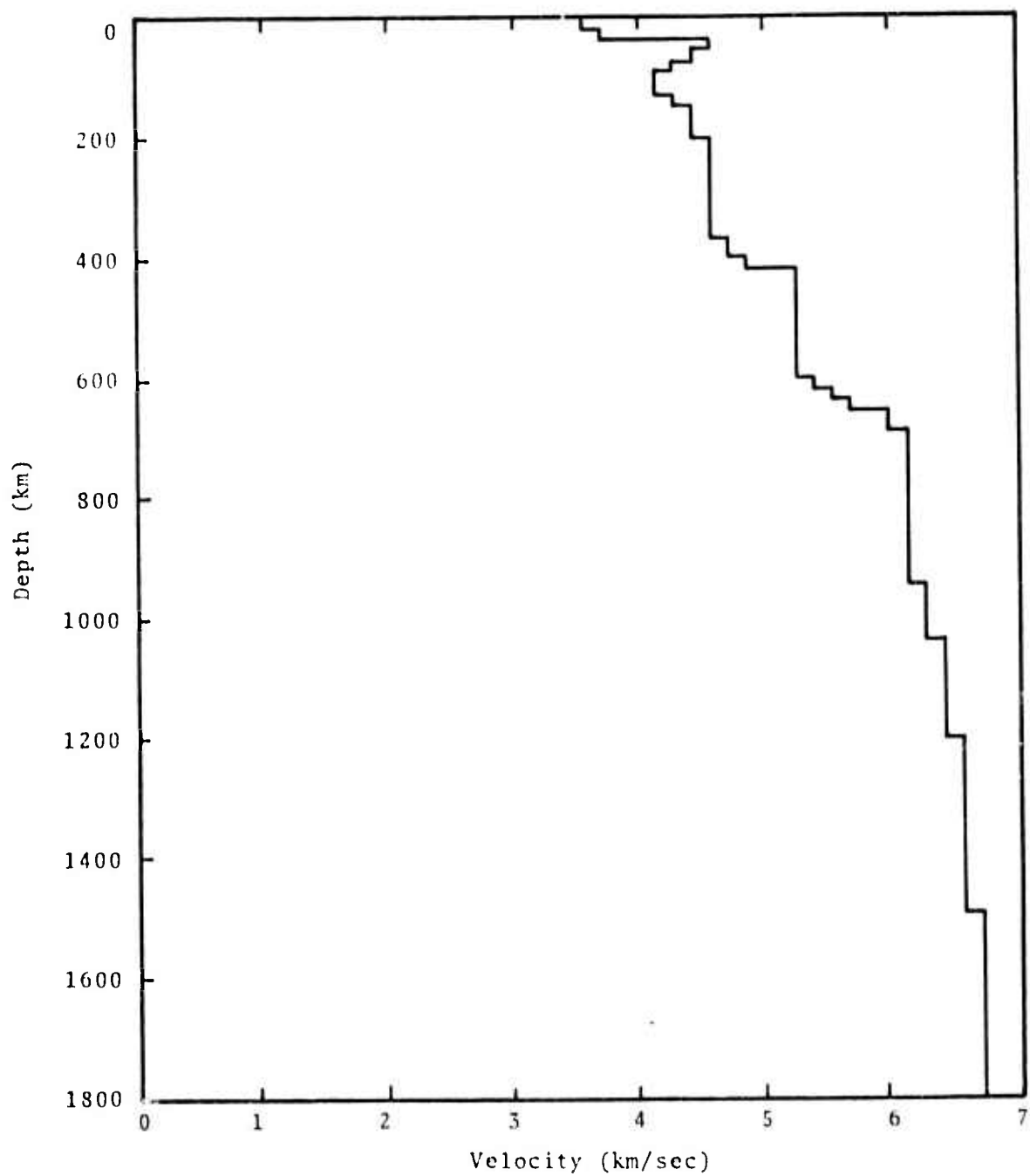
Fig. 4.15--CIT 109 shear wave velocity versus depth profile for
the upper mantle, Basin and Range Province.
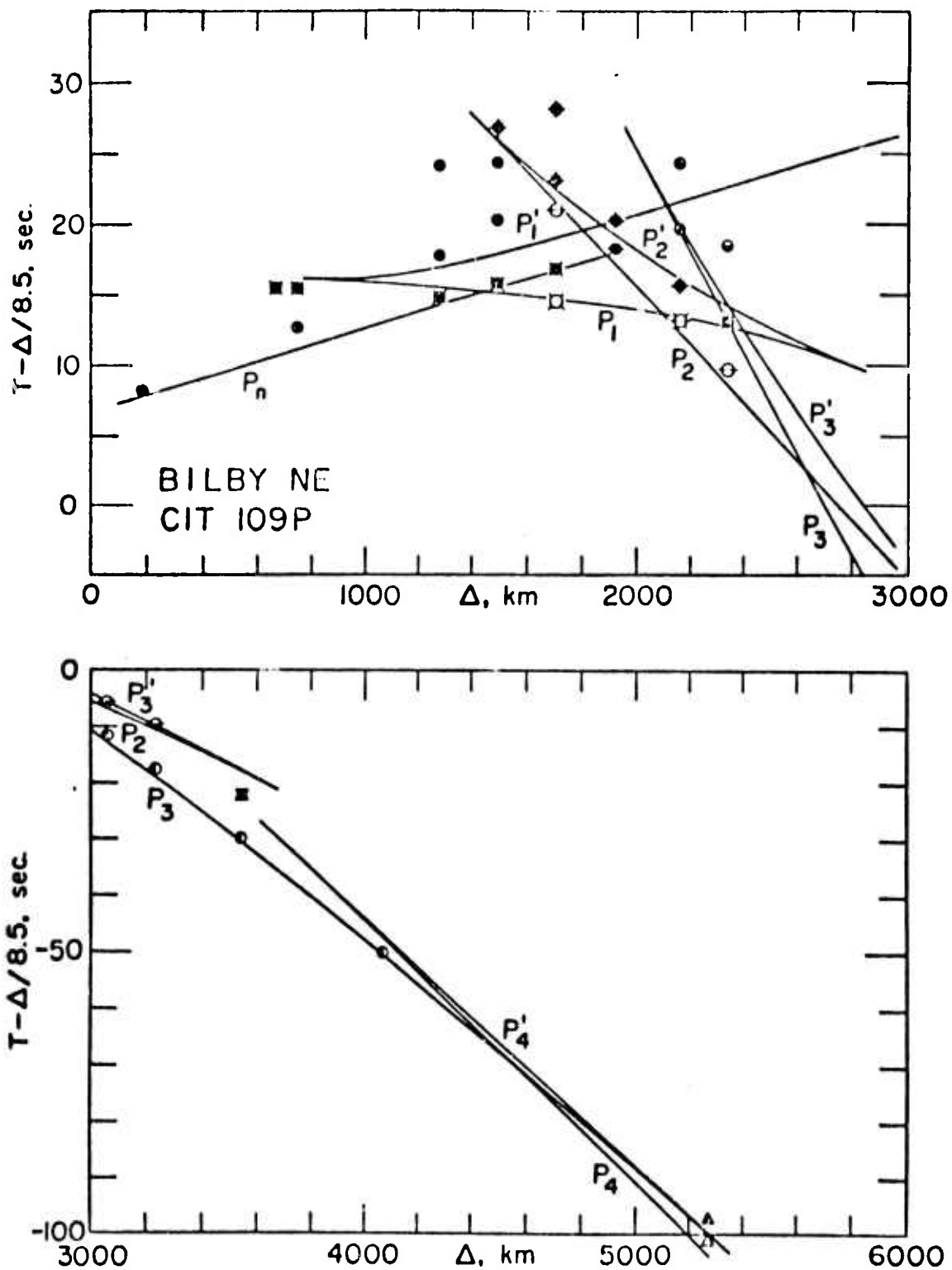
Fig. 4.16--Travel time versus distance curve for the CIT 109P structure. The points shown are observations for the Bilby event. Note the multiple branches of the curve, which arise from the presence of the low velocity zone and velocity transitions at 400 and 650 km in the upper mantle. (Archambeau, et al.[23]).

arrival and strongly affect the character of the observed seismic recording.

The dissipation function Q attenuates and disperses the teleseismic pulse. Several Q models were investigated during the course of this study. In Figs. 4.17 and 4.18 several Q depth profiles for the CIT P and CIT S wave models are shown.

Transfer Function

For the CIT 109P 0.75 Q model, the amplitude of the transfer function, $|A_p(\omega)|$ (see Eq. (4.4)) for $\omega = 2\pi$, is plotted versus distance in Fig. 4.19. This transfer function was calculated for a source depth of 700 meters. Plots of $|A_p(2\pi)|$ for each of the first three arrivals (at 100 km intervals) are shown separately on the figure. Plots for the other Q models, CIT 109P High Q and CIT 109P Low Q, take a similar form, merely being shifted above or below the plots of Fig. 4.19.

The transfer functions for other frequency components of interest for teleseismic P waves exhibit a distance dependence similar to that of the $\omega = 2\pi$ component, therefore Fig. 4.19 is essentially a plot of amplitude versus distance for P wave arrivals. The travel time curves (Fig. 4.16) together with the transfer function curves (Fig. 4.19) give the relative amplitudes and travel times of the P wave mantle arrivals at teleseismic distances. Two examples of the resulting synthetic seismograms are shown in Fig. 4.20. Note that at 3000 km the second two arrivals interfere, greatly complicating the record.
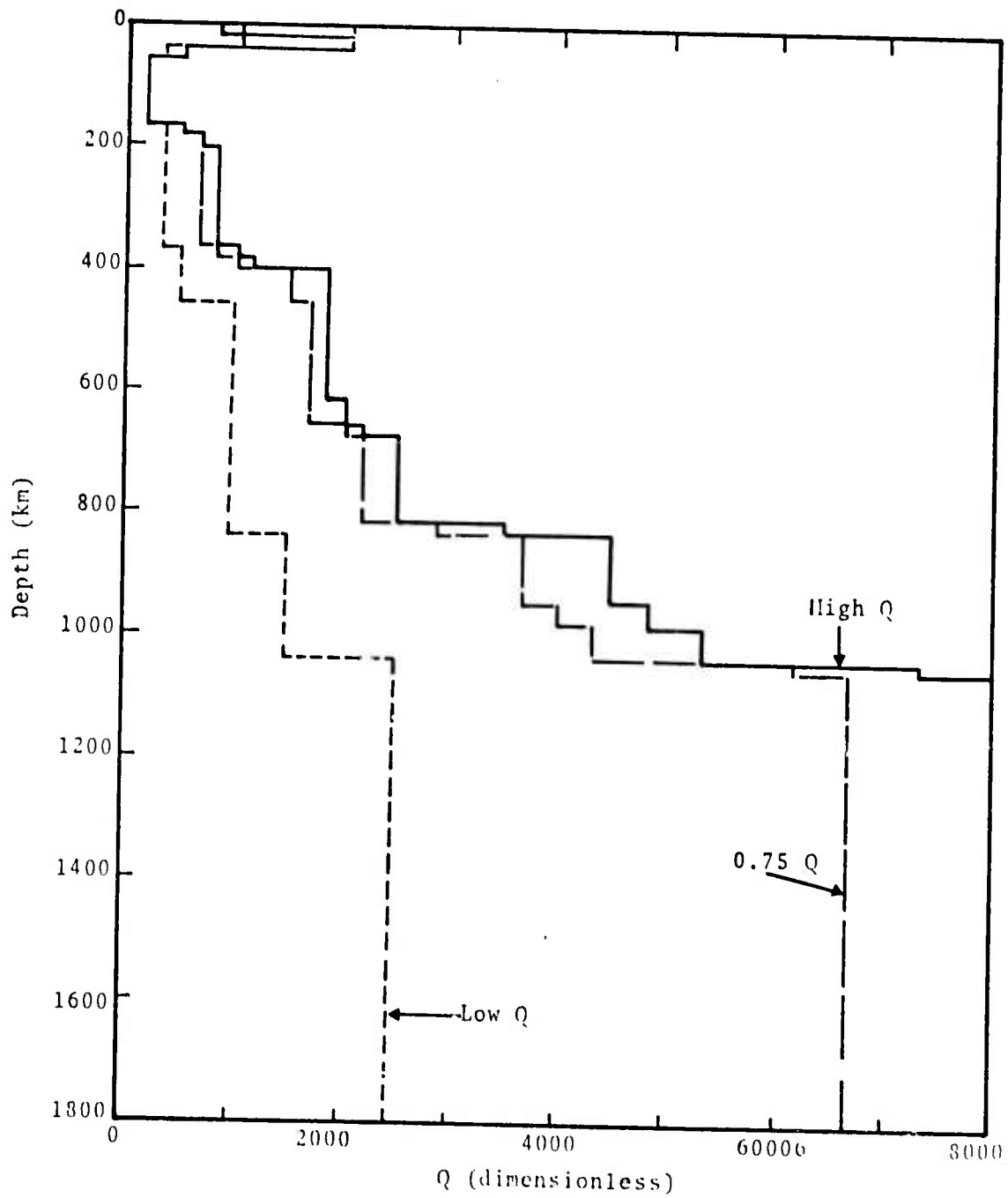
Fig. 4.17--Depth profiles of the dissipation function Q for three P-wave models.
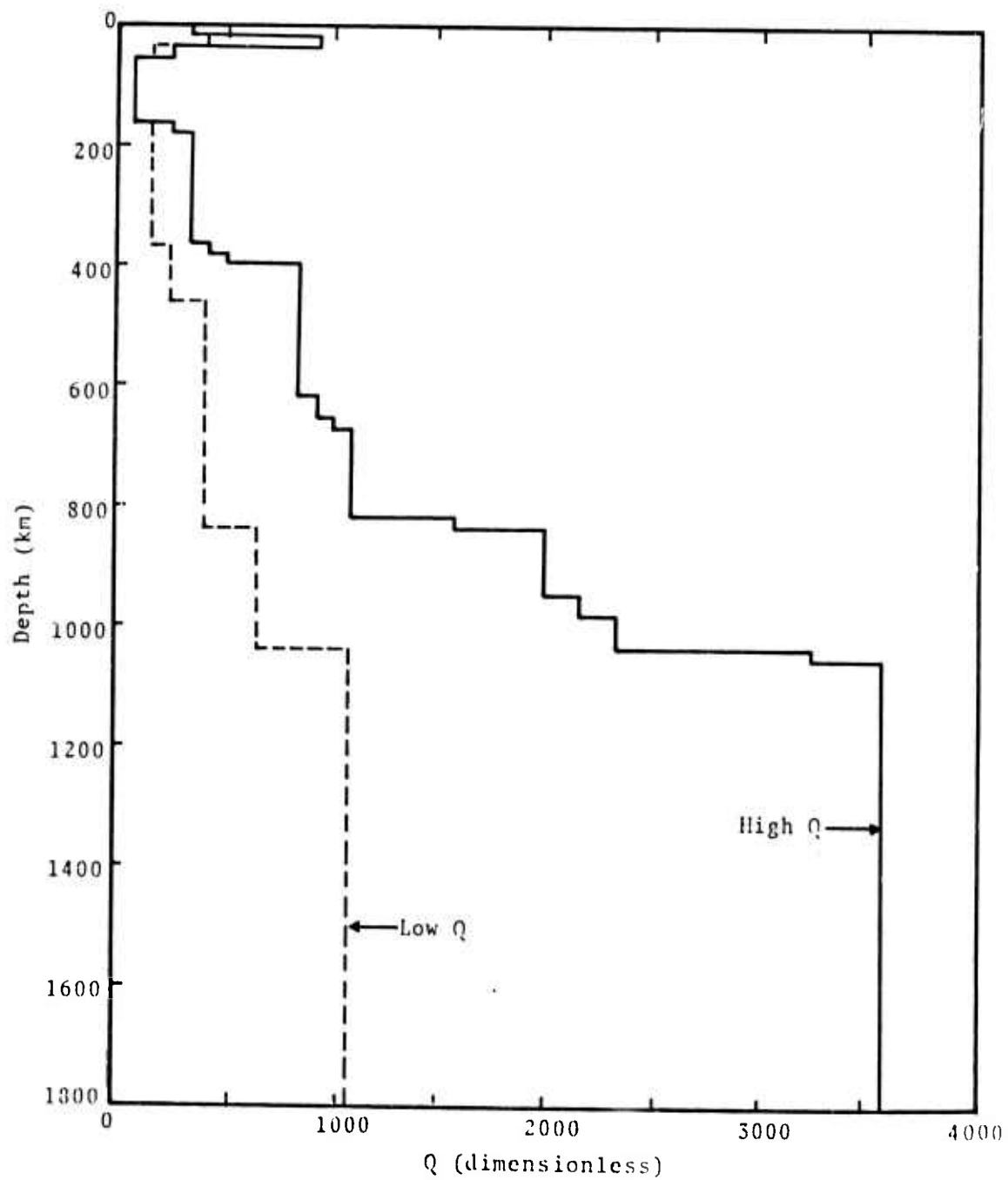
Fig. 4.18--Depth profiles of the dissipation function for two S-wave models.
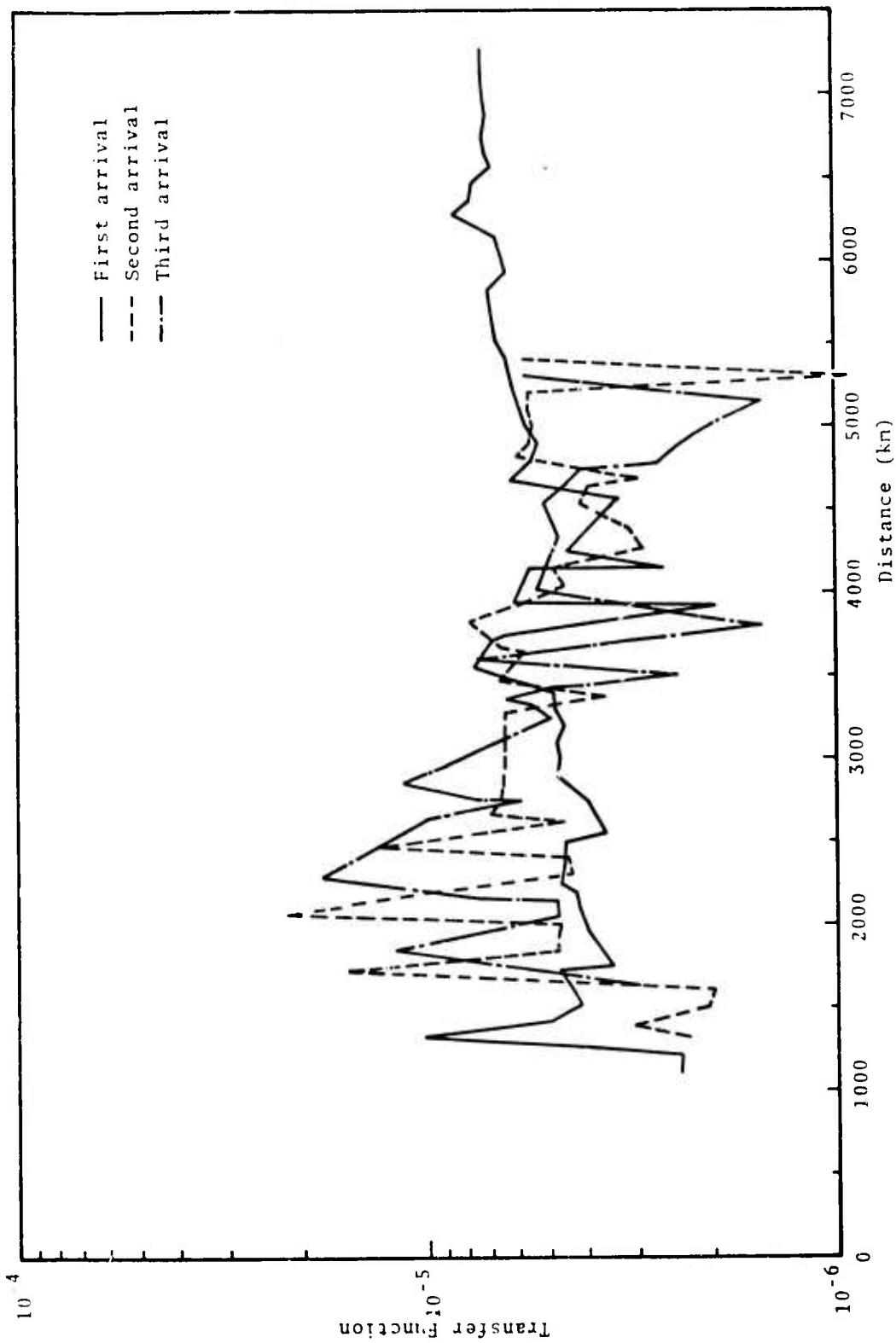
Fig. 4.19.--Transfer function versus distance for earth model CIT 109P 0.75 Q (for an event at a depth of 700 meters). The arrivals within 100 km intervals are ordered by travel time.
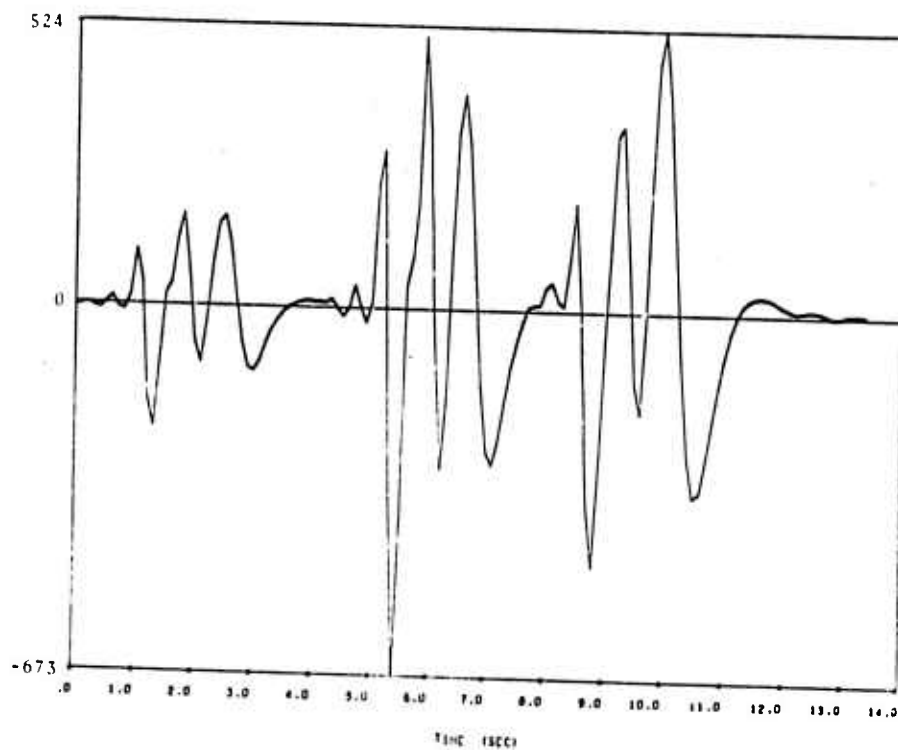
(a) First three mantle arrivals at 2500 km. Zero on the
    time scale is 299.2 seconds from detonation time.
    (Seismogram appropriate to the Bilby event with tectonic
    release--see Figs. 4.31 and 4.33.)
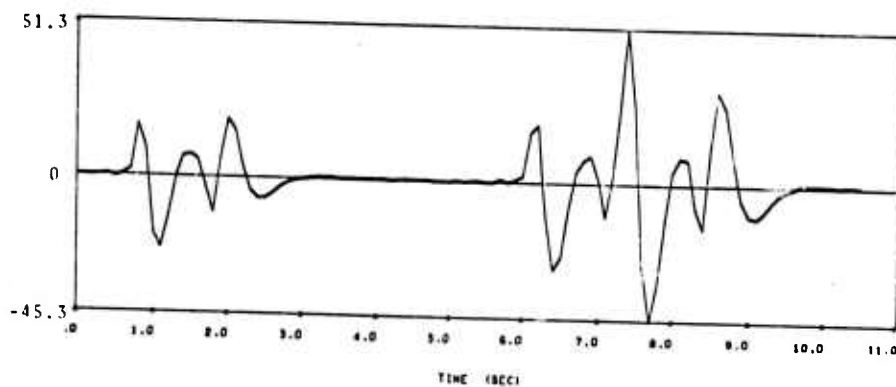
(b) First three mantle arrivals at 3000 km. Zero on the
    time scale is 341.9 seconds from detonation time.
    (Seismogram appropriate to the Rulison event (no tec-
    tonic release)--see Fig. 4.39.)

Fig. 4.20--Two synthetic seismograms illustrating the relative
          amplitudes and arrival times of the first three
          mantle arrivals. The displacements are measured in
          millimicrons.

94

The Effect of Q

The dissipation function Q attenuates the traveling P wave. Since our earth model is dispersive, Q also affects the shape of the arriving wave form, with decreasing Q causing increased spreading of the arriving pulse. This effect is illustrated in Fig. 4.21 where the first mantle arrival from an explosion (with no tectonic release) is depicted for the three Q models. The quantities A_1, T_1, A_2, T_2, which are defined in Fig. 4.21(a), are the amplitudes (in millimicrons) and periods (in seconds) of interest for calculating m_b.

The attenuating and dispersing effects of Q are apparent from the three records of the direct P wave. Since the explosion depth is rather shallow, the direct and free surface reflected P wave phases exhibit considerable interference with varying effects on the seismograph record, depending on Q.

Calculation of m_b

The synthetic seismograms of Fig. 4.21 are appropriate to the Benioff short period instruments of the LRSM stations. As outlined in the LRSM shot reports (e.g., Ref. [19]), m_b is picked from the cycle of maximum amplitude among the first few cycles of the record. As will be discussed in subsequent sections, only the first cycle is directly related to the explosion yield with later cycles being affected by free surface reflected phases and, possibly, tectonic release. However, for comparison of our results with observations, we must attempt to closely approximate the LRSM procedure for picking m_b. For records like those of Fig. 4.21 it is likely that the second cycle (of amplitude A_2) would be used.

95
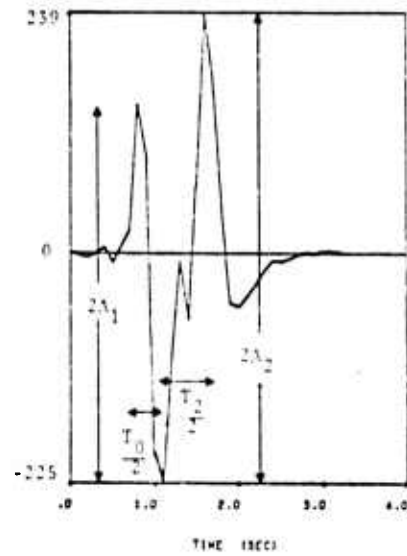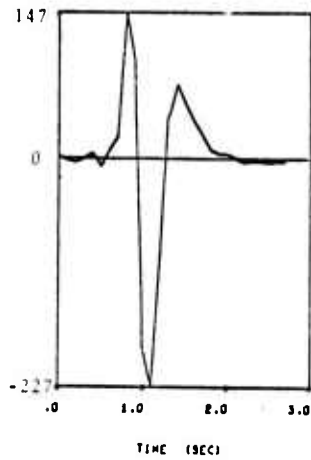
(a) CIT 109P High Q. $A_1 = 187$, $T_1 = 0.6$, $A_2 = 232$, $T_2 = 1$.
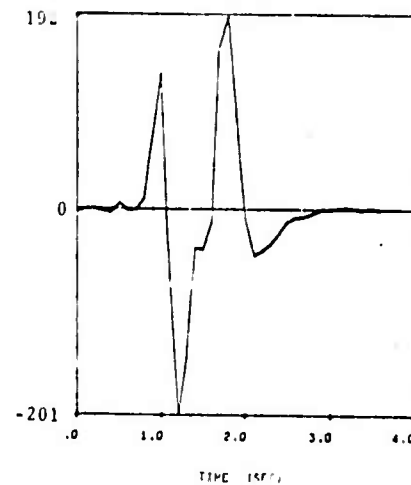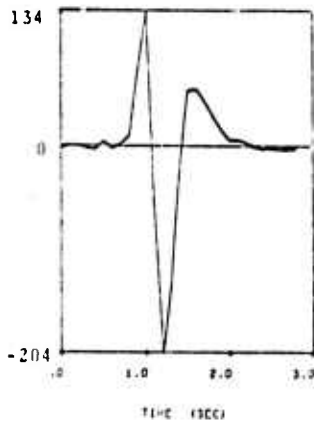
(b) CIT 109P 0.75 Q. $A_1 = 168$, $T_1 = 0.5$, $A_2 = 196$, $T_2 = 1.1$.
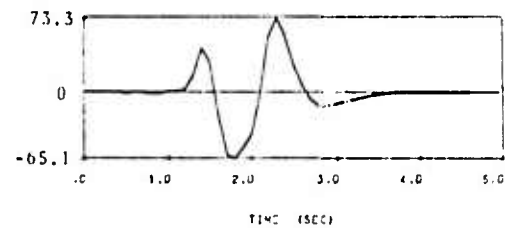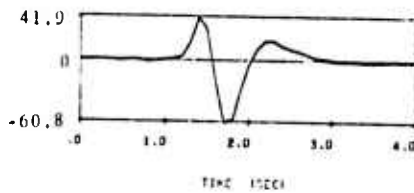
(c) CIT 109P Low Q. $A_1 = 54$, $T_1 = 0.75$, $A_2 = 70$, $T_2 = 1.1$.

Fig. 4.21--Effect of Q on the direct P phase (left column) and first mantle arrival at 4066 km (sum of direct and free surface reflected P waves). Source T-4, DOB 700 m, yield 200 kt. Displacements are in millimicrons.

The body wave magnitude is calculated from

$$m_b = \log \ A_i/T_i \ + B, \tag{4.5}$$

where B is the distance factor (~ 3.54 for 4066 km) and A_i, T_i are defined on Fig. 4.21. The values of m_b for the first $(m_b^{(1)})$ and second $(m_b^{(2)})$ cycles are listed in Table 4.1. The higher value of $m_b^{(1)}$ for each Q model is due to the smaller period for this cycle. The source parameters for Fig. 4.21 are appropriate to the Bilby event, which had an LRSM assigned m_b of 5.8, placing the values of Table 4.1. well within the acceptable range.

TABLE 4.1

COMPARISON OF m_b FOR RECORDS OF FIGURE 4.20

Q Model	$m_b^{(1)}$	$m_b^{(2)}$
High Q	6.03	5.91
0.75 Q	6.07	5.79
Low Q	5.40	5.34

Summary of Earth Structure Effects

The accuracy of our predictions of m_b and the form of the teleseismic record are quite strongly affected by the velocity and Q structures used. The CIT 109 P and S velocity models appear to give good results, but improved detailed agreement with observations could be obtained by refinement or replacement of these models. For example, it would be straightforward to include two layered earth models in our computations; one for propagating the ray from the source region to its deepest penetration, and one for propagating the ray from its turning point to the receiver, which may be located on a quite different earth structure. Further,

since crustal reverberations have a significant effect, these also could be modeled for receivers of interest.

4.3.3   The Effect of Depth of Burial on the Teleseismic Record

The burial depth of the explosion source affects the teleseismic record in several fundamental ways. By far the most important of these is the interference between the direct (P) and free surface reflected (pP) waves leaving the source vicinity. Other depth of burial (DOB) effects include the variation of local material properties and overburden pressure. Finally, great DOB changes could significantly alter the transfer function for the source to receiver travel path.

Material property changes are properly considered a source effect since the source spectrum is directly a function of the material properties in the source region. The effect of important source material parameters on the source spectrum is discussed in Section II. Further, it is to be expected that the average source-to-surface P and S wave velocities may also change with depth, thereby changing the apparent depth of burial. For example, a 10 percent decrease in the average P wave velocity results in an 11 percent increase in the arrival time lag between P and pP, having the effect of increased depth of burial.

The overburden pressure P_0 increases with increasing depth, having the apparent effect of slightly decreasing the yield. In Fig. 4.22 the amplitudes of the RVP transforms $|\hat{\psi}(\omega)|$, from three SKIPPER calculations are compared. The three source models, T-4, T-5 and T-6 in Table 2.2, Section II, are identical except for overburden pressure. With increasing depth of burial we see that the RVP transform exhibits the behavior predicted by the scaling laws (Table 2.1) for decreasing yield; that is, reduced $\dot{\psi}(0)$ and a spectral shift to higher frequencies. These effects are quite minor,
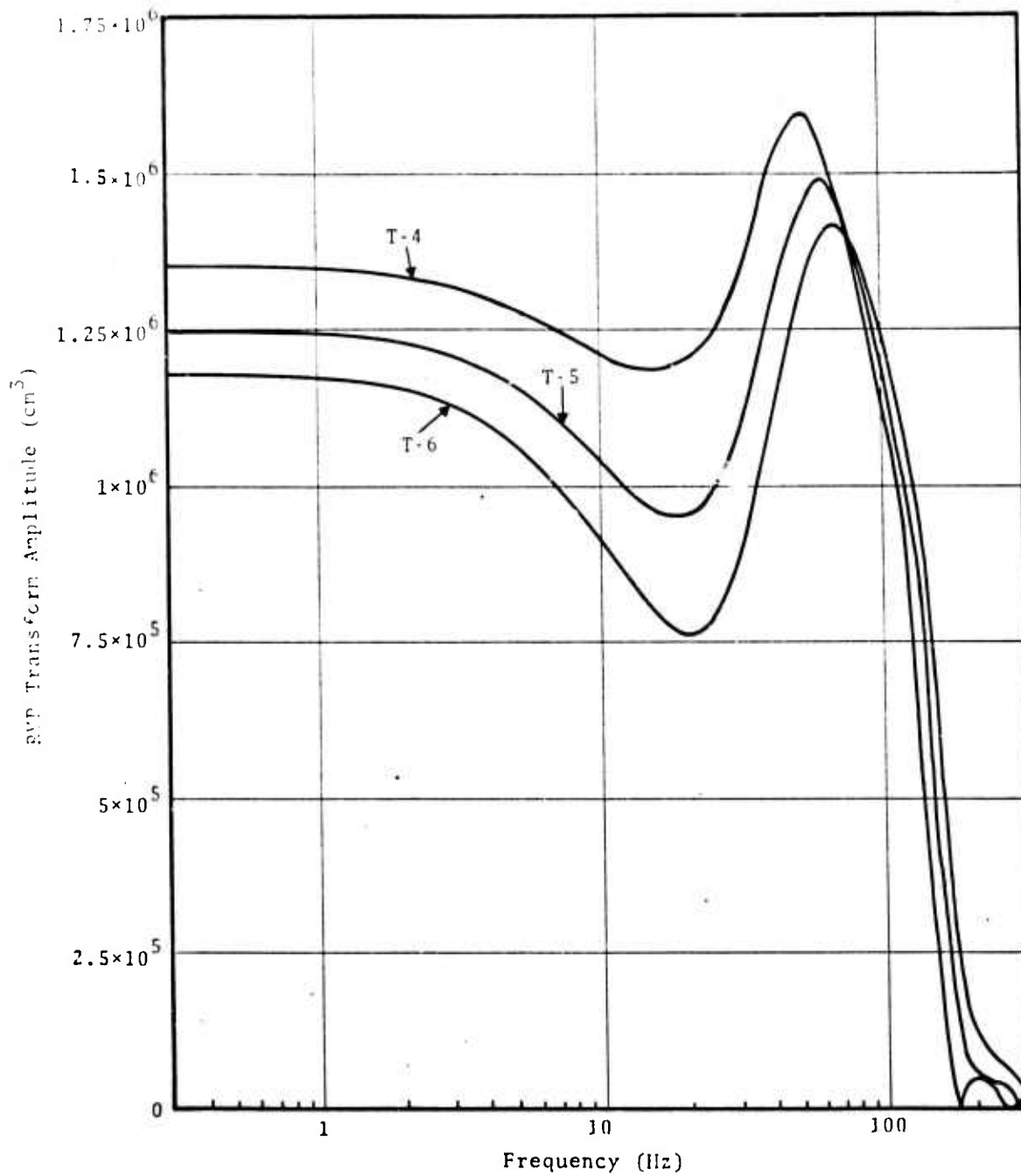
Fig. 4.22--Reduced velocity potential transform amplitude versus frequency for tuff source functions T-4, T-5 and T-6. Scale is appropriate to a yield of 0.02 kt.

however, as a more than twofold increase in depth results in an apparent yield decrease of about 15 percent (based on $\dot{\hat{\psi}}(0)$).

Interference Between P and pP

The most striking feature of the body wave spectra from an explosion is the peaking and scalloping of the spectrum due to interference between the direct and reflected waves. Examples were shown in Figs. 4.5 and 4.6. The effect of the free surface on the spectrum of the observed first arrival P wave train can be demonstrated as follows:

If

$$P = F(t), \tag{4.6a}$$

then

$$pP = -AF(t - T_0), \tag{4.6b}$$

where

A = free surface reflection coefficient (≈ 1),

$T_0 \approx 2H/v_p$,

H = depth of burial (DOB),

v_p = compressional wave velocity.

In the frequency domain

$$\hat{P} + p\hat{P} = F(\omega)\left(1 - Ae^{-i\omega T_0}\right),$$

100

and

$$|\hat{P} + p\hat{P}| = |F(\omega)| \left|1 - 2A \cos\left(\omega T_0\right) + A^2\right|^{1/2}, \tag{4.7}$$

$$= |F(\omega)| \begin{cases} |1-A|, & \omega = \pm \dfrac{2n\pi}{T_0} \\[3mm] |1+A|, & \omega = \pm \dfrac{(2n+1)\pi}{T_0}, \quad n = 0,1,2,\ldots \end{cases} \tag{4.8}$$

Equation (4.8) shows the modulation of the amplitude spectrum by the free surface reflection, with the spectral troughs and peaks occurring (alternately) at frequencies of

$$f = \frac{n v_p}{4\Pi}, \quad n = 0,1,2, \ldots . \tag{4.9}$$

The effect of Eq. (4.9) is shown in Fig. 4.23 where $|\hat{P}|$, $|p\hat{P}|$ and $|\hat{P} + p\hat{P}|$ are plotted for two hypothetical yields and burial depths. The two calculations were run using the same source function and therefore the same overburden pressure (appropriate to a DOB of 700 m). However, using the proper overburden pressure for the deeper depth would result in only a slight downward shift of the three curves for 1400 kt. The material properties in the source region were also held constant for both calculations, with the source-to-surface compressional wave velocity being 2.4 km/sec.

To demonstrate that the spectral shift of Fig. 4.23 is almost entirely a DOB effect, in Fig. 4.24 the vertical component of $|\hat{P} + p\hat{P}|$ is plotted for six yields ranging from 1 to 800 kt with the source-to-surface travel time remaining constant.
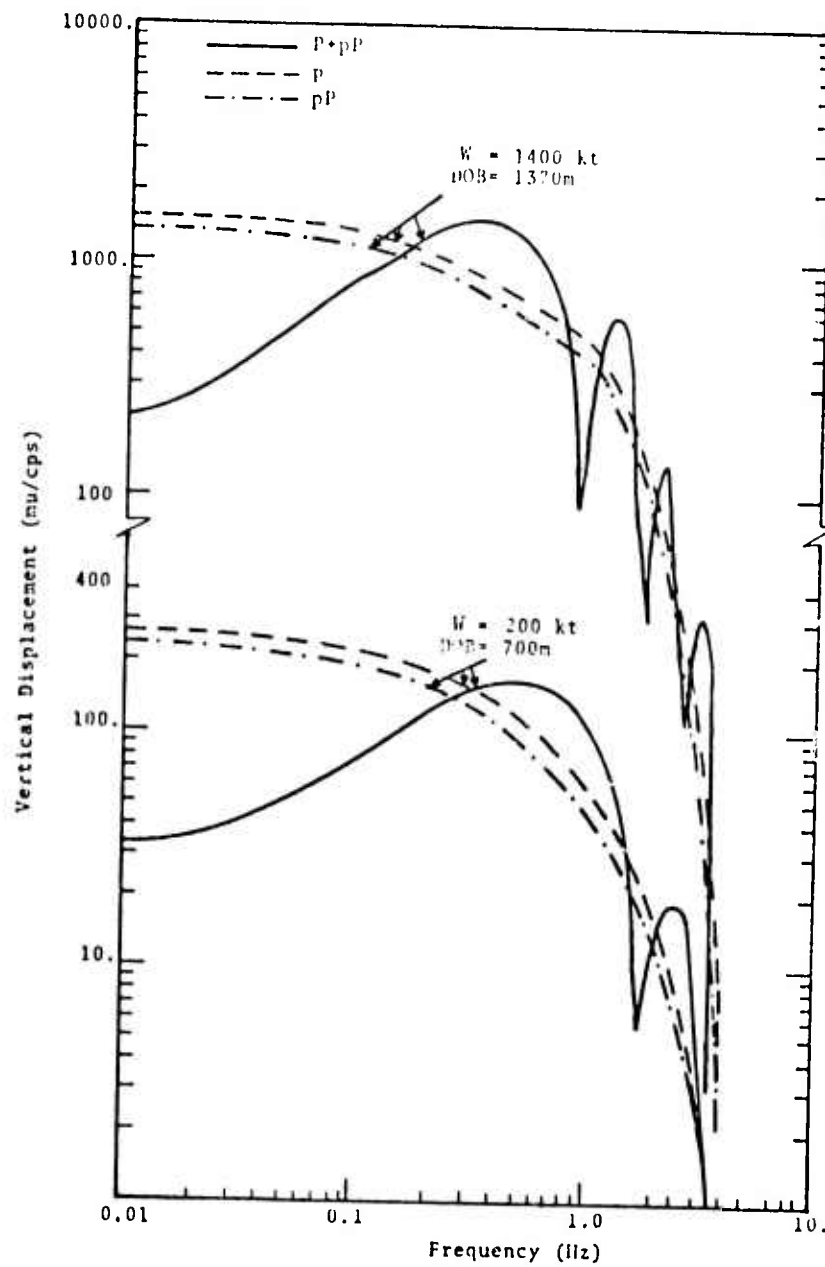
Fig. 4.23--Vertical component P wave spectra at an epicentral distance of 3000 km for RDP source T-4 at two yields and burial depths.
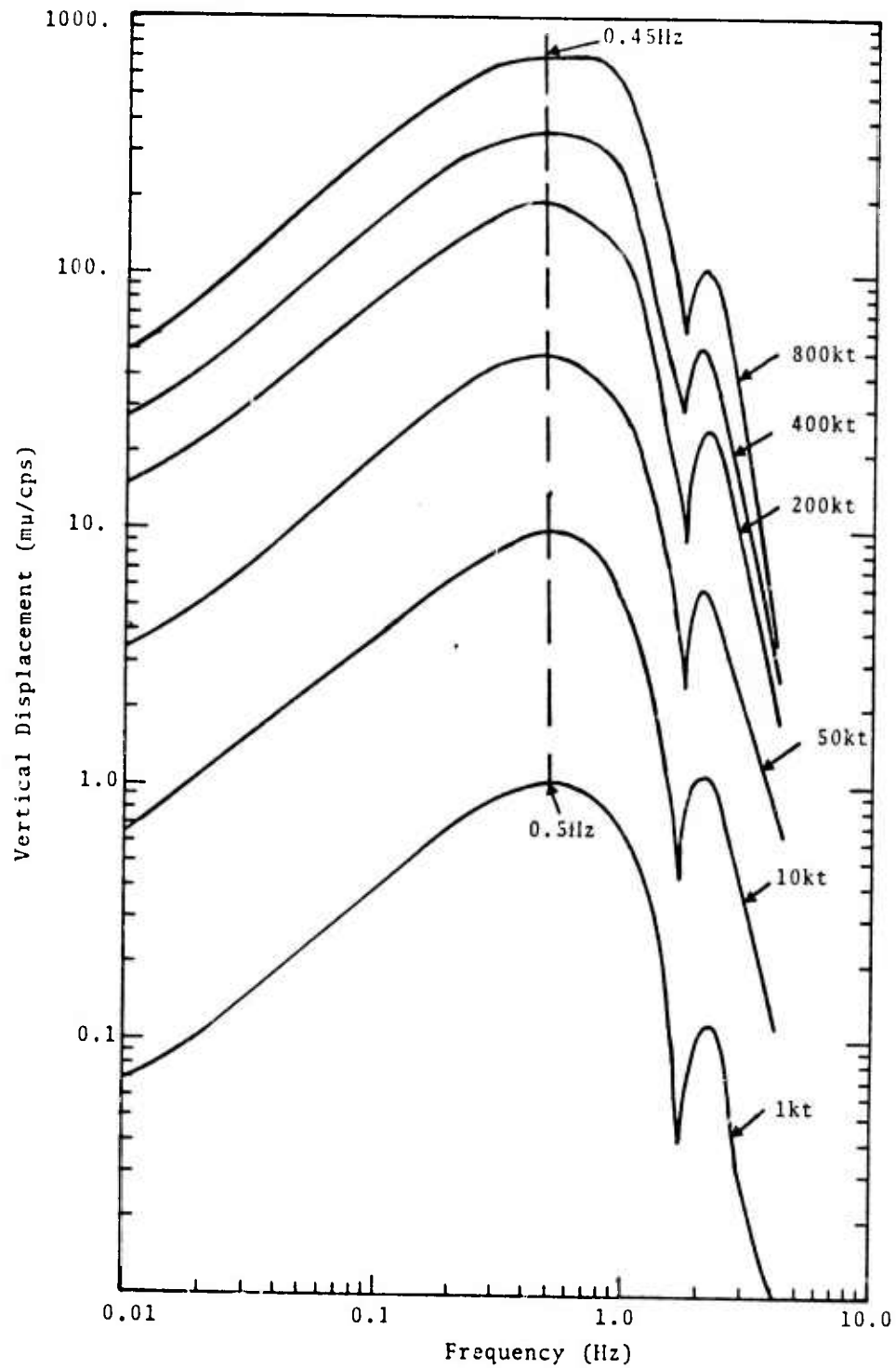
Fig. 4.24--Vertical component P wave spectra for various yields
at a constant DOB = 700 m. Data is for T-4 at an
epicentral distance of 5000 km.

The Effect of pP on m_b

The effect of free surface reflections on the tele-
seismic record is best examined by fixing all parameters
(yield, source spectrum, source-to-surface velocity) but the
depth of burial and studying synthetic seismograms due to
the explosion only (no tectonic release). Since the trans-
fer function for the source-receiver ray path has equal
effect on P and pP, only the arrival time lag between the
two is significant.

In Fig. 4.25, synthetic seismograms for depths of 700
and 1200 meters are compared.* Using Eq. (4.9), the first
spectral window for the events of 4.21a and 4.21b occurs at
1.7 and 1.0 Hz respectively. Using the same source para-
meters but a different earth model, the depths of 700 and
2573 meters are compared in Fig. 4.26. At the greater depth
pP is so delayed as to appear as a later mantle arrival.

The calculation of m_b from records such as those of
Figs. 4.25 and 4.26 is ambiguous. As briefly discussed in
Section 4.3.2, m_b is calculated from the cycle of maximum
amplitude from among the first few cycles of the record.
The formula (4.5) is then applied. Using this LRSM procedure,
m_b would almost certainly be calculated from the second cycle
on the shallow shots (Figs. 4.25b and 4.26b) and from the
first cycle on the deeper events. The m_b values for these
records are summarized in Table 4.2. It should be pointed
out that the $m_b^{(1)}$ values are, in a sense, anomalous since
the periods T_1 are on the order of 0.5 sec, values seldom
observed for m_b measurements at teleseismic distances.

---

* See Figure 4.21 for definitions of A_i and T_i.
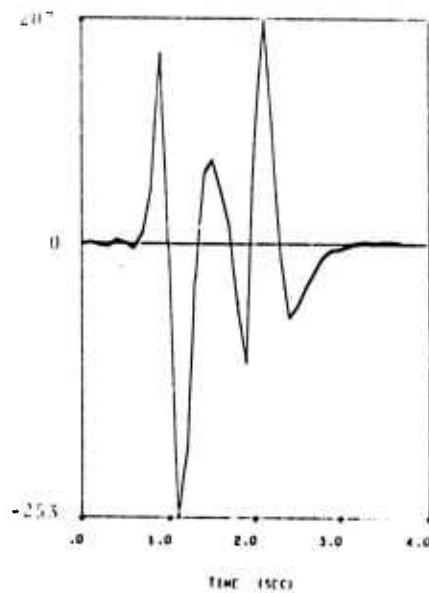
(a) DOB = 1200 meters. A_1 = 215, T_1 = 0.5.
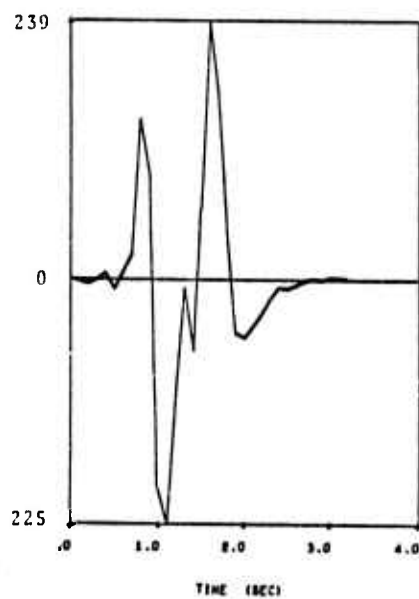
(b) DOB = 700 meters. A_1 = 187, T_1 = 0.6, A_2 = 232, T_2 = 1.

Fig. 4.25--Comparison of first arrival P waves (P+pP), as
recorded at 4066 km, for different depths of burial. Source
T-4, CIT 109P High Q earth model, v_p = 2.4 km/sec. Displace-
ments are in millimicrons.
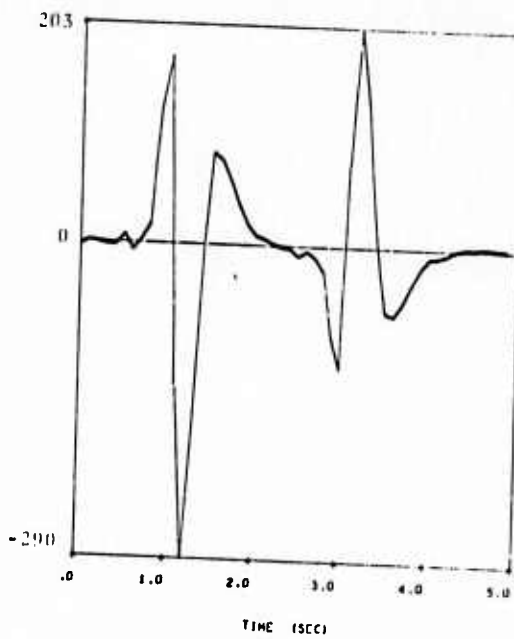
(a) DOB = 2573 meters. A_1 = 230, T_1 = 0.5.
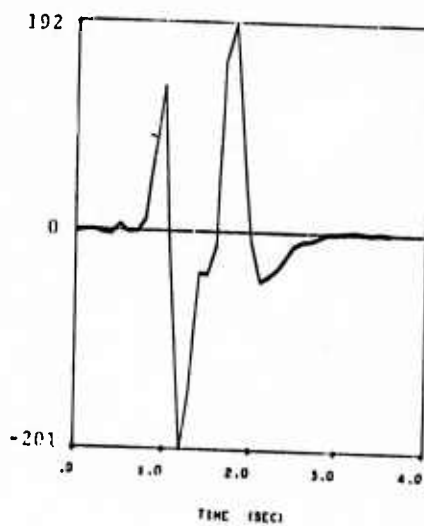
(b) DOB = 700 meters. A_1 = 169, T_1 = 0.5, A_2 = 195, T_2 = 1.1.

Fig. 4.26--Comparison of first mantle arrival P-waves at 4066 km. Source T-4, CIT 109P 0.75 Q earth model, v_p^{ss}=2.4 km/sec. The dis-placements are measured in millimicrons.

TABLE 4.2

COMPARISON OF m_b FOR RECORDS OF FIGURES 4.24 AND 4.25

Seismogram	DOB	Q Model	$m_b^{(1)}$	$m_b^{(2)}$
4.25a	1200 m	High Q	6.17	
4.25b	700 m	High Q	6.03	5.91
4.26a	2573 m	0.75 Q	6.20	
4.26b	700 m	0.75 Q	6.07	5.79

107

Summary of Depth of Burial Effects

Although DOB has some minor influence on the source spectrum, the dominant DOB effect is the shifting of the arrival time of pP with respect to P. For shallow depths the two phases may combine to significantly increase the maximum amplitude on the record. This maximum amplitude, from which m_b measurements are made, is therefore dependent not only on explosion yield but also on DOB. Below a certain depth (about 1000 m for the tuff example treated here), the two pulses disengage on the seismogram and the maximum amplitude is then directly dependent on yield.

4.3.4 The Effect of Yield on the Teleseismic Record

Taken by itself, the effect of the explosion yield is essentially restricted to scaling the record amplitudes directly with yield. In practice a change in yield is generally associated with a change in the depth of burial and, possibly, other parameters of the event, thus obscuring this elementary scaling relationship.

In Fig. 4.24 the total displacement spectra due to a series of explosions over a wide range of yields were displayed. For these events the source environment and DOB were held constant; therefore, the effect of yield is isolated and is restricted, aside from the amplitude scaling, to a very slight shift of the spectrum. This result is a straightforward consequence of the properties of the earth, as will be explained below.

Source Spectrum Changes with Yield

The calculation of the source function by SKIPPER is carried out at a nominal yield of 0.02 kt, then scaled to the yield of interest. The far field displacement spectrum

is directly proportional to the reduced velocity potential
(RVP) transform, $\dot{\psi}(\omega)$ (see Eq. (4.1)). Therefore, the
scaling laws of interest are that $\dot{\psi}(\omega) \sim W$ and $\omega \sim W^{-1/3}$,
where W is the explosion yield.

In Fig. 4.27 $|\dot{\psi}(\omega)|$ for the SKIPPER calculation T-4
(tuff) is shown. The spectral shape is typical of our source
calculations. The amplitudes and frequencies given on the
axes are for a yield of 0.02 kt. Since the amplitude scales
directly with yield, appropriate amplitude values for any
desired yield are quickly obtained. Of greater interest is
the observation that the spectral shape changes with yield.
This is indicated by the additional frequency scales on the
figure for yields of 200, 500 and 1000 kt. As yield increases,
the 1 Hz point on the spectrum moves down the flat part of the
spectrum, through the trough, etc. Therefore, the displace-
ment spectrum in the source region varies significantly with
yield.

Propagation of the source spectrum to teleseismic
distances is accomplished by multiplying by the transfer
function Eq. (4.4). The earth acts as a low pass filter with
the filter attenuation given by Eq. (4.2). In Fig. 4.28 the
attenuation function $\exp[-\omega T/2Q_p]$ is plotted for several
typical ray paths. From this figure it is seen that the
attenuation is quite strong, so strong that details of the
source spectrum are essentially washed out. That is, even
such differing source spectra as those indicated in Fig.
4.27 result in quite similar spectra at teleseismic distances.
The latter assertion is born out by Fig. 4.29 where direct P
wave spectra at 4066 km are compared for several yields. The
spectrum for 0.02 kt has been scaled by 10^4 to juxtapose it
with the others.
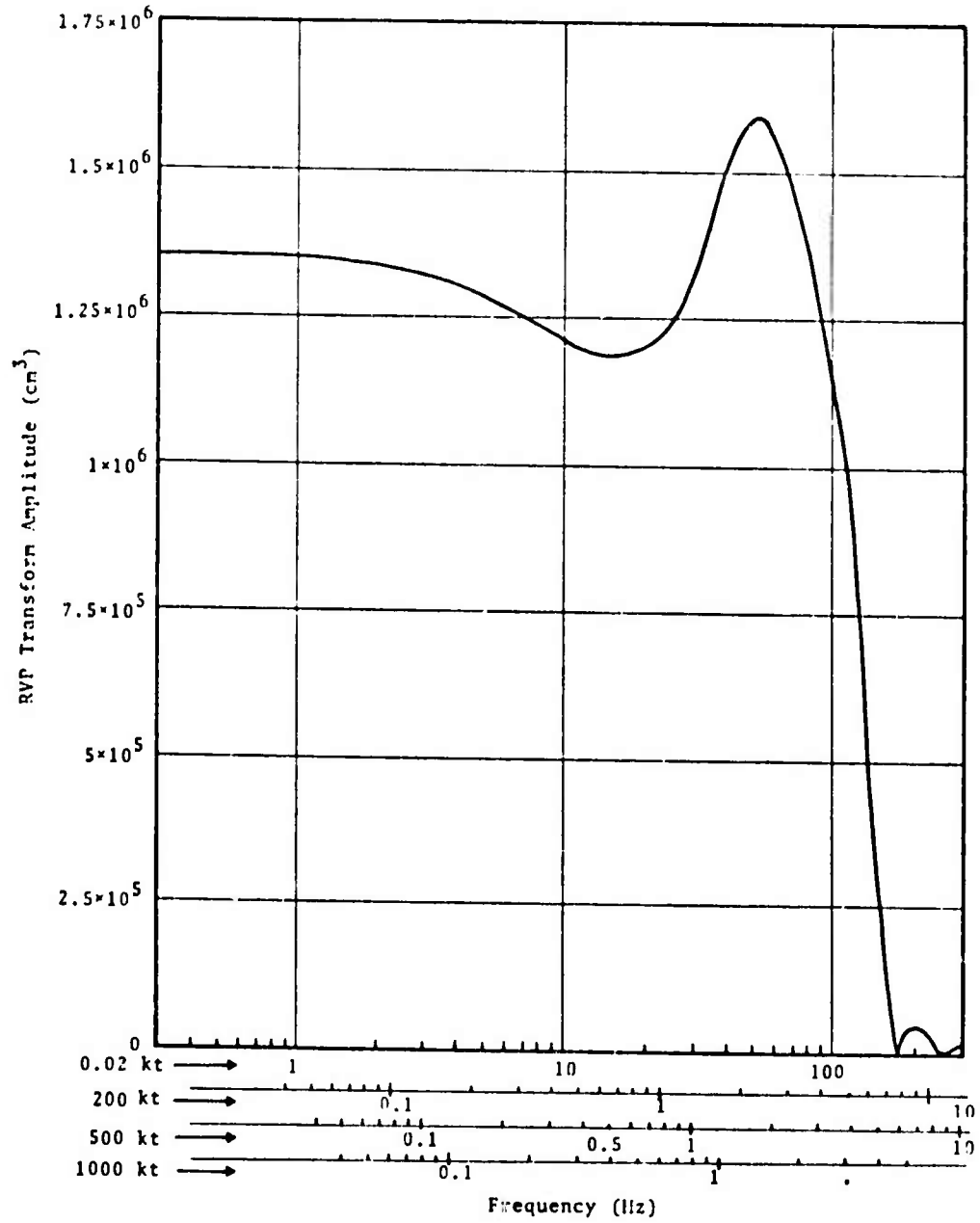
Fig. 4.27--Reduced velocity potential transform amplitude versus frequency for source function T-4. The grid is scaled for a yield of 0.02 kt, while additional scales are shown for yields of 200, 500 and 1000 kt.
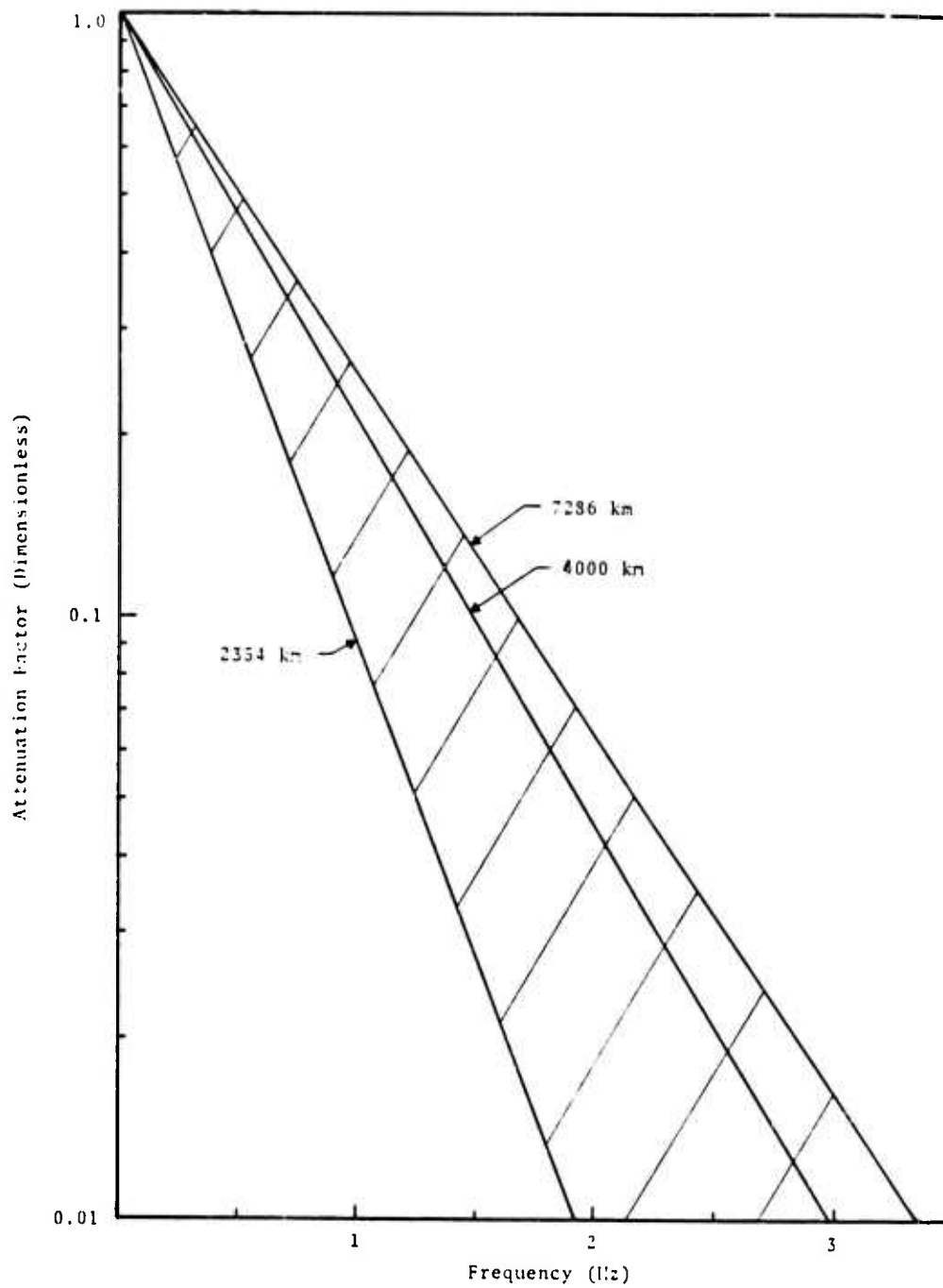
Fig. 4.28--The attenuation function $\exp[-\omega T/2Q_p]$ for three ray paths in the model CIT 109 0.75 Q. All other attenuation functions for this model fall in the shaded area.
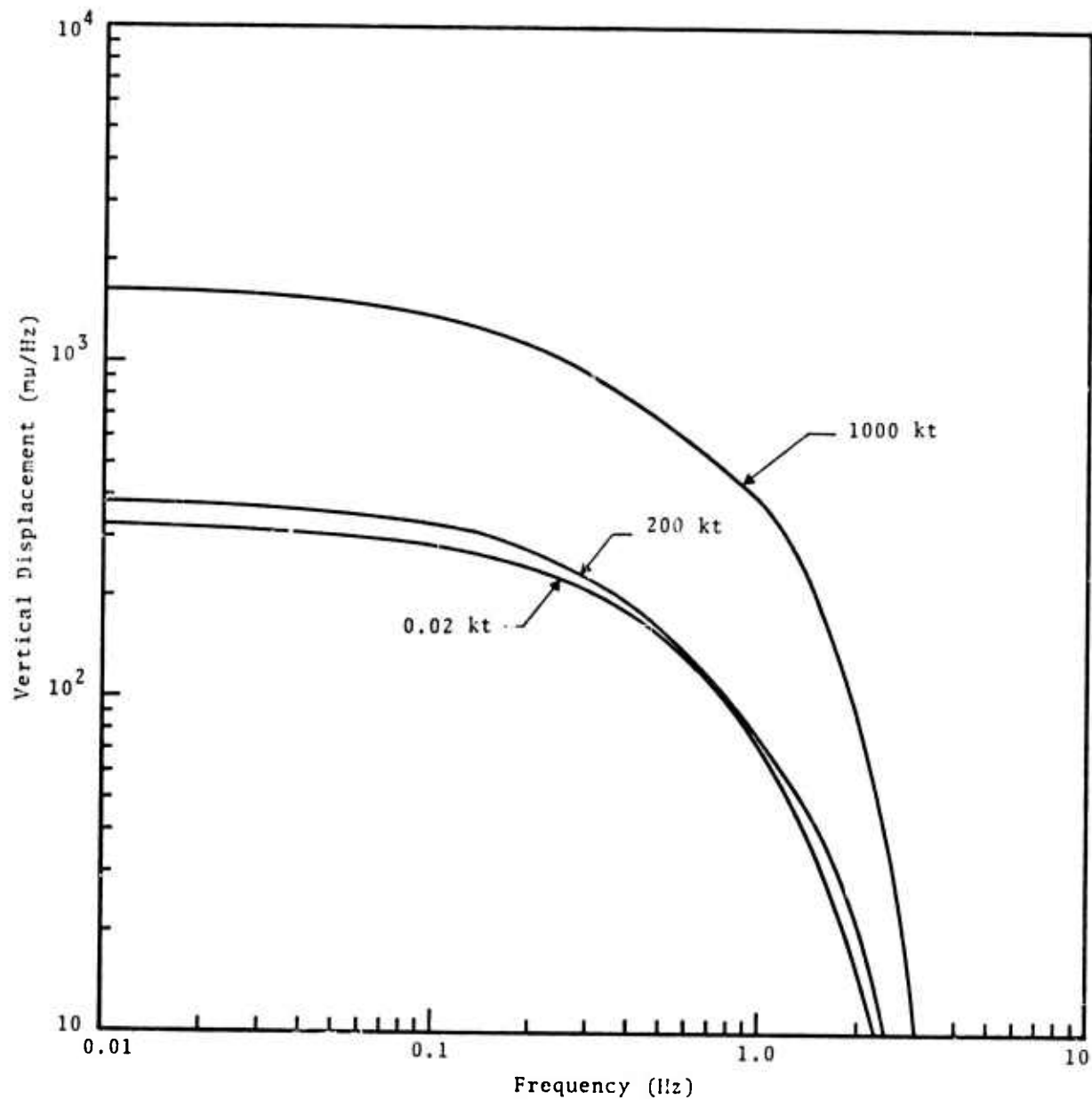
Fig. 4.29--Spectral amplitude of the direct P wave at 4066 km due to the source spectra of Fig. 4.27. The amplitudes for 0.02 kT have been multiplied by 10^4.

Scaling of m_b With Yield, W

In view of the above discussion, m_b versus log W curves are expected to have slope ≈ 1. Fixing all other parameters, the teleseismic records of the first mantle arrival due to three events of different yields are shown in Fig. 4.30. No differences in the pulse shapes for the three yields are apparent.

Figure 4.30d is essentially a plot of m_b versus log W. If, following Basham and Horner,[24] we were to define

$$m_b^* = m_b + \log T, \tag{4.10}$$

and plot m_b^* versus log W, we would obtain a parallel line. Although the source spectrum is quite different for the three yields (Fig. 4.27), only a slight deviation from unit slope is apparent in the plot. A linear fit to the data would have a slope of ≈ 0.975.

4.3.5 Tectonic Stress Release

Tectonic stress release is recognized as the most likely cause of the anomalous part of the radiation field from large underground explosions (e.g., Ref. [13-16]). The theory of stress wave radiation from explosions in prestressed media formulated by Archambeau[17] is used to compute the tectonic release contribution to the radiation field. Typical calculations including tectonic release effects were presented in Section 4.3.1, where it was observed that, in general, tectonic release does not affect m_b, but may have an appreciable effect on the observed wave form.

The tectonic release component of the source is specified in terms of a quadrupole point source. The important parameters controlling this source are the magnitude and orientation of the prestress and the radius (R_0) of the

113
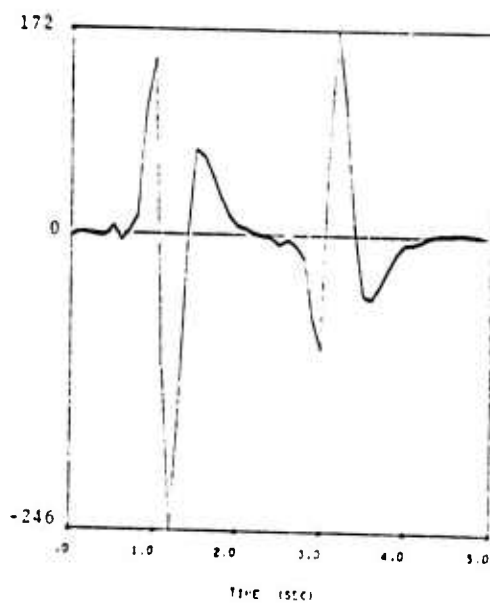
(a) W = 200kT. A_1 = 195mµ, T_1 = 0.5 sec.
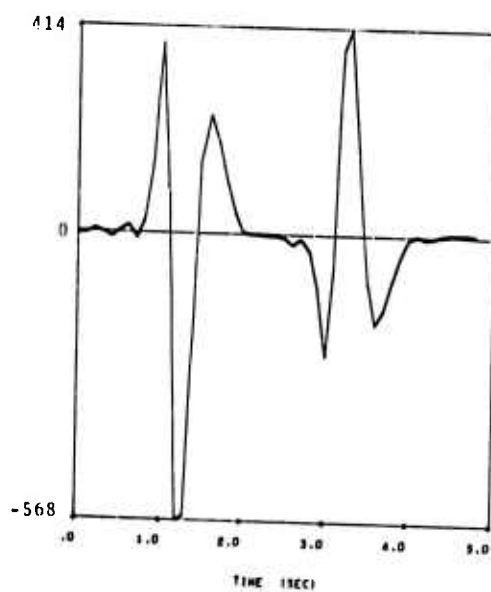
(b) W = 500 kT. A_1 = 485 mµ, T_1 = 0.5 sec.

Fig. 4.30--The effect of yield on m_b. Tuff source T-4, DOB = 2573 m, v_p^{ss}= 2.4 km/sec. Epicentral distance = 4066 km. Amplitudes are displayed in millimicrons.

Fig. 4.30 (Cont.)
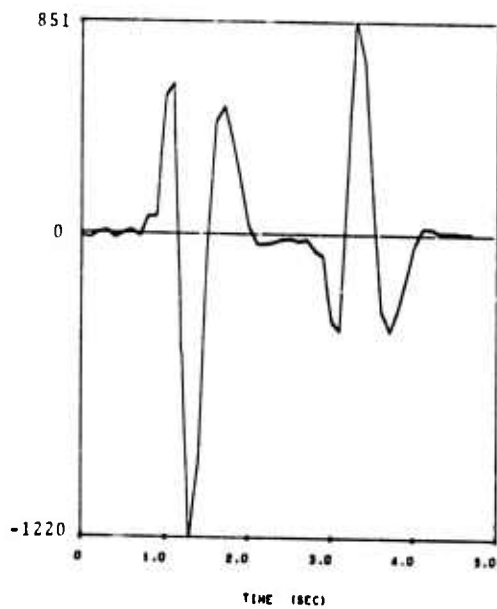
(c) W = 1000 kT. A_1 = 915 mµ, T_1 = 0.5 sec.
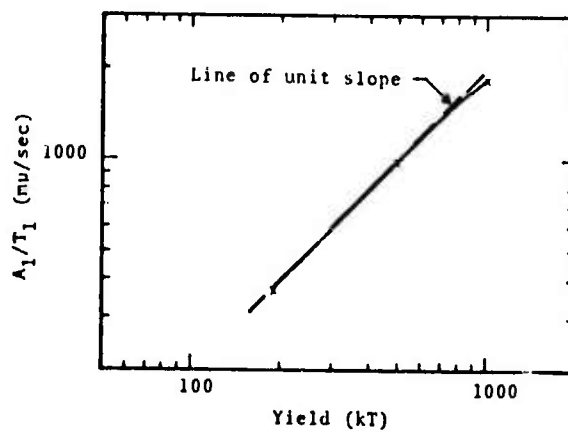
(d) Log (A_1/T_1) versus log W for the records (a) -
(c).

shatter zone created by the explosion shock wave. The displacement spectral amplitudes scale directly with the prestress and exhibit the azimuthal dependence characteristic of a quadrupole source. The amplitudes also scale with the cube of the shatter zone radius. Since R_{J} is expected to scale as $W^{1/3}$, the latter is equivalent to tectonic release amplitude scaling with yield.

Tectonic Release Effects on SPZ Records

The theory of tectonic stress release from explosions was developed to account for observations of anomalous shear wave radiation from large underground explosions. Most studies of this phenomenon are primarily concerned with surface waves; however, let us examine the possible contribution of tectonic release to measurements of short period vertical motion (SPZ). In Fig. 4.31 the true ground motion for the phases which make up the first mantle arrival from an explosion with tectonic release are shown, as well as the records of this motion from a Benioff short period instrument (see Fig. 4.7 for the instrument transfer function). The records are appropriate for an epicentral distance of 4066 km and an azimuth of 45 degrees. The conventions for defining prestress and source-to-receiver azimuth are shown in Fig. 4.32. From Fig. 4.31, note that the first P-wave motion from tectonic release is rarefaction, as expected. From symmetry, the records of Fig. 4.31 also apply for a prestress of σ_{12} = -160 bars and an azimuth of 225 degrees.

The effect of the LRSM SP instrument is clearly indicated in Fig. 4.31. It is interesting to note that for the simple direct P wave pulse from the explosion, the peak-to-peak amplitude on the instrument record is nearly the same as the peak true ground motion. The more complicated tectonic release wave forms do not exhibit this relationship,
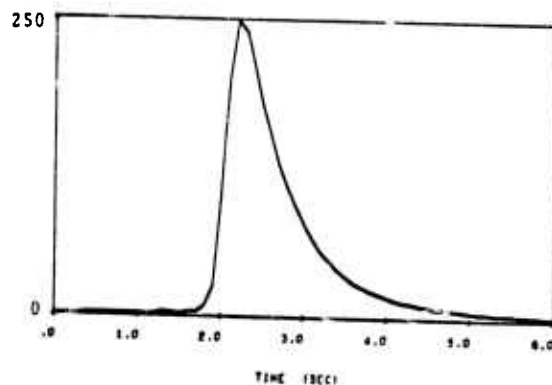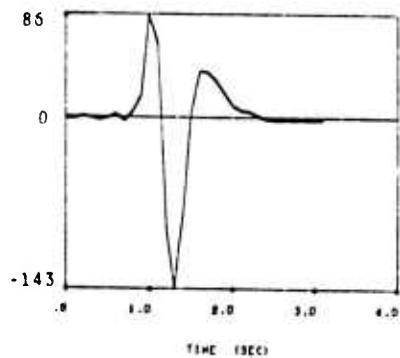
(a) Direct P wave from the explosion.
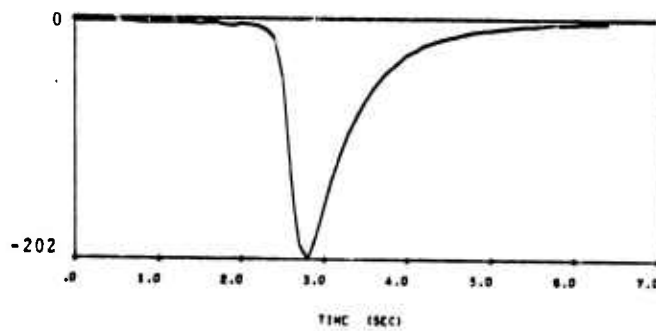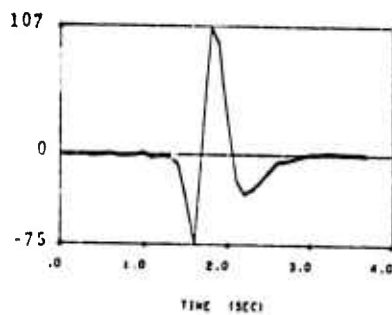
(b) Reflected P wave from the explosion.

Fig. 4.31--P wave phases at a distance of 2500 km and an azimuth of 45 degrees from a source consisting of an explosion plus tectonic release. Given are the true ground motion (right column) and seismometer output from LRSM SP instrument. (Explosion source T-4, yield = 200 kt, DOB = 700 m, R_0 = 600 m, prestress σ_{12} = 160 bars, earth structure CIT 109P 0.75Q.) The displacements are indicated in millimicrons.

117
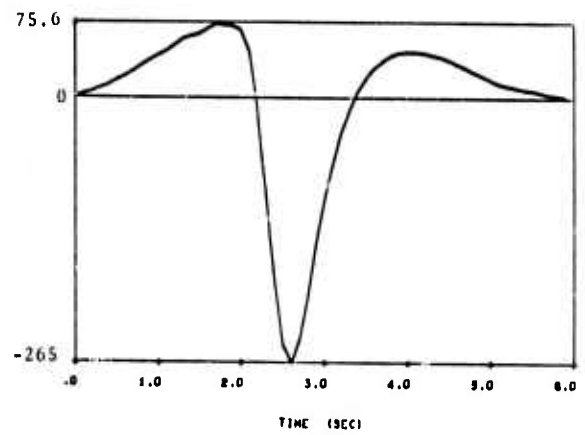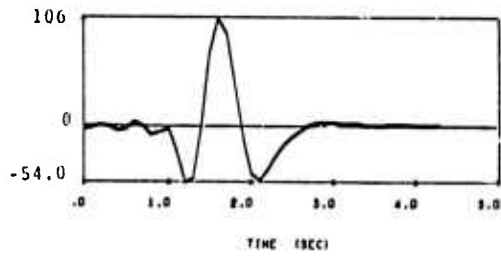
Fig. 4.31 (Cont.)

(c) Direct P wave from tectonic release.
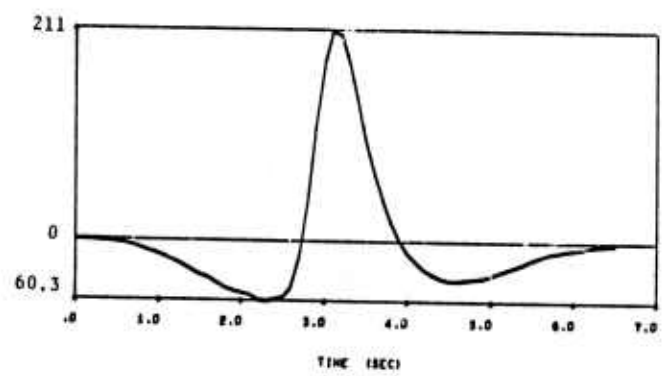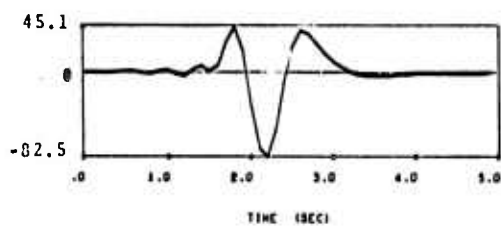
(d) Reflected P wave from tectonic release.

Fig. 4.31 (Cont.)
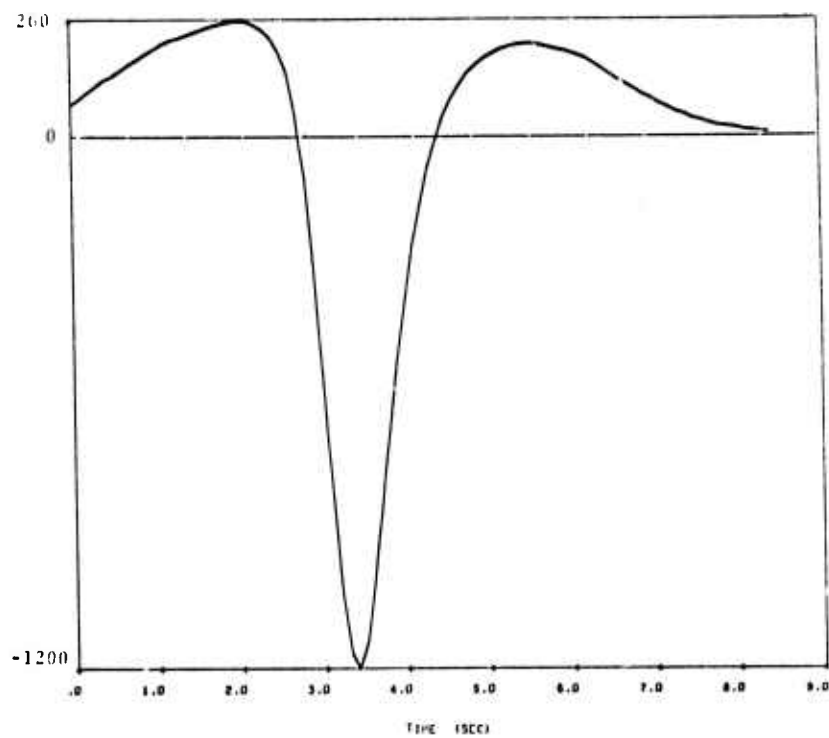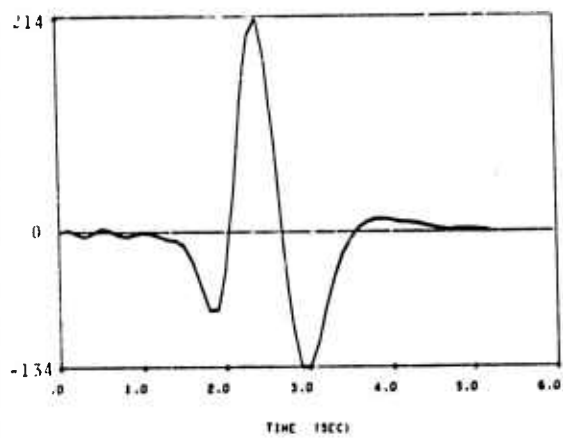
(e) Converted P wave from tectonic release.

Fig. 4.32 --Coordinate system for defining the prestress (arrows) and source-to-receiver azimuth (θ). The first motion in the four quadrants due to an explosion in a medium with prestress $\sigma_{12} > 0$ is also indicated. Definitions of σ_{13} and σ_{23} are consistant with that of σ_{12}.

due mainly to the instrument filtering of the long period components of these pulses. The long period lobes on the tectonic release ground motion records (caused by finite R_s, see Fig. 4.4 and Section 4.3.1) have little effect on the seismograph records.

For the event of Fig. 4.31, the tectonic P wave is of the same order as the explosion P wave and the tectonic sP_T is the largest phase of all. This is due to the rather large prestress and crush zone radius selected, as well as the station orientation with respect to the prestress (radiation pattern effect). The effect of this large tectonic release component is ascertained by comparing first mantle arrival records with and without tectonic release. In Fig. 4.33 the total first arrival record (from the LRSM SP instrument) including only explosion effects is shown as well as the total record with both explosion and tectonic release phases included. In Table 4.3 the m_b values for the two records are compared (the distance correction for 2500 km is taken to be 3.25).

TABLE 4.3

COMPARISON OF m_b FOR THE RECORDS OF FIGURE 4.33

Seismogram	$m_b^{(1)}$	$m_b^{(2)}$
4.33a (no tectonic release)	5.62	5.45
4.33b (with tectonic release)	5.69	5.55

Clearly, tectonic release has little effect on m_b for this example. However, comparing the two records, tectonic
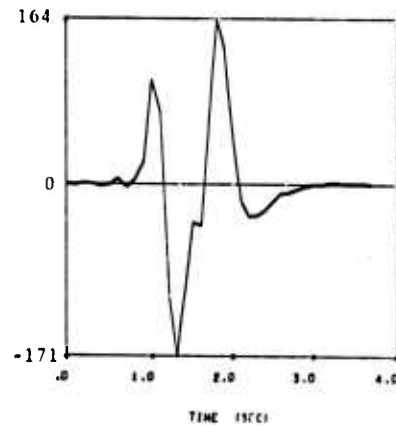
(a) First mantle arrival with no tectonic release: sum of phases 4.31(a)-(b). $A_1 = 139$, $T_1 = 0.6$, $A_2 = 167$, $T_2 = 1.05$.
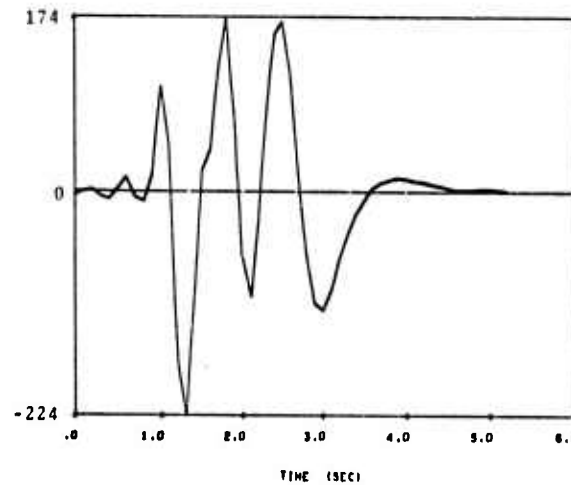
(b) First mantle arrival including tectonic release; sum of phases 4.31(a)-(e). $A_1 = 165$, $T_1 = 0.6$, $A_2 = 199$, $T_2 = 1$.

Fig. 4.33--Comparison of P wave first mantle arrival records for the event of Fig. 4.31, with and without tectonic release. The first three mantle arrivals as recorded at 2500 km are shown in part (c). All displacements are indicated in millimicrons.

Fig. 4.33 (Cont.)
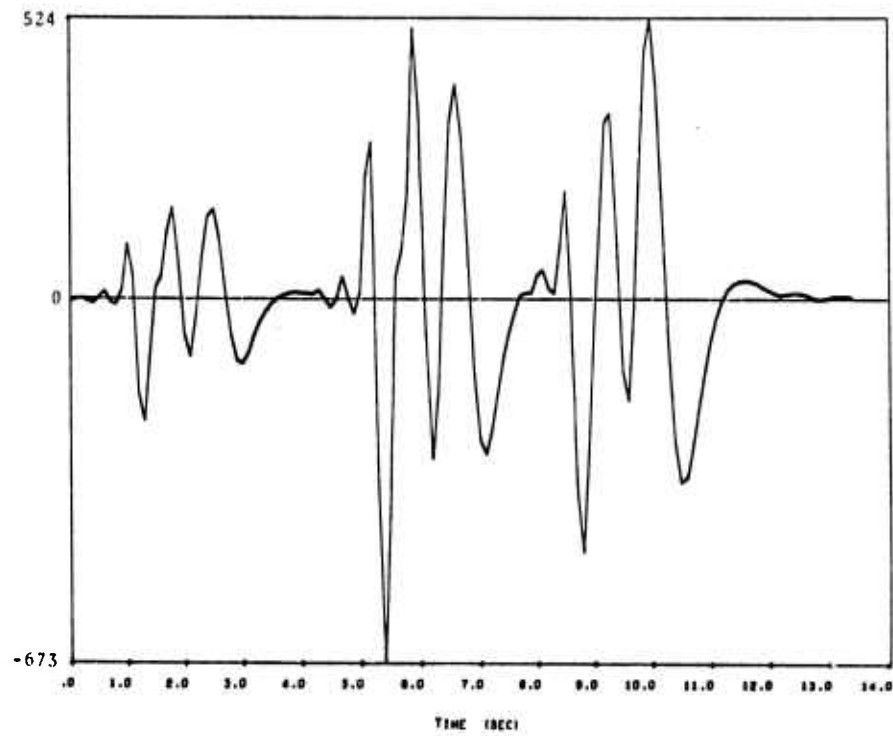
(c) First three mantle arrivals, including tectonic release.

release does add considerable complexity, especially via the large and late arriving sP_T phase.

In Fig. 4.33c the complete record of the first three P wave mantle arrivals is shown. At this distance, 2500 km, the first mantle arrival is unusually small compared to later arrivals. This suggests another source of difficulty in choosing m_b, especially for low yield events, in that a later arriving phase might be selected for computation of m_b.

4.4   THE DEPENDENCE OF m_b ON EARTH STRUCTURE AND THE SOURCE ENVIRONMENT

4.4.1   General Remarks

In previous sections we have seen how the various parameters characterizing an explosion event influence teleseismic amplitude measurements. These parameters include material properties in the source vicinity (determining the explosion and tectonic release spectra), the depth of burial, the yield, and the velocity and attenuation (Q) properties of the earth structure between source and receiver. Using this information, we proceed to study a series of events in tuff, granite and sandstone media.

4.4.2   Underground Explosions in NTS Tuff

All calculations presented in Section 4.3 pertained to NTS tuff. Reference was previously made to such tuff events as Bilby and Handley, with which our computational procedure gave excellent agreement. It has been postulated that significant amounts of tectonic stress release accompanied many of the tuff events. However, it was learned in Section 4.3.5 that tectonic release has little effect on the first two cycles of the teleseismic record, the region in which our m_b measurements are made. Therefore, for simplicity, let us

124

assume no tectonic release component and construct synthetic seismograms for several events in NTS tuff.

Bilby

This much studied event was the source of the data on which the earth structure model, CIT 109, used in this report was constructed.[23] The event was a 200 kt explosion in NTS tuff at a depth of burial of 700 m. Synthetic seismograms applicable to Bilby have been presented in Figs. 4.11, 4.12, 4.13, 4.21, 4.25b, 4.26b, and 4.33. The m_b results from these figures are summarized in Table 4.4. The LRSM assigned m_b for Bilby was 5.8; hence, the values of the table show good agreement with the observed.

Before directing our attention to other tuff events, we calculate synthetic seismograms for the Bilby event at a series of epicentral distances. These are shown in Fig. 4.34. In Fig. 4.35 the maximum amplitudes, A_1 and A_2 of Fig. 4.34, are plotted versus epicentral distance. Also shown are the amplitudes of the "principal phases" as recorded by the LRSM network.[25] These observed amplitudes should be the maximum amplitudes recorded during the first few cycles of motion. Considering the wide scatter of this data, our agreement seems quite satisfactory.

The m_b values for the synthetic seismograms of Fig. 4.34 are summarized in Table 4.5. Once again, our calculated values show excellent agreement with the observed m_b of 5.8. Recall that $m_b^{(2)}$ is that which likely corresponds to the LRSM value, while $m_b^{(1)}$ reflects most accurately the explosion yield (relatively unaffected by DOB) and is given for reference.

Finally, note that the variation of m_b with distance in Table 4.5 simply reflects an incompatibility of our earth structure model with the LRSM distance correction factors.
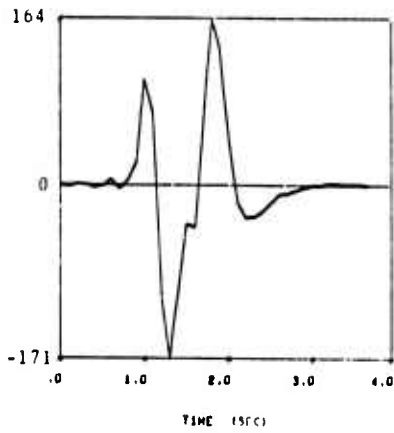
(a) 2500 km. $A_1 = 139$, $T_1 = 0.6$, $A_2 = 167$, $T_2 = 1.05$.
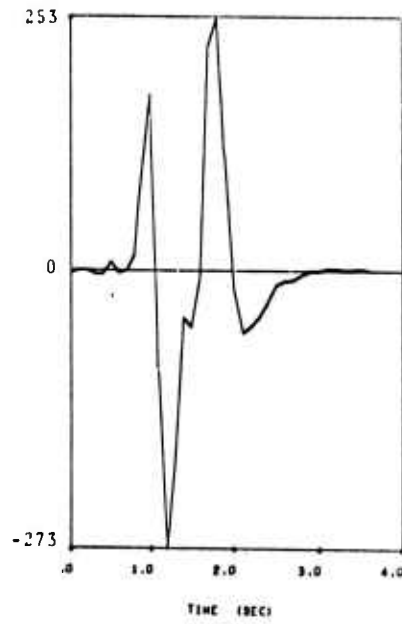
(c) 3500 km. $A_1 = 225$, $T_1 = 0.5$, $A_2 = 263$, $T_2 = 1.1$.
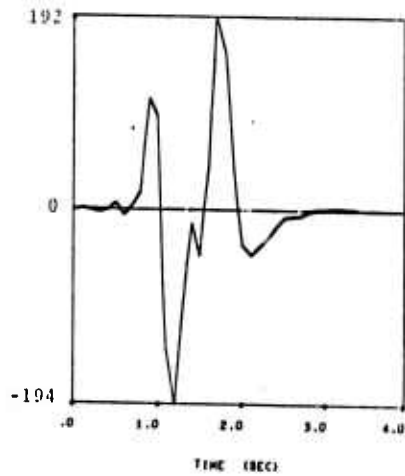
(b) 3000 km. $A_1 = 152$, $T_1 = 0.55$, $A_2 = 193$, $T_2 = 1.05$.
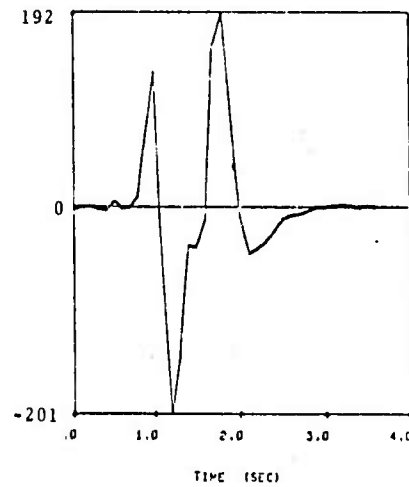
(d) 4066 km. $A_1 = 168$, $T_1 = 0.5$, $A_2 = 195$, $T_2 = 1.1$.

Fig. 4.34--Synthetic seismograms for Bilby at a series of epicentral distances. Source 13B, Yield 200 kt, DOB 700 meters, earth structure CIT 109P 0.75 Q.

Fig. 4.34 (Cont.)
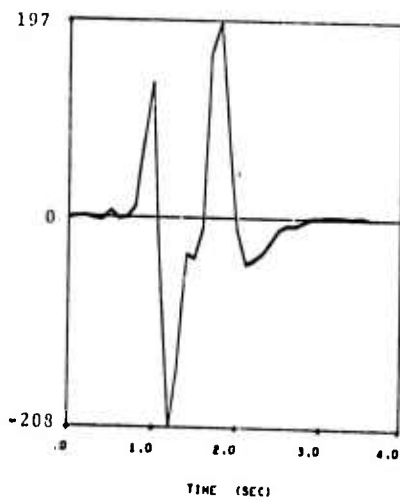
(e) 4500 km. $A_1 = 173$, $T_1 = 0.5$, $A_2 = 202$, $T_2^1 = 1.1$.

(f) 5000 km. $A_1 = 220$, $T_1 = 0.5$, $A_2^1 = 253$, $T_2^1 = 1.15$.

TABLE 4.4

BILBY m_b FROM VARIOUS MODELS OF SECTION 4.5

Figure	Source	Q Model	Epicentral Distance	$m_b^{(1)}$	$m_b^{(2)}$
4.11	T-3	Low Q	4066 km	5.65	---
4.21a	T-4	High Q	4066 km	6.03	5.91
4.21b	T-4	0.75 Q	4066 km	6.07	5.79
4.21c	T-4	Low Q	4066 km	5.40	5.34
4.33a	T-4	0.75 Q	2500 km	5.62	5.45
4.33b	T-4*	0.75 Q	2500 km	5.69	5.55

* Including tectonic release
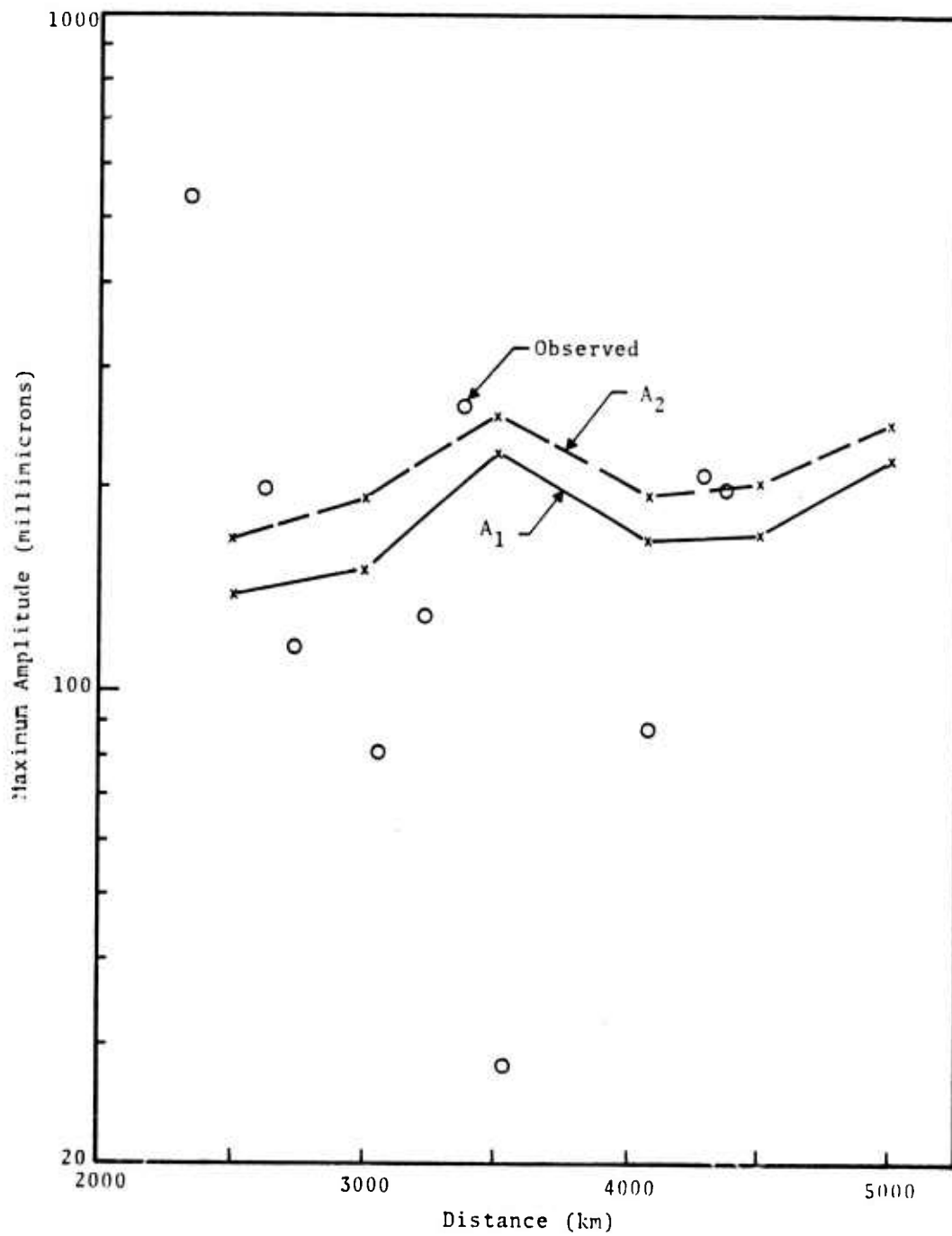
Fig. 4.35--Maximum amplitude versus epicentral distance for the Bilby event. Amplitudes from the synthetic seismograms of Fig. 4.34 are compared to LRSM observed values.

TABLE 4.5

BILBY m_b AT VARIOUS DISTANCES

Epicentral Distance	Distance Factor*	$m_b^{(1)}$	$m_b^{(2)}$
2500	3.25	5.61	5.45
3000	3.50	5.94	5.76
3500	3.70	6.35	6.07
4066	3.54	6.07	5.79
4500	3.45	5.99	5.71
5000	3.70	6.34	6.04

* Taken from the table of distance factors appearing in LRSM shot reports (e.g., [25])

Improvements to our model and/or the distance factor table are necessary to remove this incompatability.

Knickerbocker, Greeley, Benham

Synthetic seismograms for three NTS tuff events of widely differing yields are shown in Fig. 4.36. These events, Knickerbocker, Greeley and Benham, were detonated at virtually the same location at depths of burial dependent on yield.[8,24] The synthetic seismograms were constructed for an epicentral distance of 3000 km using the earth structure model CIT 109P 0.75 Q and the SKIPPER Source T-4.

The Knickerbocker event, like Bilby detonated at a depth sufficiently shallow to allow interference between P and pP, gives a seismogram for which $m_b^{(2)}$ seems most comparable to LRSM values. However, for the two larger events, P and pP arrive separately and no large second cycle appears on the records.

The m_b values for these three events are summarized in Table 4.6. Also shown is m_b^* defined from the maximum amplitude on the record (4.10), along with average m_b^* values from the Canadian Seismograph Network given by Basham and Horner.[24] Once again, our computed m_b values agree quite well with the observed.

In Fig. 4.37 the teleseismic data for the four tuff events studied in this section is plotted versus yield. The slope of the lines connecting adjacent events is also indicated on the figure and should be compared with the analogous data (Fig. 4.30) with depth of burial effects removed. Comparing plots 4.37(a) and (b), we see a clear indication of the sensitivity of m_b to the measurement period. This period is quite difficult to measure accurately on our synthetic seismogram and is expected to introduce a random error.
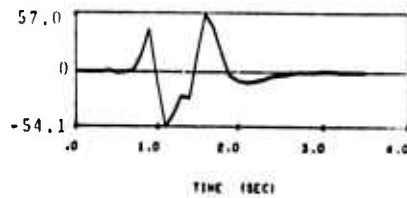
(a) Knickerbocker (71 kt at 630 m). $A_1 = 48$, $T_1 = 0.45$, $A_2 = 56$, $T_2 = 1.0$.
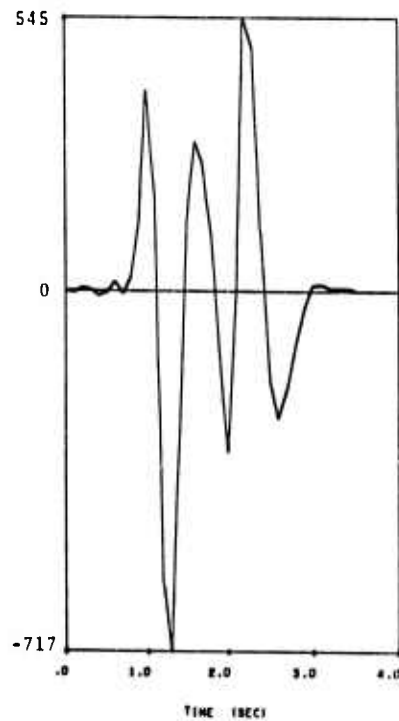
(b) Greeley (825 kt at 1214 m). $A_1 = 560$, $T_1 = 0.6$.

Fig. 4.36--First mantle arrival synthetic seismograms for the Knickerbocker, Greeley and Benham events in NTS tuff. Epicentral distance 3000 km, Source T-4, earth structure model CIT 109P 0.75 Q.
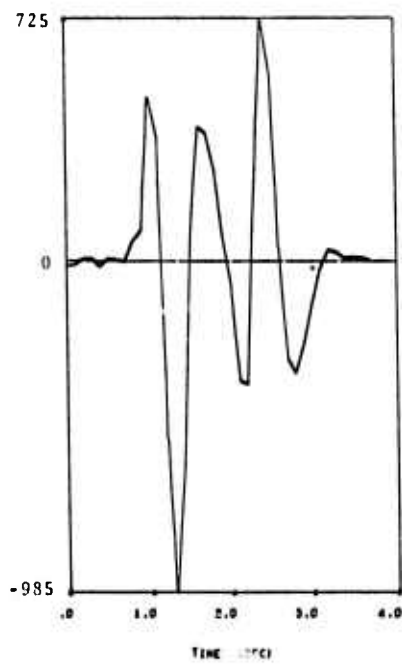
(c) Benham (1100 kt at 1402 m). $A_1 = 745$, $T_1 = 0.6$.

Fig. 4.36 (Cont.)

TABLE 4.6

m_b FOR SELECTED NTS TUFF EVENTS

Event	Yield	DOB	Observed m_b^*	m_b^*	$m_b^{(1)}$	$m_b^{(2)}$
Knickerbocker	75 kt	630 m	4.95	5.25	5.53	5.25
Greeley	825 kt	1214 m	6.01	6.25	6.47	--
Benham	1100 kt	1402 m	6.37	6.37	6.59	--
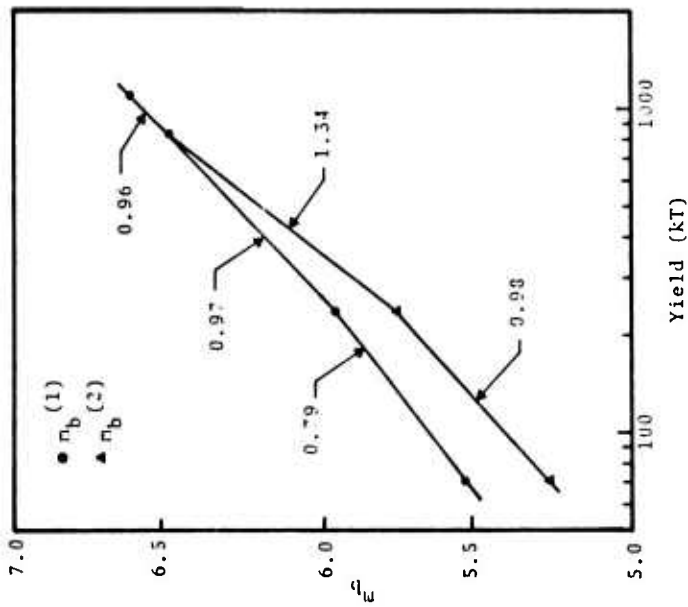
(a) m_b versus yield
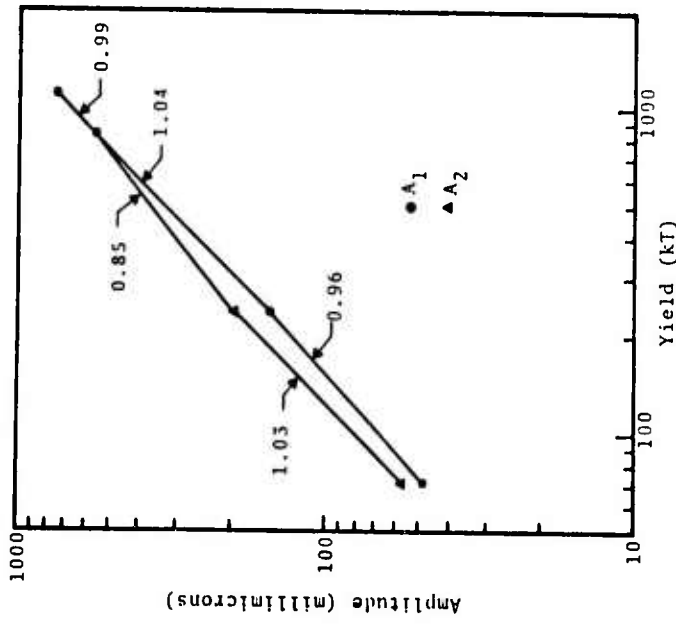
(b) Amplitude versus yield

Fig. 4.37--Comparison of m_b and maximum amplitude versus yield for four explosions in NTS tuff. The slope of the linear segment connecting various events is also indicated.

135

For shallow explosions the effect of small changes in DOB is significant because it affects the measurement period. This accounts for the seemingly anomalous slope of 0.79 on 4.37a. For deeper events, DOB becomes insignificant for m_b measurements.

As a final observation, m_b data from a series of different yields, and thus different burial depths, may include data obtained from different cycles for different events. Thus, caution must be exercised when plotting m_b versus log yield. For example, using the maximum cycle on the records of Fig. 4.36 (as suggested for the LRSM network) results in an anomalous bend in the m_b versus log W or m_b^* versus log W curve (Fig. 4.37).

4.4.3 Underground Explosions in Sandstone

Several nuclear explosions in sandstone have been detonated in western Colorado. In this section, computations applicable to two of these events, Rulison and Rio Blanco, will be presented.

Rulison

Rulison was a gas stimulation explosion of 40 kt detonated at a burial depth of 2573 m. The source function calculation for Rulison was described in Section II. The amplitude of the RVP transform from this calculation is shown in Fig. 4.38. It is seen that the source spectrum is nearly flat in the region (< 3 Hz) which influences the teleseismic signal.

In Fig. 4.39 synthetic seismograms constructed for Rulison at an epicentral distance of 2500 km are presented. The record of Fig. 4.39b is from a calculation including a rather large tectonic release component and is included to illustrate the possible effect of tectonic release on a
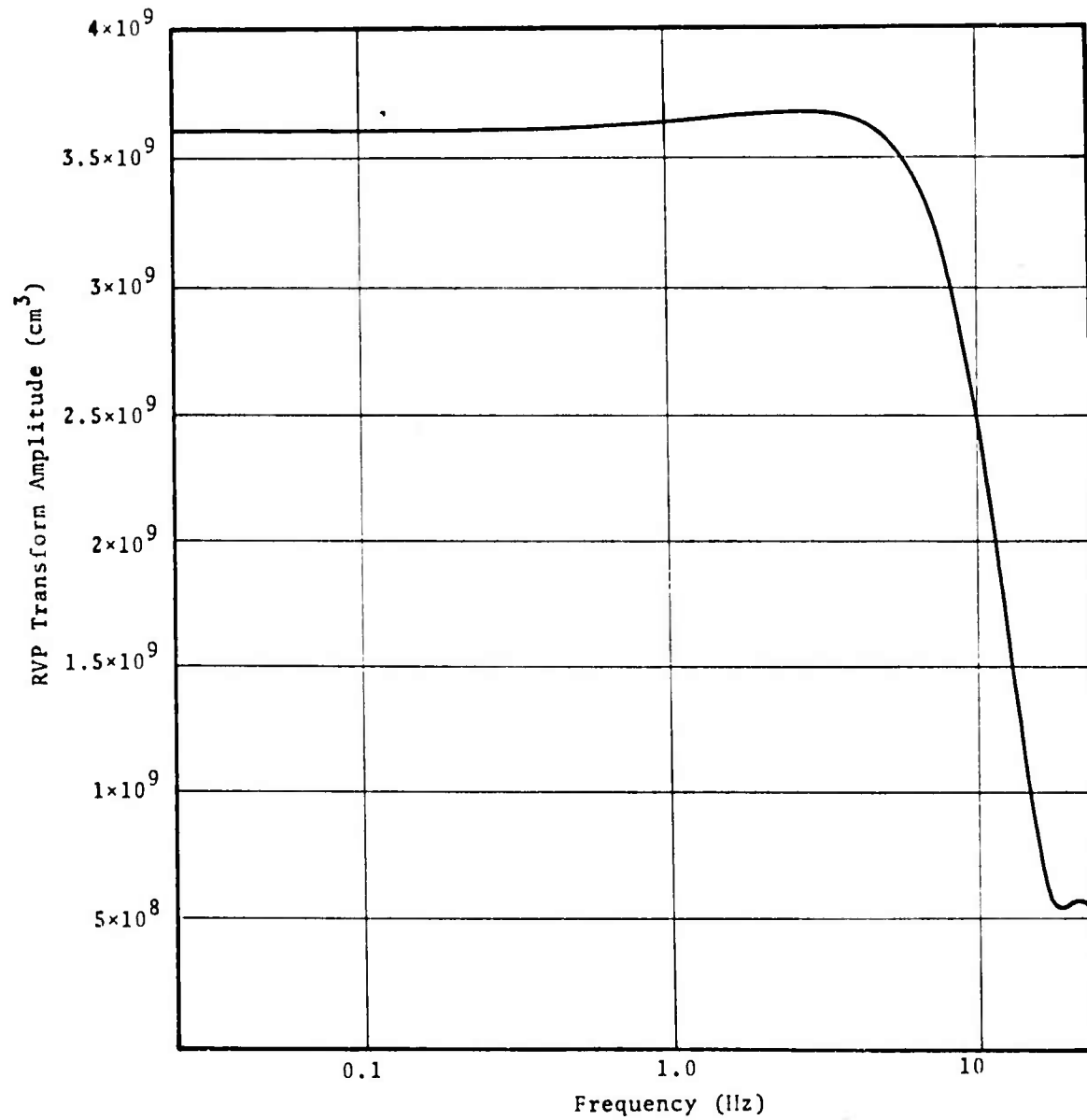
Fig. 4.38--Reduced velocity transform amplitude versus frequency for Rulison, 40 kt in sandstone at a depth of 2573 meters.
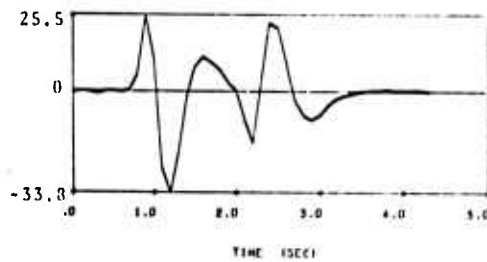
(a) First mantle arrival (no tectonic release). $A_1 = 30$, $T_1 = 0.6$.
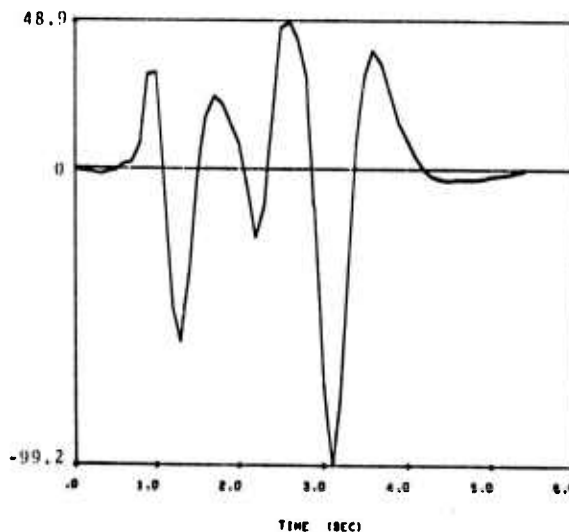
(b) First mantle arrival including tectonic release (shatter zone radius $R_0 = 400$ m, prestress $\sigma_{12} = 256$ bars). $A_1 = 46$, $T_1 = 0.7$, $A_3 = 74$, $T_3 = 1.1$.

Fig. 4.39--First mantle arrival for the Rulison explosion with and without tectonic release. Epicentral distance 2500 km, SKIPPER Source S-2, earth structure model CIT 109P 0.75 Q, source-to-surface velocities assumed identical to velocities in the source region.

very deep event. The cycle of maximum amplitude for this record is the third.

The computed m_b and m_b^* values for Rulison are compared to average observed values given by Lambert and Ahner[26] and Basham and Horner[24] in Table 4.7.

The agreement of computed and observed m_b^*; that is, the maximum amplitude appearing on the record, is excellent for the explosion without the tectonic component. The poorer agreement of m_b values then seems to be due to the relatively short periods of the cycles from which our m_b measurements are made. This is believed to be a consequence of our earth structure model, but indicates an area which warrants further investigation.

The tectonic release component in Fig. 4.39b seems too high for the Rulison explosion, but represents a not im-plausible event for a tectonically stressed sandstone region.

Rio Blanco

For Rio Blanco three 30 kt devices were simultaneously detonated in a vertical hole at depths of 1780, 1900 and 2040 meters. The SKIPPER source S-1 was calculated for a depth intermediate to the three, giving the $|\hat{\psi}|$ shown in Fig. 4.40. The amplitude scales on this figure are appropriate to a yield of 30 kt while frequency scales for both 30 and 90 kt are shown.

Ignoring depth effects, which are expected to be small, two ways of treating this event are suggested. First, we could compute the teleseismic signal due to a 30 kt explosion and multiply the far field signal by three. Second, we could treat the event as a single 90 kt explosion. Examining Fig. 4.40, it is apparent that the two approaches are equivalent due to the flat character of the spectrum.

TABLE 4.7

m_b DATA FOR RULISON

Seismogram	Observed m_b	Observed m_b^*	m_b^*	$m_b^{(1)}$	$m_b^{(3)}$
4.39a (no tectonic release)	4.62	4.78	4.73	4.95	--
4.39b (with tectonic			5.12	5.07	5.07
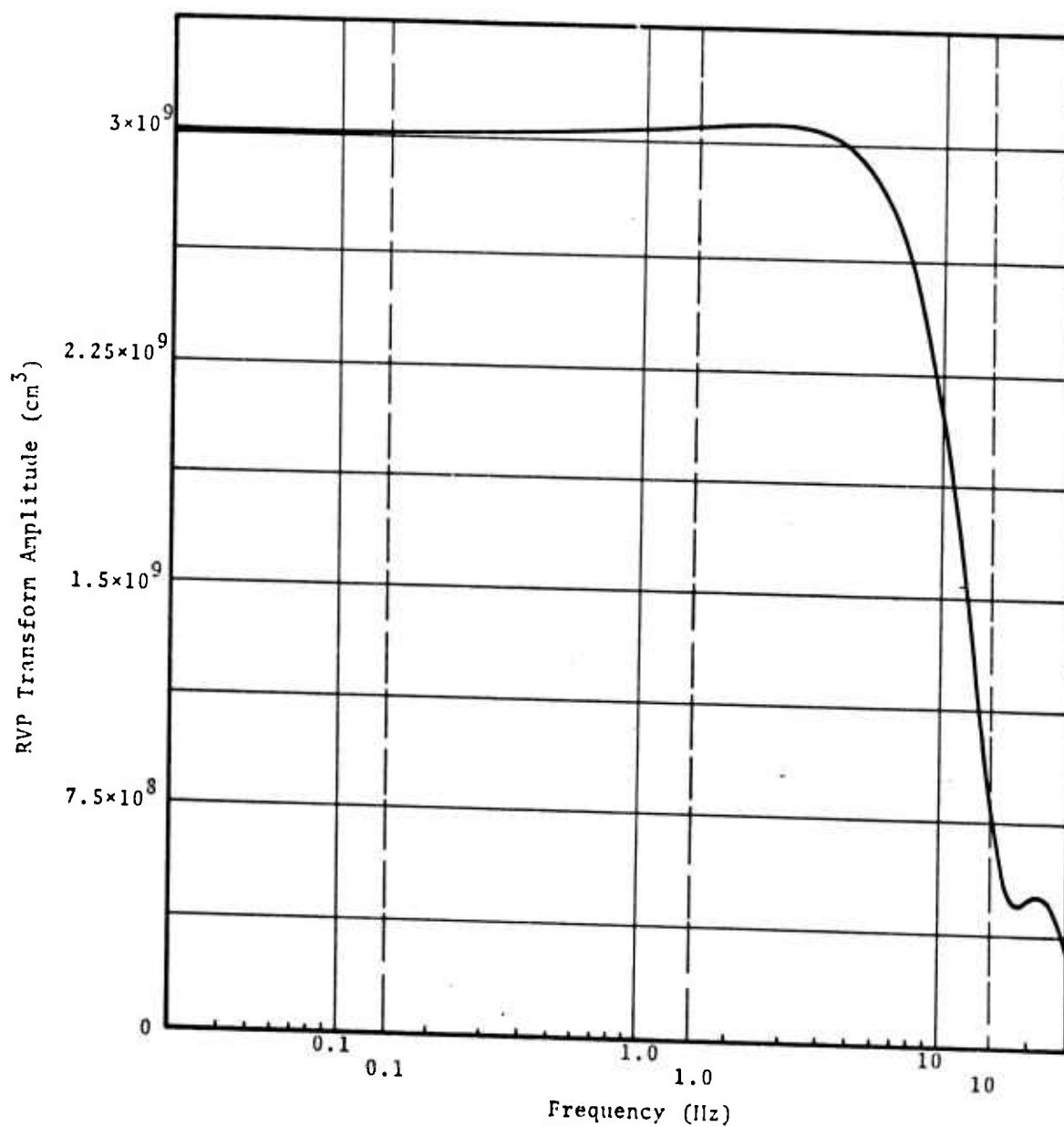
Fig. 4.40--Reduced velocity potential transform amplitude
versus frequency for Rio Blanco, three simultaneously de-
tonated 30 kt explosions in sandstone at a mean depth of
1900 meters. Solid grid lines are for a single 30 kt
explosion, while the dashed time scales represent scaling
for 90 kt.

The first mantle arrival portion of a synthetic seismogram for Rio Blanco is shown in Fig. 4.41. The cycle of maximum amplitude on the record is the first which is influenced only the the direct P wave from the explosion. For this computation the body wave magnitudes are

$$m_b = 5.51,$$

$$m_b^* = 5.29.$$

(4.11)

4.4.4 Underground Explosions in Granite

This section includes an investigation of the teleseismic signature of explosions in granite. One specific event, Piledriver, is modeled along with a study of magnitude versus yield and tectonic release effects.

Source Functions

The calculation of source functions for explosions in granite is discussed in Section II, where two SKIPPER calculations giving markedly different results were presented. The amplitudes of the RVP transforms for the two source functions are shown in Fig. 4.42.

Piledriver

The Piledriver event was a 61 kt explosion at a depth of 463 meters in NTS granite. Synthetic seismograms using both source functions G-1 and G-2 are presented in Fig. 4.43. These seismograms show the first mantle arrival at an epicentral distance of 3000 km. The shallow depth of burial and high local wave velocity (5.6 km/sec) cause P and pP to arrive almost simultaneously with a lag of $\approx$ 0.17 seconds.

TIME (SEC)
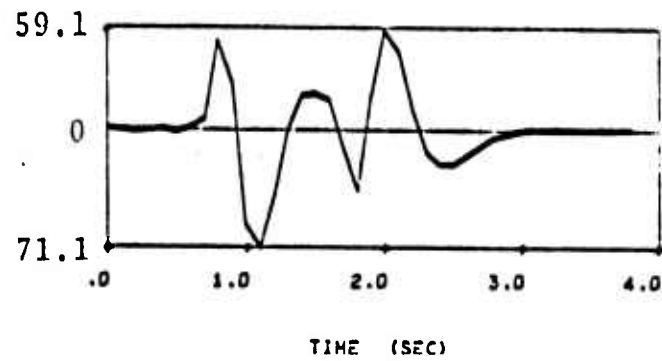
Fig. 4.41--First mantle arrival for Rio Blanco. Epicentral
distance 3000 km, source S-1, earth structure model CIT 109P
0.75 Q. $A_1 = 62$, $T_1 = 0.6$.
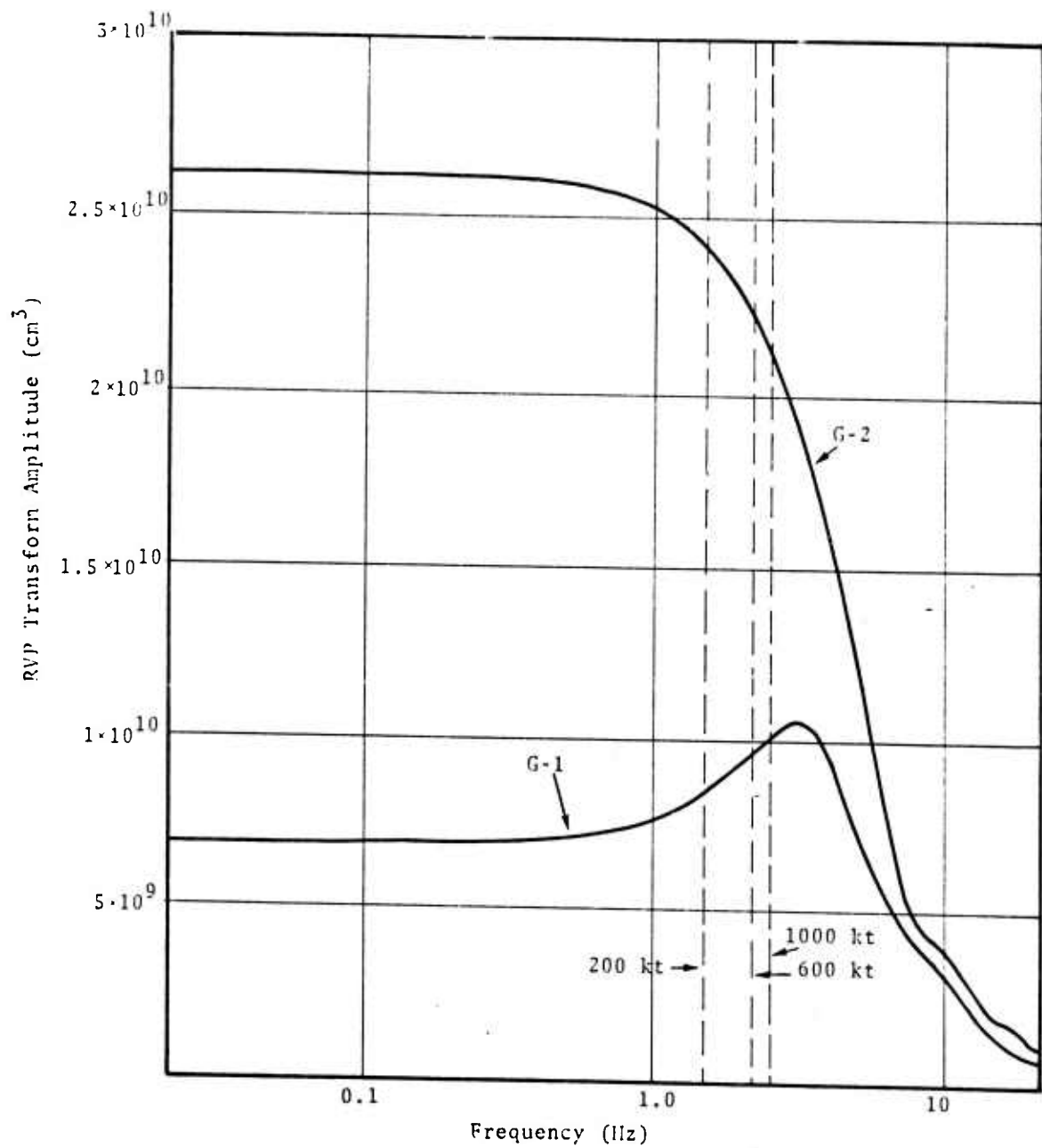
Fig. 4.42--Reduced velocity potential transform amplitude versus frequency for granite source functions G-1 and G-2, scaled to 61 kt. Also shown are the 1 Hz frequency points for 200, 600, and 1000 kt.
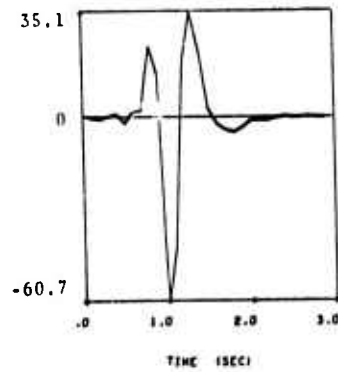
(a) Source G-1. A_1 = 42, T_1 = 0.4, A_2 = 48, T_2 = 0.6.
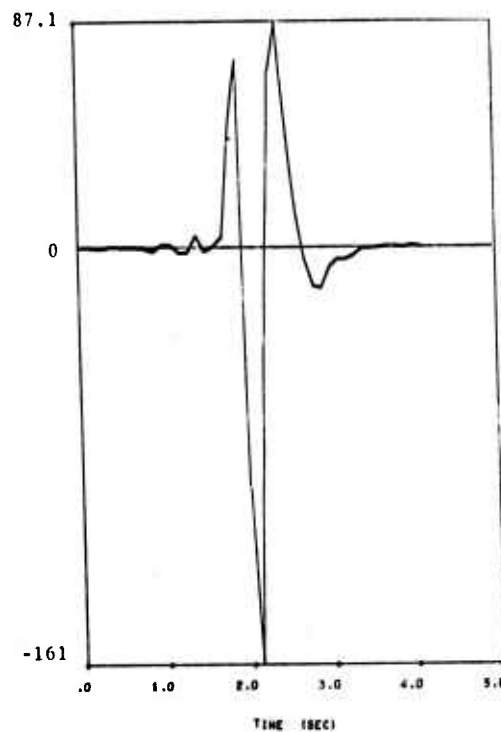
(b) Source G-2. A_1 = 118, T_1 = 0.4, A_2 = 124, T_2 = 0.6.

Fig. 4.43--First mantle arrival synthetic seismograms for Pile-driver using two source functions. Yield 61 kt, DOB 463 m, epicentral distance 3000 km, earth structure model CIT 109P 0.75 Q.

TABLE 4.8

COMPARISON OF OBSERVED AND COMPUTED
m_b FOR PILEDRIVER

Seismogram	Observed[+] m_b	Observed[‡] m_b^*	m_b^*	$m_b^{(1)}$	$m_b^{(2)}$
4.43b (G-1)	5.53	5.46	5.59	5.97	5.82
4.43a (G-2)			5.18	5.52	5.40

[+]Average value from LRSM Shot Report[19]

[‡]Average value from Basham and Horner[24]

The body wave magnitudes for this event are summarized in Table 4.8.

The magnitudes measured on the first cycle, $m_b^{(1)}$, do not relate to observations and are given only for comparison with previous sections. The synthetic seismograms are quite similar in shape to the first two cycles of the actual records[19] and $m_b^{(2)}$ is almost certainly directly comparable to the LRSM m_b.

As was the case for the sandstone event Rulison, the maximum amplitude on our computed records (i.e., m_b^*) shows good agreement with the observed. However, once again the period of the measured cycle is somewhat smaller than the periods on the actual records.

Comparing the two theoretical records, note that substantial differences in source spectral shape have little influence on the shape of the teleseismic pulse. The combined filters of the earth structure and seismograph have too narrow a pass band to see much source spectral variation. The absolute amplitude of the source spectrum in the 0.3 to 1 Hz range is, of course, directly reflected in the amplitude of the teleseismic pulse.

Magnitude Versus Yield for Granite

In Fig. 4.44, synthetic seismograms for explosions of 200, 600 and 1000 kt in granite are shown along with a plot of magnitude versus yield. The changing shape of the source function G-2 for each yield is indicated on Fig. 4.42. All three events are at the same depth, so the complicating effect of the usual functional relationship between yield and DOB is removed. Despite the source spectrum differences, the slope of the resulting magnitude versus log yield plot (Fig. 4.44d) is very close to unity, certainly within the accuracy of our measurements.
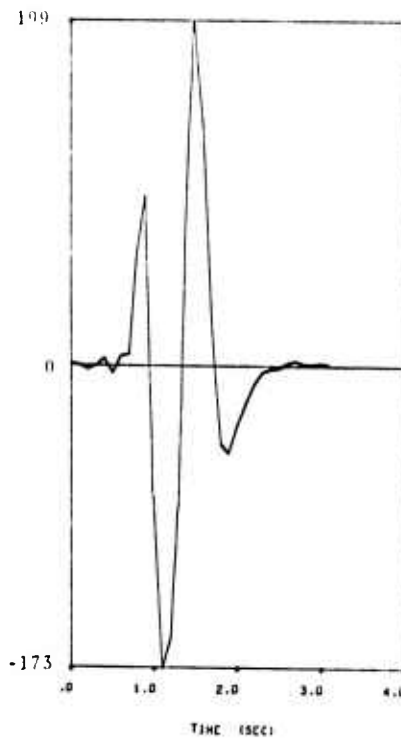
(a) 200 kt. $A_2 = 186$, $T_2 = 0.75$.
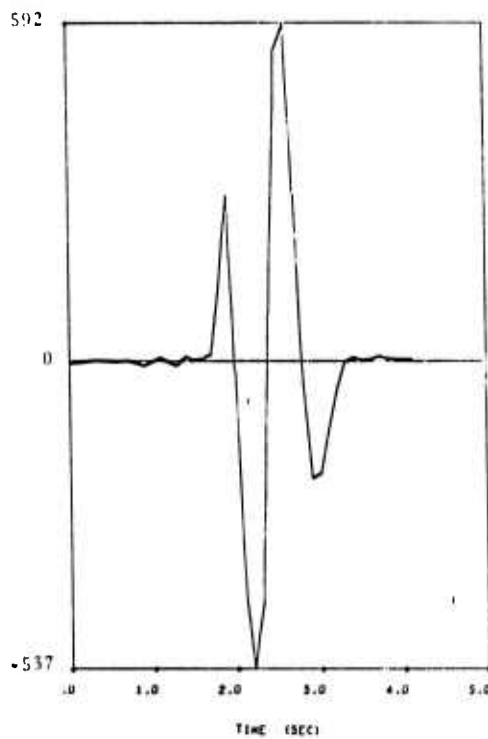
(b) 600 kt. $A_2 = 564$, $T_2 = 0.75$.

Fig. 4.44--First mantle arrival synthetic seismograms for three explosions in granite. Source G-2, DOB 1200 m, epicentral distance 3000 km, earth structure model CIT 109P 0.75 Q.

Fig. 4.44 (Cont.)
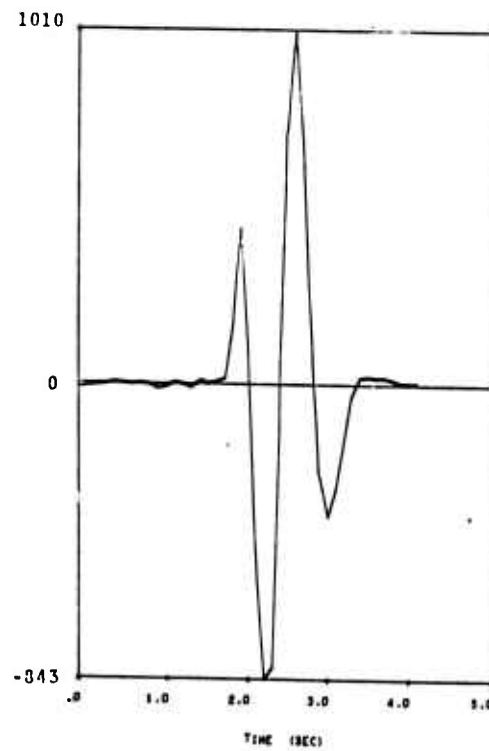
(c) 1000 kt. $A_2 = 920$, $T_2 = 0.75$.
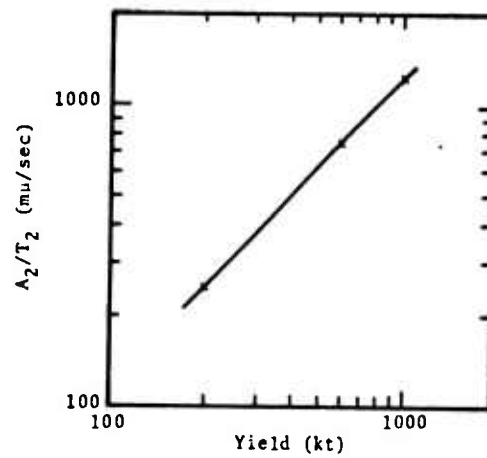
(d) Magnitude versus yield for (a)-(c).

Granite Calculations Including Tectonic Stress Release

The Piledriver event was characterized by a substantial amount of anomalous shear radiation. The effect of a rather large tectonic release component on short period body waves from Piledriver is presented in Fig. 4.45 for both granite source functions. Assuming the tectonic prestress to be aligned along a north-south axis, as is typical of NTS, the chosen azimuth corresponds to stations in the northeastern U.S. and adjacent areas of Canada.

Even for this large tectonic release component (the converted sP_T is of the same order as direct P from the explosion), the effect on SPZ records is minimal. The measured magnitudes, summarized in Table 4.9, are seen to be little different than the corresponding values (Table 4.8) for the calculation with no tectonic release.

4.4.5 Summary of Body Wave Magnitudes--Comparison to Observed

The body wave magnitudes from our synthetic seismograms are compared to observed values in graphical form in Fig. 4.46. The computed values are all from computations using the earth structure model CIT 109P 0.75 Q. The source function T-4 was used for all tuff calculations. The values for Knickerbocker, Greeley and Benham are from Table 4.6. The Rulison value is from Table 4.7. For Piledriver and Bilby a range of computed values is indicated. For Piledriver this represents the range of values from the two source functions G-1 and G-2, with and without tectonic release (Tables 4.8 and 4.9). For Bilby the $m_b^{(2)}$ values are taken from Table 4.5 which gives Bilby m_b values at various teleseismic distances.
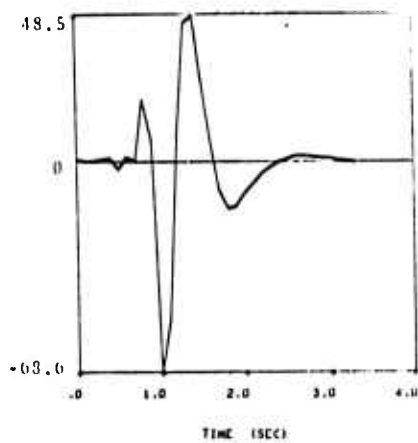
(a) Source G-1. $A_1 = 45$, $T_1 = 0.4$, $A_2 = 58$, $T_2 = 0.7$.
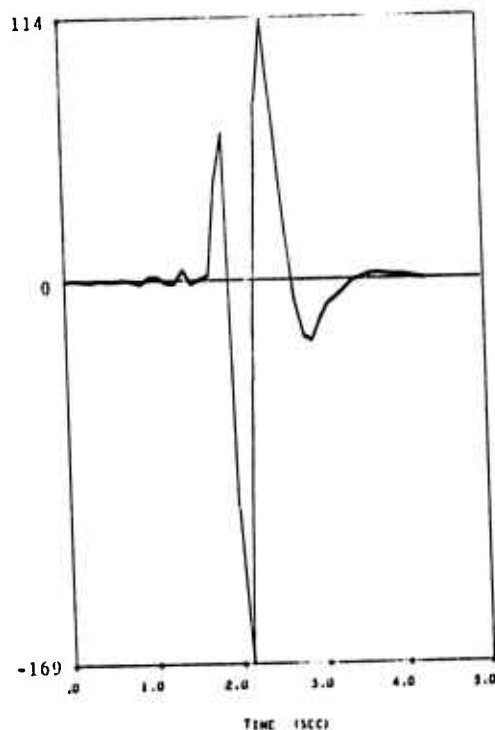
(b) Source G-2. $A_1 = 117$, $T_1 = 0.45$, $A_2 = 142$, $T_2 = 0.6$.

Fig. 4.45--First mantle arrival synthetic seismograms for the Piledriver event including tectonic release. Epicentral distance 3000 km, aximuth 300°, DOB = 463 meters, prestress σ_{12} = -536 bars, shatter zone radius R_0 = 400 meters, earth structure model CIT 109P 0.75 Q.

151

TABLE 4.9

BODY WAVE MAGNITUDES FOR PILEDRIVER RECORDS
OF FIGURE 4.45

Seismogram	m_b^*	$m_b^{(1)}$	$m_b^{(2)}$
4.45a (G-1)	5.65	5.91	5.87
4.45b (G-2)	5.26	5.55	5.42
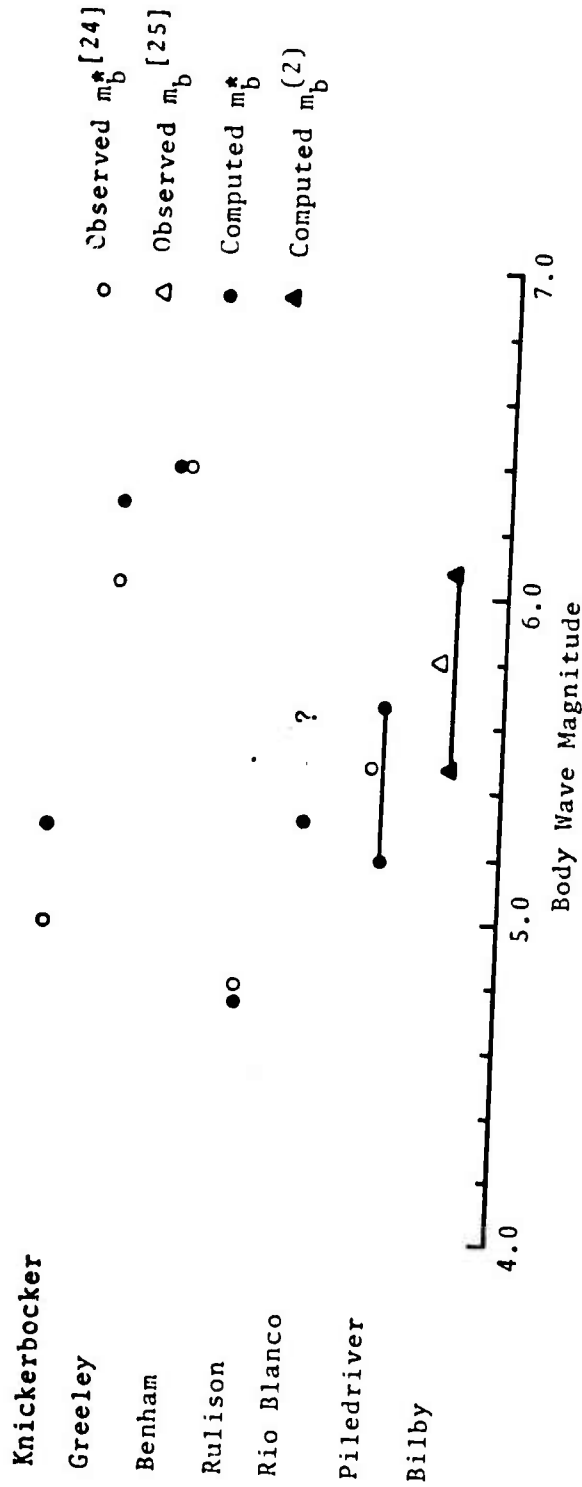
Fig. 4.46--Comparison of observed and computed body wave magnitudes. The earth structure model CIT 109P 0.75 Q was used for the computations shown.

V. SUMMARY AND CONCLUSIONS

Using a deterministic computer model, the dependence
of teleseismic ground motion on the near source material
properties, yield, tectonic stress release, depth of burial
and source-receiver earth structure has been investigated.
In Section II the application of a Lagrangian, finite
difference shock wave code (SKIPPER) to compute the equi-
valent elastic source representation of an underground ex-
plosion is described. Calculations in tuff, sandstone and
granite media are presented demonstrating the effect of
changing near-source material properties on the explosion
source spectrum.

In Section III the SKIPPER code output in the form of
the reduced displacement potential ($\psi(\tau)$) is used to drive
the teleseismic surface wave codes to compute synthetic
Rayleigh wave seismograms. Determining surface wave magni-
tude, M_s, directly from these seismograms, the dependence
of this important parameter on the source spectrum, depth of
burial and the earth structure model is studied.

Section IV is devoted to a study of the dependence of
teleseismic body waves on the important controlling para-
meters. The explosion source, which is primarily given by
the SKIPPER generated reduced displacement potential, may
also have a tectonic stress release component. Once again
synthetic seismograms are generating allowing a determina-
tion of body wave magnitude, m_b, in a standard manner. An
investigation of the dependence of m_b on the source spectrum
(including tectonic release), yield, depth of burial, near
source wave velocities and the earth structure model is
presented.

Among the important conclusions resulting from this
research are the following:

Preceding page blank

155

1. Given an invariant earth structure and fixing the
    depth of burial, Rayleigh wave amplitude is linearly
    related to the steady state value of the reduced
    displacement potential, $\psi(\infty)$.

2. Rayleigh wave amplitude is nearly insensitive to
    changes in depth of burial when $\psi(\infty)$ and the earth
    structure are invariant for DOB in the range of 0 to
    6400 ft.

3. The first two conclusions imply that Rayleigh wave
    amplitude scales as the yield, W, of the explosion
    and M_S scales as $\log_{10} W$ when both the near source
    material properties and earth structure are in-
    variant.

4. Rayleigh wave magnitude (M_S) is quite sensitive to the
    seismogram phase at which peak to peak amplitude is
    measured. This is especially true if the earth struc-
    ture gives a large Airy phase both within the band
    pass of the seismometer and near 20 seconds.

5. For the first arrival P wave train, the spectral
    shape and position of the spectral peak is controlled
    almost entirely by the depth of burial. The wave
    train is assumed to be composed of both direct and
    reflected phases and the shaping of the spectrum
    is caused by interference between the two.

6. Changing the explosion yield while keeping the depth
    of burial fixed does not appreciably alter the shape
    of the P wave train. In this situation P wave ampli-
    tudes, and hence m_b, scale as $\log_{10} W$.

7. Tectonic stress release at the source should have little
    effect on m_b. The major tectonic phase, the free sur-
    face converted sP_T phase, arrives too late to influence

156

magnitude measurements, while the earlier arriving P_T and pP_T phases are generally too small to significantly alter m_b. The effect of tectonic stress release on M_s remains an area for future study.

8.   One of the main advantages of the computational model described in this report may well be its ability to rapidly invert field observations to deduce the earth structure model appropriate for a specific source-receiver configuration. Having made the inversion to obtain reliable earth structure models, it should then be possible to derive the explosion yield from teleseismic data.

VI. REFERENCES

1. Cherry, J. T., C. B. Archambeau, G. A. Frazier, A. J. Good, K. G. Hamilton and D. G. Harkrider, "The Teleseismic Radiation Field From Explosions: Dependence of Seismic Amplitudes Upon Properties of Materials in the Source Region," Systems, Science and Software Report SSS-R-72-1193, Contract No. DASA 01-71-C-0156, July 1972.

2. Harkrider, D. G., "Surface Waves in Multilayered Media I. Rayleigh and Love Waves from Buried Sources in a Multilayered Elastic Half-Space," B.S.S.A., 54, pp. 627-679, 1964.

3. Bullen, K. E., An Introduction to the Theory of Seismology, Cambridge University Press, 3rd Edition, Chapters 6, 7, and 8, 1963.

4. Cherry, J. T., A. J. Good and K. G. Hamilton, "Near Field Calculations For Seismic Predictions," Systems, Science and Software Final Report SSS-R-73-1605, Submitted to U.S.A.E.C., Nevada Operations Office, Contract No. DNA 001-72-C-0153, April 5, 1973.

5. Stephens, D. R., H. C. Heard and R. N. Schock, "High Pressure Mechanical Properties of Tuff from the Diamond Dust Site," Lawrence Livermore Laboratory Report UCRL-50858, April 27, 1970.

6. Riney, T. D., G. A. Frazier, S. K. Garg, A. J. Good, R. G. Herrman, L. W. Morland, J. W. Pritchett, M. H. Rice and J. Sweet, "Constitutive Models and Computer Techniques for Ground Motion Predictions," Systems, Science and Software Final Report SSS-R-73-1490, March 1973.

7. Springer, D. L. and R. L. Kinnaman, "Seismic Source Summary for U. S. Underground Nuclear Explosions, 1969-1970," B.S.S.A., 61, pp. 1073-1098, 1971.

8. Springer, D. L. and W. J. Hannon, "Amplitude-Yield Scaling for Underground Nuclear Explosions," B.S.S.A., 63, pp. 477-500, 1973.

9. Schock, R. N., H. C. Heard and D. R. Stephens, "Mechanical Properties of Rocks from the Site of the Rio Blanco Gas Stimulation Experiment," Lawrence Livermore Laboratory Report UCRL-51260, 1972.

Preceding page blank

10.   Terhune, R. W., "Prediction of Underground Nuclear
        Explosion Effects in Wagon Wheel Sandstone," Lawrence
        Livermore Laboratory Report UCRL-50993-Rev. 1, 1971.

11.   Stephens, D. R., and E. M. Lilley, "Static P-V Curves
        of Cracked and Consolidated Earth Materials to 40 kb,
        UCRL-14711, Lawrence Livermore Laboratory, 1966.

12.   Heard, H. C., "The Influence of Environment on the In-
        elastic Behavior of Rocks, in Symposium on Engineering
        with Nuclear Explosives Conference, 700101, Vol. 1,
        1970.

13.   Toksöz, M. N., D. G. Harkrider, and A. Ben-Menahem,
        "Determination of Source Parameters by Amplitude
        Equalization of Seismic Surface Waves. 2.   Release
        of Tectonic Strain by Underground Explosions and
        Mechanisms of Earthquakes," J. Geophys. Res., 70,
        pp. 907-922, 1965.

14.   Lambert, D. G., E. A. Flinn, and C. B. Archambeau,
        "A Comparative Study of the Elastic Wave Radiation
        from Earthquakes and Underground Explosions," Geophys.
        J. Roy. Astr. Soc., 29, pp. 403-432, 1972.

15.   Archambeau, C. B., and C. Sammis, "Seismic Radiation
        from Explosions in Prestressed Media and Measurement
        of Tectonic Stress in the Earth," Rev. Geophys. and
        Space Phys., 8, pp. 473-499, 1970.

16.   Toksöz, M. N., and H. H. Kehrer, "Tectonic Strain-
        Release Characteristics of Cannikin," B.S.S.A, 62,
        pp. 1425-1438, 1972.

17.   Archambeau, C. B., "The Theory of Stress Wave Radia-
        tion from Explosions in Prestressed Media," Geophys.
        J. Roy. Astr. Soc., 29, p. 329, 1972.

18.   Gutenberg, B., and C. F. Richter, "On Seismic Waves,"
        Beitr. Geophysik, 47, pp. 73-131, 1936.

19.   "Long Range Seismic Measurements--Piledriver," Seismic
        Data Laboratory Report No. 165, Earth Sciences Division,
        Teledyne Industries, Inc., 1966.

20.   Bullen, K. E., An Introduction to the Theory of Seismo-
        logy, Cambridge University Press, 3rd Edition, 1963.

21.   Futterman, W. I., "Dispersive Body Waves," J. Geophys.
        Res., 67, pp. 5279-5291, 1962.

22. Strick, E., "A Predicted Pedestal Effect for Pulse Propagation in Constant-Q Solids," Geophysics, 35, pp. 387-403, 1970.

23. Archambeau, C. B., E. A. Flinn, and D. G. Lambert, "Fine Structure of the Upper Mantle," J. Geophys. Res., 74, #25, 1969.

24. Basham, P. W., and R. B. Horner, "Seismic Magnitudes of Underground Nuclear Explosions," B.S.S.A, 63, pp. 105-131, 1973.

25. "Long Range Seismic Measurements--Bilby," Data Analysis and Technique Development Center Report No. 87, United Earth Sciences Division, United Electrodynamics, Inc., 1963.

26. Lambert, D. G., and R. O. Ahner, "Seismic Analysis of the Rulison Explosion," ARPA Report prepared by Teledyne Geotech, ARPA Order No. 1714, 1972.